Plasmonics for surface-enhanced Raman scattering: from classical to quantum

Plasmonics for surface-enhanced Raman scattering: from classical to quantum

A thesis presented

by

Wenqi Zhu

to

The School of Engineering and Applied Sciences

in partial fulfillment of the requirements
for the degree of
Doctor of Philosophy
in the subject of

Engineering Sciences

Harvard University
Cambridge, Massachusetts

May 2014

Thesis advisor
Kenneth B. Crozier

Author
Wenqi Zhu

Plasmonics for surface-enhanced Raman scattering: from classical to quantum

Abstract

Metallic nanostructures that employ localized surface plasmon resonances to capture or radiate electromagnetic waves at optical frequencies are termed "plasmonic optical antennas". These structures enhance light-matter interactions in an efficient manner, enabling unique linear and nonlinear optical applications. One such application is surface-enhanced Raman scattering (SERS), which employs plasmonic antennas to enhance Raman cross-section of molecules by orders of magnitude. SERS has attracted a significant amount of research attention since it enables molecules to be identified through their characteristic vibrational spectra, even at the single molecule level.

In this thesis, we investigate the mechanisms underlying electromagnetic enhancement in SERS, and optimize plasmonic optical antenna designs to allow efficient SERS detection. We first demonstrate a top-down fabrication procedure to reproducibly fabricate plasmonic dimers with controllable gap widths that can be as small as 3 nm. We experimentally demonstrate that SERS enhancements increase as the gap size is reduced. The method we introduce is capable of routinely delivering reproducible SERS substrates with high enhancement factors. We then investigate a technique termed "energy-momentum spectroscopy" to measure Raman emission patterns, i.e. the angular distribution of Raman scattering. In particular, we demonstrate how they are modified by plasmonic optical antennas. It is found that the Raman scattering from molecules on

plasmonic dimers (pairs of gold rods) forms two beams into the substrate which supports the dimers. This would normally necessitate the use of an objective lens with a large numerical aperture for efficient collection. We investigate the abilities of two alternative optical antenna designs to modify the angular distribution of Raman scattering. We term this effect "beamed Raman scattering". The first antenna design is that of Yagi-Uda antennas. The second design consists of plasmonic dimers formed above a gold film integrated with a one-dimensional array of gold stripes. For both antenna types, beamed Raman scattering is observed.

In most cases, the electromagnetic enhancement mechanism of SERS can be understood by classical electromagnetic theory. Only recently has it become well-appreciated that quantum mechanical effects such as nonlocality and electron tunneling emerge as the feature sizes of metallic nanostructures approach atomic length-scales. We unambiguously demonstrate the emergence of electron tunneling at optical frequencies for metallic nanostructures with gap-widths in the single-digit angstrom range. Moreover we experimentally demonstrate, for the first time the best of our knowledge, that the emergence of electron tunneling limits the maximum achievable SERS enhancement.

Table of Contents

List of Publications

Journals:

W. Zhu and K. B. Crozier, "Quantum Mechanical Limit to Plasmonic Enhancement: Observation by Surface-Enhanced Raman Scattering," in preparation, 2014.

W. Zhu, D. Wang, and K. B. Crozier, "Direct observation of beamed Raman scattering," Nano Letters 12, 6235–6543 (2012).

W. Zhu, M. G. Banaee, D. Wang, Y. Chu, and K. B. Crozier, "Lithographically fabricated optical antennas with gaps well below 10 nm," Small 7, 1761–1766 (2011).

D. Wang, **W. Zhu**, M. D. Best, J. P. Camden, and K. B. Crozier, "Wafer-scale metasurface for total power absorption, local field enhancement and single molecule Raman spectroscopy," Scientific Reports 3, 2867 (2013).

D. Wang, **W. Zhu**, M. D. Best, J. P. Camden, and K. B. Crozier, "Directional Raman scattering from single molecules in the feed gaps of optical antennas," Nano Letters 13, 2194–2198 (2013).

S. Lin, **W. Zhu**, Y. Jin, and K. B. Crozier, "Surface-enhanced Raman scattering with Ag nanoparticles optically trapped by a photonic crystal cavity," Nano Letters 13, 559–563 (2013).

D. Wang, **W. Zhu**, Y. Chu, and K. B. Crozier, "High directivity optical antenna substrates for surface enhanced Raman scattering," Advanced Materials 24, 4376–4380 (2012).

Y. Chu, **W. Zhu**, D. Wang, and K. B. Crozier, "Beamed Raman: directional excitation and emission enhancement in a plasmonic crystal double resonance SERS substrate," Optics Express 19, 20054–20068 (2011).

Y. Chu, D. Wang, **W. Zhu**, and K. B. Crozier, "Double resonance surface enhanced Raman scattering substrates: an intuitive coupled oscillator model," Optics Express 19, 14919–14928 (2011).

Conference Presentations:

W. Zhu and K. B. Crozier, "Plasmonics: Quantum on the Angstrom Scale, as Observed by Surface-enhanced Raman Scattering," ***invited***, Conference on Lasers and Electro-Optics (2014).

W. Zhu, D. Wang, and K. B. Crozier, "Surface-enhanced Raman scattering from plasmonic dimers with gap widths in the quantum regime," The 6th International Conference on Surface Plasmon Photonics (2013).

W. Zhu, D. Wang, Y. Chu and K. B. Crozier, "Directing Raman scattering with nanoscale Yagi-Uda antenna," poster, Gordon Research Conference - Plasmonics (2012).

W. Zhu, D. Wang, Y. Chu, and K. B. Crozier, "Collimation of Raman scattering with plasmonic structures," Conference of Quantum Electronics and Laser Sciences (2012).

W. Zhu, M. G. Banaee, and K. B. Crozier, "Lithographically fabricated optical antennas with sub-10nm gaps formed by a sacrificial layer," ***invited***, Conference of Quantum Electronics and Laser Sciences (2010).

List of Contributions

1. We developed a fabrication procedure based on a sacrificial layer for the lithographic fabrication of optical antennas with gaps well below 10 nm. The gap size can be controlled by oxidizing the sacrificial layer using oxygen plasma. The electric fields in the antenna gaps can be significantly enhanced. This is confirmed by SERS measurements.

2. We directly observe the Raman emission patterns of molecules on dimer antennas on dielectric substrates. Our technique allows Raman scattering to be distinguished from the broad luminescent background continuum that typically occurs in SERS, thereby enabling the Raman emission patterns from different plasmonic structures to be unambiguously measured. It is found that plasmonic nanostructures modify Raman emission patterns. For dimer antennas, most of the Raman scattering occurs into the substrate, peaking around the critical angle.

3. We measure the Raman emission patterns from molecules on nanoscale Yagi-Uda antennas. By using a nanoparticle dimer, instead of a single nanoparticle, as the feed element, the overall SERS intensity is significantly enhanced. Using Raman emission pattern measurements, we show that the reflector and director antennas in our Yagi–Uda antenna direct Raman scattering into the forward direction. Raman emission patterns of different Raman lines indicate that the operating bandwidth of the Yagi–Uda antenna is around 85 nm.

4. We directly observe beamed Raman scattering, i.e. highly directional Raman emission patterns, from a structure consisting of dimer antennas formed above a gold film and integrated with a one-dimensional array of gold stripes. A large SERS enhancement factor (1.2×10^{10}) is achieved with this structure. The Raman scattering from the structure is collimated into a direction that is surface-normal to the substrate. We show that the observed Raman emission patterns can be understood by considering by the bandstructures of the surface plasmon polaritons supported by the substrate.

5. We developed a method to lithographically fabricate dimers with angstrom scale gap-width. Through dark-field scattering spectra and transmission electron microscope images, we demonstrate the emergence of electron tunneling at optical frequencies for metallic nanostructures with gap-widths in the single-digit angstrom range. Moreover, we experimentally demonstrate, for the first time to the best of our knowledge, that the emergence of electron tunneling limits the maximum achievable plasmonic enhancement. This conclusion is reached via SERS measurements.

Acknowledgement

First, I would like to thank my advisor Prof. Kenneth B. Crozier for his guidance and support throughout my Ph. D. study. He introduced me to the wonderful field of nano-optics, and granted me freedom in my investigations of interesting research topics. He has always been able to point out crucial questions that I had missed. The answers to these questions not only ensure the integrity of the research, but also many times lead to more discoveries and a deeper understanding of the physics. He also spent a significant amount of time in helping me improve my writing and presentation skills. This has not only helped my Ph. D. studies, but is also highly likely to be beneficial for my future professional career. He encouraged and supported me to attend many conferences which I found truly helpful to my research.

I would like to thank Prof. Federico Capasso and Prof. Jene A. Golovchenko for their time as members of my Ph.D. committee. They have provided insightful comments and advice on my research. I feel privileged to learn from them. I would also like to thank Prof. Eric Mazur for his time as a committee member in my Ph. D. qualification exam.

I would like to thank all former and present group members in the Crozier group. In particular, I am grateful to Dr. Shiyun Lin, Dr. Dongxing Wang and Dr. Anthony Orth. We came to Harvard in the same year. It has been a pleasure to work and study with them during my Ph. D. degree. I would also like to thank Dr. Mohammad Banaee and Dr. Yizhuo for their knowledge and generous help. I am also grateful to have worked with Dr. Tian Yang, Dr. Yaping Dan, Dr. Kai Wang, Dr. Tal Ellenbogen, Dr. Seo Kwanyong, and

Ph.D. candidate Hyunsung Park. Daily discussions with them were indeed helpful to my research.

I would like to thank all staff members in Harvard CNS. In particular, I want to thank Dr. Yuan Lu, Dr. Jiangdong Deng, Dr. Ling Xie and Dr. Ed Macomber for their professional training and performing maintenance of the nanofabrication tools that I have used. I also want to thank Dr. Adam Graham, Dr. Carolyn Marks and Dr. Dave Lange for their professional training and for performing maintenance of the electron microscopes that I have used.

I would like to thank all my friends at Harvard. It is my pleasure to have studied and worked with them. I would especially like to thank Dr. Xinwei Wang from the Gordon group in Department of Chemistry. He has provided crucial advice related to the preparation of my TEM samples.

Finally I would like to thank all my family members in China and my wife Shiyu Wang. All my family members, especially my parents and my grandparents, have been very supportive during my Ph. D. study. I would not have been able to accomplish this without their love. Meanwhile, I feel so fortunate to have met my wife Shiyu Wang in the third year of my Ph. D. study. Love from her and her parents have been essential in this journey.

Dedicated to

my parents

Zhilan Rao and Raorong Zhu

and my wife Shiyu Wang

Chapter 1 Introduction

1.1 Overview

The field of plasmonics has expanded dramatically over the past decade. This is a consequence of interest in the striking new physics that is being explored as well as the potential for new applications associated with many of the discovered phenomena [1]. One of the main topics of study in the field of plasmonics is that of "surface plasmon polaritons" or SPPs. The term "plasmon" refers to the quantum particle representation of plasma oscillations, which are collective oscillations of the electron density in conducting media such as plasmas or metals [2]. Among them, "surface plasmons" refer to those plasmons which are confined to metallic surfaces; they usually interact strongly with light, resulting in their designation as "polaritons". SPPs can be categorized into propagating SPPs and localized surface plasmon resonances (LSPRs). The former usually represent surface waves bound to one-dimensional (1D) metal/dielectric interfaces. They can be excited by prism coupling [3], or by small perturbation to the surface, such as protrusions [4] or slits [5]. Engineering the surface structures of metals and the dispersions of propagating SPPs have lead to interesting optical phenomena such as extraordinary transmission [6], negative refraction [7], and "spoof" surface plasmons [8].

The optical properties of propagating SPPs can also be exploited in nano lasing [9], optical trapping [10], and laser collimation [11] applications.

In LSPRs, surfaces plasmons are confined in two (2D) or three dimensions (3D). Metallic nanoparticles interact resonantly with visible light via LSPRs, resulting in distinct absorption and scattering phenomena. Applications of such LSPRs have a much longer history than the field of plasmonics: gold/silver nanoparticles dispersed in glass have been used since ancient times to represent colors. Recent developments in nanofabrication have permitted much more flexibility in the design of complex metallic nanostructures for various applications. For example, the strong absorption and scattering of metallic nanoparticles have been exploited in light harvesting in solar cells [12], optical filtering in thin-films [13], and designing metamaterials [14]/meta-surfaces [15,16]. The strong field enhancements in the vicinity of the nanoparticles have enabled single-molecule detection [17,18], the optical trapping of bacteria and other biological materials [19] and nanoscale nonlinear optical conversion [20,21].

My research focuses on the application of plasmonics in surface-enhanced Raman scattering (SERS). Raman spectroscopy is a powerful analytical method, enabling molecules to be identified through their characteristic vibrational spectra. In SERS, metallic nanoparticles function as “optical antennas” to enhance the Raman cross-section of molecules by orders of magnitude [22]. Engineered optical antennas boost the efficiency by which light can be focused into subwavelength regions. Similarly, in the reciprocal process, optical antennas boost the transmission of energy to the far-field. In this dissertation, we investigate the performance of optical dimer antennas for both of these processes. We first demonstrate that the higher SERS enhancement can be achieved

from dimer antennas with gaps well below 10 nm. We then show that dimer antennas do not transmit Raman scattering into the far-field in a manner that is effective as it could be, and that this situation can be improved by adding collimation structures. We also investigate the impact of quantum mechanical effects on both the far-field and near-field optical properties of dimer antennas with angstrom-scale gaps, and demonstrate that the ultimately achievable SERS enhancement is limited by electron tunneling.

The remainder of this chapter introduces physical descriptions of surface plasmons, including discussions of the optical properties of metals, of propagating SPPs at 2D dielectric/metal interfaces, of LSPRs supported by nanoparticles, and of quantum mechanical effects associated with surface plasmons. We also provide an introduction to Raman scattering and examine the mechanisms underlying SERS. Methods used to evaluate the SERS enhancement factor are furthermore discussed.

Chapter 2 introduces a lithographical nanofabrication method to achieve optical dimer antennas with gaps well below 10 nm. This is based on an electron-beam lithography process that has two steps and uses a sacrificial layer. Dimer antenna arrays with minimum gap size as small as 3 nm are achieved with this method, well below the resolution limit of conventional electron-beam lithography. The method we introduce is capable of routinely delivering reproducible SERS substrates with high enhancement factors.

Chapter 3 investigates the emission patterns of the Raman scattering from molecules on dimer antennas. We use a technique termed energy momentum spectroscopy to unambiguously observe Raman emission patterns. Our observations show that the majority of Raman scattering occurs into the substrate at angles larger than

the critical angle at the air/substrate interface. Efficient collection of the Raman signal is therefore only possible by use of an objective lens with a sufficiently large numerical aperture. This motivates the use of directional optical antenna structures for SERS substrates.

Chapter 4 discusses a directional optical antenna design for SERS, namely the nanoscale Yagi–Uda antenna. Directional emission is achieved in this structure by placing additional metallic nanoparticles, which work as a reflector and directors, around the dimer antenna. The functions of these additional nanoparticles, as well as the bandwidth of the Yagi–Uda antenna, are studied in this chapter.

Chapter 5 investigates another antenna design for directional Raman emission in which LSPRs on dimer antennas are coupled with SPPs on plasmonic substrates. This design not only boosts the SERS enhancement factor by ~77 times, but also collimates the Raman scattering to be within an angular spread of $\pm 5^\circ$ from the surface normal.

Chapter 6 examines the impact of quantum mechanical effects on the field enhancements achieved by plasmonic structures. We develop a lithographic method to achieve dimer structures with angstrom-scale gaps, and study their far-field and near-field optical properties. Achieving small gaps has been a long-pursued goal for high performance SERS substrates. Our results, however, suggests that smaller gaps are not always beneficial due to the emergence of electron tunneling when the gap-width approaches the atomic scale.

1.2 Surface plasmon polaritons – classical view

Despite being named in a manner that emphasizes quantum mechanical aspects, SPPs can be usually understood from purely classical electromagnetics. In this approach, the response of the electrons is described by the permittivity of the material. The interaction between the electrons and the electromagnetic waves is thus included in the constitutive relations of the macroscopic Maxwell equations. Therefore, the optical properties of SPPs are obtained by solving the Maxwell equations for the "propagating" or "localized" electromagnetic waves.

1.2.1 Optical properties of metals

The field of plasmonics is mainly concerned with the interaction between visible light and nanoparticles made of noble metals such as gold and silver. Understanding the dielectric functions of these metals at optical frequencies is therefore of great importance to the study of SPPs. Here, we derive the Drude-Sommerfeld model, which describes the contributions of bound and free electrons to the dielectric function of a metal. We also note that surface plasmons have been also observed in other materials such as graphene, transition metal oxides and transition metal nitrides. These interact primarily with light at near- and mid-infrared wavelengths. The dielectric functions of these materials can be modeled by approaches similar to those employed here.

We use a simple harmonic oscillator model to describe the motion of electrons in the presence of an applied electromagnetic field. For simplicity, we only consider the motion in one dimension. Assuming plane wave excitation, the motion of an electron is given by:

$$m_e^* \ddot{x} + m_e^* \gamma \dot{x} + \mathrm{K}x = -eEe^{-i\omega t} \tag{1.1}$$

where m_e^* is the effective mass of electrons, γ is the damping coefficient associated with electron scattering, Kx is a restoring force, $-e$ is the charge of the electron, $Ee^{-i\omega t}$ is time-varying local field applied to the electron. A solution to Equation (1.1) is $x(t) = x_0 e^{-i\omega t}$, describing the oscillation of the electron at the same frequency as the driving field. Here, we consider the response of the free electrons. The spring coefficient K is therefore taken to be zero. If we were to instead to consider the response of the bound electrons, this term would be non-zero. The instantaneous displacement of the electron is thus given by:

$$x(t) = \frac{e/m_e^*}{\omega(\omega + i\gamma)} Ee^{-i\omega t} \tag{1.2}$$

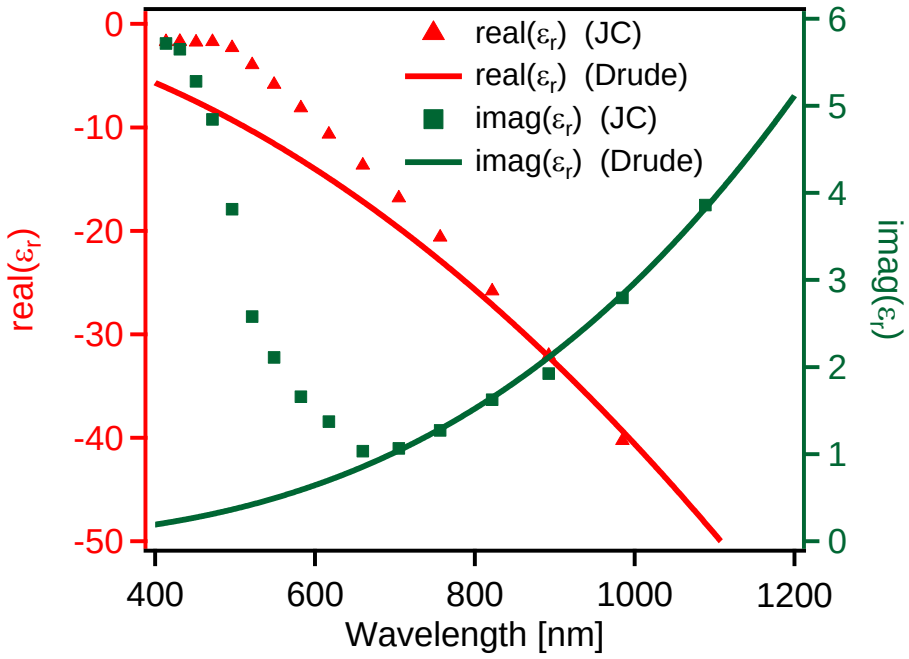

Figure 1.1. Drude model of gold with ω_p = 1.94×10^{15} Hz, and γ = 2.14×10^{13} Hz, compared with the experimentally measured dielectric functions from Ref. [23].

Now consider the collective oscillation of all the electrons in the unit volume, the macroscopic polarization is then given by:

$$P(t) = -Nex(t) = -\frac{N e^2 / m_e^*}{\omega(\omega + i\gamma)} E e^{-i\omega t} \tag{1.3}$$

where N is the number of electrons per unit volume. With the constitutive relations $D(t) = \varepsilon_0 \varepsilon_r E(t) = \varepsilon_0 E(t) + P(t)$, we obtain the dielectric function of the metal to be:

$$\varepsilon_r = 1 - \frac{\omega_p^2}{\omega(\omega + i\gamma)} \tag{1.4}$$

where $\omega_p = \sqrt{\frac{Ne^2}{\varepsilon_0 m_e^*}}$ is the plasma frequency of the metal. This equation is known as the Drude model of a metal. In Figure 1.1, we fit the experimentally measured dielectric function of gold [23] with the Drude model. A good fit is achieved for near-infrared wavelengths, while the deviation around 550 nm is due to the interband transitions of electrons that can be described by additional Lorentz model correction terms. These terms are modeled in the same way as that used for the free electrons, but with a non-zero value for the spring constant K. The result is termed the Drude-Sommerfeld model.

1.2.2 Propagating surface plasmon polaritons

With the dielectric functions of metals now understood, we now investigate why propagating SPPs can exist at dielectric/metal interfaces. In addition, we derive the dispersion relation of this surface wave and discuss its unique properties.

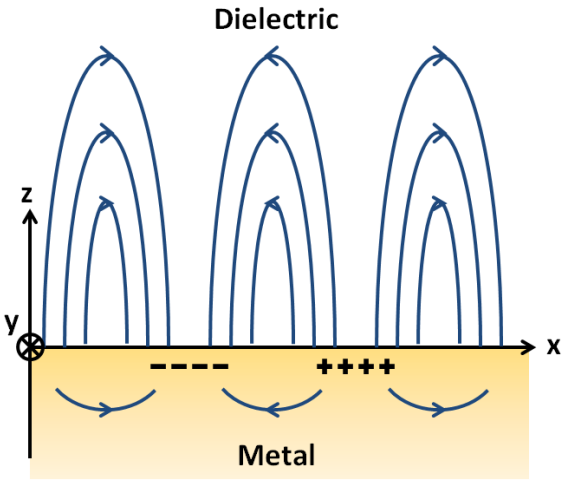

Figure 1.2. Schematic depiction of SPPs propagating along the interface between a metal and a dielectric material, showing instantaneous polarization charges and electric field lines.

As shown in Figure 1.2, propagating SPPs represent longitudinal oscillations of the surface charges. Hence, we assume a transverse-magnetic (TM) surface wave propagating along the x-axis. The field above the interface (i.e. in the dielectric) can be described by:

$$\vec{E}_1 = (\hat{x}E_{x1} + \hat{z}E_{z1})\exp[i(k_x x - \omega t)]\exp(-\gamma_{z1} z) \tag{1.5}$$

$$\vec{H}_1 = \hat{y}H_{y1}\exp[i(k_x x - \omega t)]\exp(-\gamma_{z1} z) \tag{1.6}$$

where $\gamma_{z1} > 0$ ensures that the TM mode is evanescent in the +z-direction. The dispersion relation in an isotropic medium requires:

$$\gamma_{z1} = \sqrt{k_x^2 - \omega^2 \mu_0 \varepsilon_0 \varepsilon_1} \tag{1.7}$$

By inserting Equation (1.5) and (1.6) into Ampere's law, we obtain

$$E_{x1} = \frac{-i\gamma_{z1}}{\omega\varepsilon_1} H_{y1} \tag{1.8}$$

Similarly, the field below the interface (i.e. in the metal) can be described by:

$$\vec{E}_2 = (\hat{x}E_{x2} + \hat{z}E_{z2})\exp[i(k_x x - \omega t)]\exp(\gamma_{z2} z) \tag{1.9}$$

$$\vec{H}_2 = \hat{y}H_{y2}\exp[i(k_x x - \omega t)]\exp(\gamma_{z2} z) \tag{1.10}$$

where $\gamma_{z2} > 0$ ensures that the TM mode is evanescent in the –z-direction. From the dispersion relation and Ampere's law, we have:

$$\gamma_{z2} = \sqrt{k_x^2 - \omega^2 \mu_0 \varepsilon_0 \varepsilon_2} \tag{1.11}$$

$$E_{x2} = \frac{i\gamma_{z2}}{\omega\varepsilon_2} H_{y2} \tag{1.12}$$

The boundary conditions require the continuity of the tangential component of the electric and magnetic fields, i.e. $E_{x1} = E_{x2}$ and $H_{y1} = H_{y2}$. From Equations (1.8) and (1.12) we have:

$$\frac{-\gamma_{z1}}{\omega\varepsilon_1} = \frac{\gamma_{z2}}{\omega\varepsilon_2} \tag{1.13}$$

Combining this equation with Equation (1.7) and (1.8), we obtain the dispersion relation of the propagating SPPs to be:

$$k_x = \frac{\omega}{c}\sqrt{\frac{\varepsilon_1\varepsilon_2}{\varepsilon_1 + \varepsilon_2}} \tag{1.14}$$

The real and imaginary parts of k_x for the propagating SPPs at air/gold interface are plotted in Figure 1.3. The real part of the dispersion curve is below the light line $k_x=\omega/c$, confirming that this wave is bound to the surface: the field amplitude maximum is achieved at the surface, with exponential decay into both the dielectric and metal media. This can be used for refractive index sensing [24] and optical trapping [25] where an evanescent field is desired. For the same reason, propagating SPPs cannot be directly excited in this configuration by free space illumination due to the mismatch in

momentum. In Chapter 5, it is shown that propagating SPPs can be efficiently excited with a 1D gold grating.

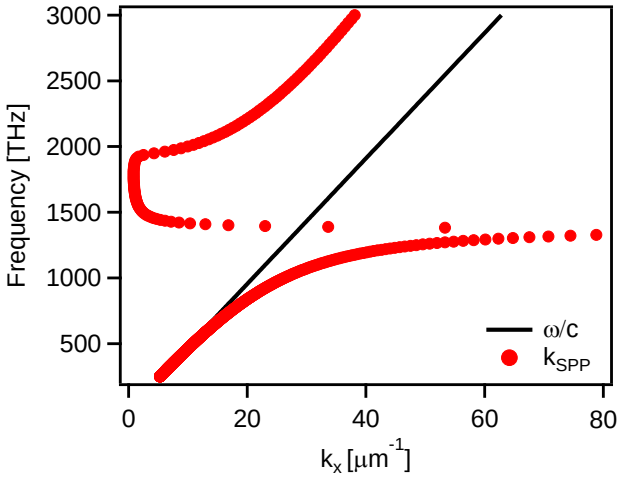

Figure 1.3. Dispersion of propagating SPPs at air/gold interface. The dielectric function of gold is given by the Drude model in Figure 1.2. Black line shows the light line $k_x=\omega/c$.

1.2.3 Localized surface plasmon resonances

Here, we describe the far-field and near-field optical properties of LSPRs on a metal nanosphere. Unlike the propagating SPPs, LSPRs can be directly excited by free space illumination. Figure 1.4(a) depicts the illumination of a nanosphere of radius *a* by a plane wave. For simplicity, we assume *a* is much smaller than the optical wavelength λ. This means that the phase retardation across the nanostructure is neglected and that the instantaneous field distribution can be found by the electrostatic approximation.

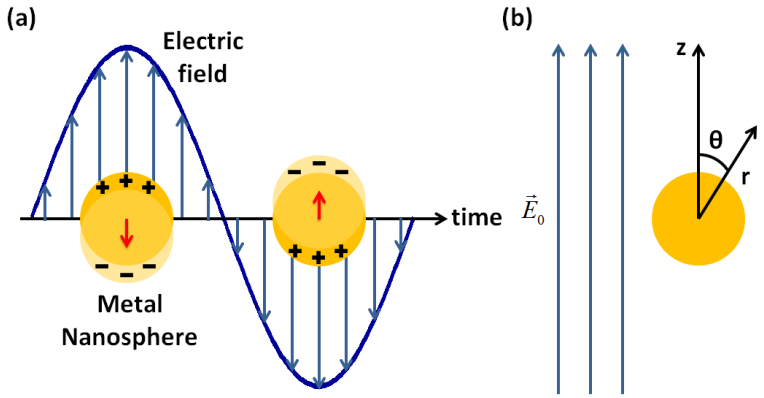

Figure 1.4. Localized surface plasmon resonance (LSPR). (a) Schematic illustration of localized collective electron oscillation. (2) Electrostatic approximation: definition of coordinates.

In the electrostatic approximation, the electric fields inside and outside the nanosphere, $\vec{E}_1$ and $\vec{E}_2$, respectively, can be expressed as the gradients of scalar potentials $\Phi_1(r,\theta)$ and $\Phi_2(r,\theta)$:

$$\vec{E}_1 = -\nabla\Phi_1, \qquad \vec{E}_2 = -\nabla\Phi_2 \tag{1.15}$$

The definition of the coordinates is shown in Figure 1.4(b). Due to the symmetry of the problem, the azimuthal angle φ is not included in the expressions. Due to charge neutrality, the electric potentials inside and outside of the nanosphere satisfy the Laplace equation:

$$\nabla^2\Phi_1 = 0 \quad (r < a), \qquad \nabla^2\Phi_2 = 0 \quad (r > a) \tag{1.16}$$

The solution for the Laplace equation in spherical coordinates is given by:

$$\Phi_1 = \sum_{m=0}^{\infty}(\alpha_m r^m + \beta_m r^{-(m+1)})P_m(\cos\theta) \tag{1.17}$$

where $P_m(\cos\theta)$ is the mth order Legendre polynomial. We now apply boundary conditions. We first consider that the electric potential $\Phi_1(r,\theta)$ inside the nanosphere

should be bounded for $r \to 0$. Also, the electric potential $\Phi_2(r,\theta)$ outside the nanosphere should be resemble that of the unperturbed field for $r \to \infty$. These two conditions are given by:

$$\lim_{r\to 0} \Phi_1 \; exists, \qquad \lim_{r\to 0} \Phi_2 = -E_0 z = -E_0 r\cos\theta \tag{1.18}$$

Boundary conditions also require the continuity of the electric potentials and the surface normal components of the displacement field:

$$\Phi_1(r=a) = \Phi_2(r=a), \quad \varepsilon_1 \left.\frac{\partial \Phi_1}{\partial r}\right|_{r=a} = \varepsilon_2 \left.\frac{\partial \Phi_2}{\partial r}\right|_{r=a} \tag{1.19}$$

It can be shown that the functions

$$\Phi_1(r,\theta) = -\frac{3\varepsilon_2}{\varepsilon_1 + 2\varepsilon_2} E_0 r\cos\theta \tag{1.20}$$

$$\Phi_2(r,\theta) = -E_0 r\cos\theta + a^3 E_0 \frac{\varepsilon_1 - \varepsilon_2}{\varepsilon_1 + 2\varepsilon_2} \frac{\cos\theta}{r^2} \tag{1.21}$$

satisfy the Equations (1.16), (1.18) and (1.19). The surface-normal electric field at the dielectric side of the interface is thus given by:

$$E_2(r=a,\theta) = -\frac{2\varepsilon_1 + \varepsilon_2}{\varepsilon_1 + 2\varepsilon_2} E_0 \cos\theta \tag{1.22}$$

We now obtain the expression for the largest field enhancement *FE* that occurs at the surface nanosphere to be:

$$FE = \left|\frac{2\varepsilon_1 + \varepsilon_2}{\varepsilon_1 + 2\varepsilon_2}\right| \tag{1.23}$$

Since the permittivity of metal can be negative, $real(\varepsilon_1) = -2\varepsilon_2$ represents a resonance condition where the denominator of Equation (1.23) approaches zero and field enhancement is only limited by the imaginary part of ε_1. For example, this can be

achieved with gold surrounded by air at a wavelength of 522 nm. Figure 1.5(a) shows a finite-difference time-domain (FDTD) simulation of the LSPR of a gold nanosphere with diameter of 60 nm at a wavelength of 522 nm. Strong near-fields can be observed at the two ends of the nanosphere, with the largest field intensity enhancement being ~25.

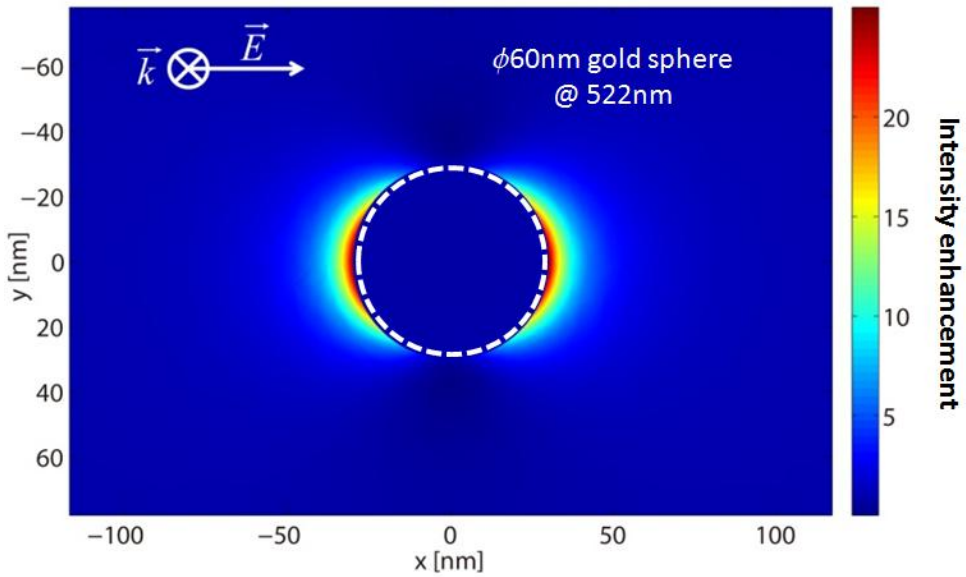

Figure 1.5 Intensity enhancement of the LSPR of a gold nanosphere with diameter of 60 nm. The nanosphere is illuminated with a plane wave at wavelength of 522 nm.

One means for achieving a field enhancement that is even higher is to employ two plasmonic structures, e.g. nanospheres, separated by a narrow gap (Figure 1.6). For gaps that are large, the field enhancement in the gap can be thought of as arising from the sum of the field enhancements provided by two isolated nanospheres. As the gap width reduces, coupling between the nanospheres increases. The plasmons on each nanosphere are not only excited by the incident plane wave, but also by the enhanced near field of the other nanosphere. This can lead to higher field enhancement. Through the mutual excitation or "coupling" of plasmons, a resonant "bonding dipole mode (BDP)" can be excited, and a much larger field enhancement within the nanoscale gap can thus be

expected. Figure 1.6 shows the FDTD simulation of a gold dimer consisting of two nanospheres with radii of 30 nm and a gap width of 5 nm. Upon illumination by a plane wave at a wavelength of 550 nm, the field intensity enhancement within the gap is ~1600 times larger than the incident field, and ~60 times higher than that of an isolated nanosphere.

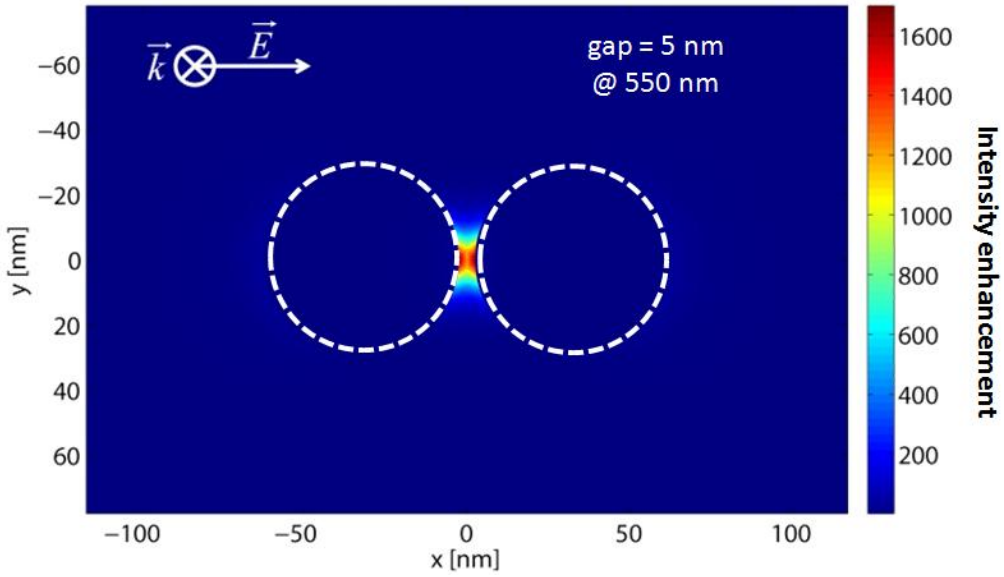

Figure 1.6 Intensity enhancement of the LSPR of a gold dimer consisting of two nanospheres with diameters of 60 nm. Maximum field enhancement is achieved with plane wave illumination when the wavelength is 550 nm.

1.3 Quantum plasmonics

As we have shown, SPPs can be generally well described by classical electromagnetics. Only recently has it become widely appreciated that the quantum mechanical "wave" nature of electrons needs to be considered as the feature size of the plasmonic nanostructure approaches the angstrom scale [26–29]. In this section, we consider two quantum mechanical effects that have significant impact on both near-field and far-field optical properties of plasmonic nanostructures.

1.3.1 Nonlocal effect

In the classical treatment of SPPs, the optical properties of metals are described by dielectric permittivity tensors that are functions of frequency only. This classical model is also referred as being a "local" model. By contrast, non-local models take the dielectric permittivity as being not only a function of frequency, but also of electron wavenumber k [26]. This correction is important for very small features such as sharp tips or small gaps. This is because it accounts for quantum mechanical effects that occur in such situations, such as the Pauli Exclusion Principle between electrons in narrow regions [27]. For example, consider the dimer with a nanoscale gap that is analyzed using classical electromagnetics in the previous section. In addition to the classical Coulomb repulsion that is accounted for in Maxwell equations, the electron density around the gap region is now further limited by Pauli repulsion. This leads to the field enhancement within the gap region being reduced in comparison to the predictions of classical electromagnetics.

In the non-local model, the charge continuity equation of classical electromagnetics is replaced by a hydrodynamic equation:

$$\beta^2 \nabla(\nabla \cdot \vec{J}) + (\omega^2 + i\gamma\omega)\vec{J} = i\omega\omega_p^2 \varepsilon_0 E \tag{1.24}$$

where $\vec{J}$ is the current inside the metal induced by an electric field $\vec{E}$ oscillating at frequency ω. The non-local coefficient β is proportional to the Fermi velocity v_F of the electrons within the metal through $\beta = \sqrt{3/(D+2)}v_F$, where D is the number of dimensions that are not quantum confined [30]. In some investigations, β has been taken as a fitting parameter in the hydrodynamic model in order to match the experimentally measured optical properties [27].

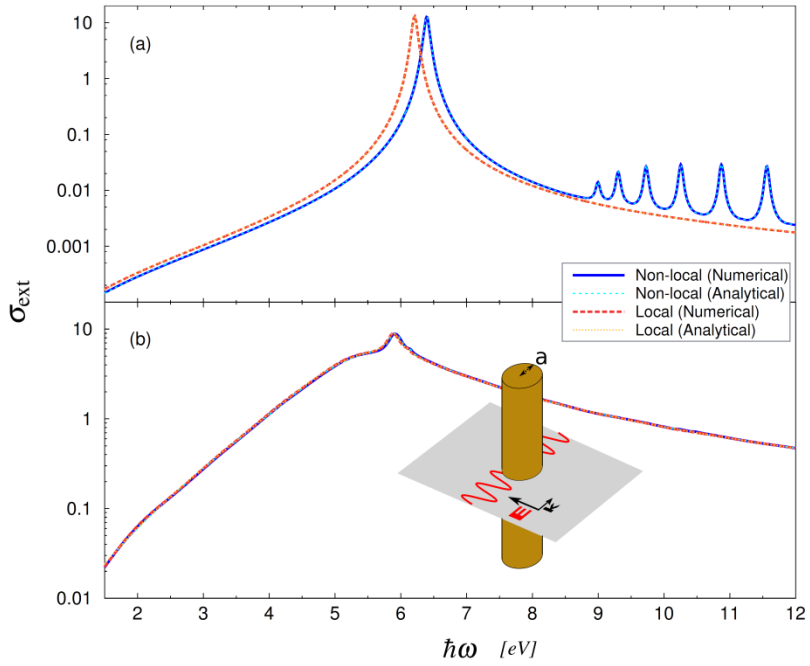

Figure 1.7 Nonlocal effects for nanowires. 2D calculations/simulations of extinction cross sections of nanowires with two radii: (a) radius a = 2 nm; (b) radius a = 25 nm. (Adapted from Ref. [30])

Toscano et al. solved this equation for 2D gold nanostructures using the finite element method (FEM) [30]. The authors first studied the far-field extinction cross-sections of infinitely long nanowires with radii of 2 nm and 25 nm, as shown in Figure 1.7. For the nanowire of radius 2 nm, the simulation results of Figure 1.7(a) show considerable differences between the local model and non-local model, namely the blueshift of the surface plasmon resonance, and the confined bulk plasmon resonances above the plasma frequency. In comparison, simulation results for the nanowire with radius of 25 nm in Figure 1.7(b) show no visible difference between local and non-local models. These two examples indicate that for an isolated nanostructure, non-local effects are only significant if the nanostructure is very small.

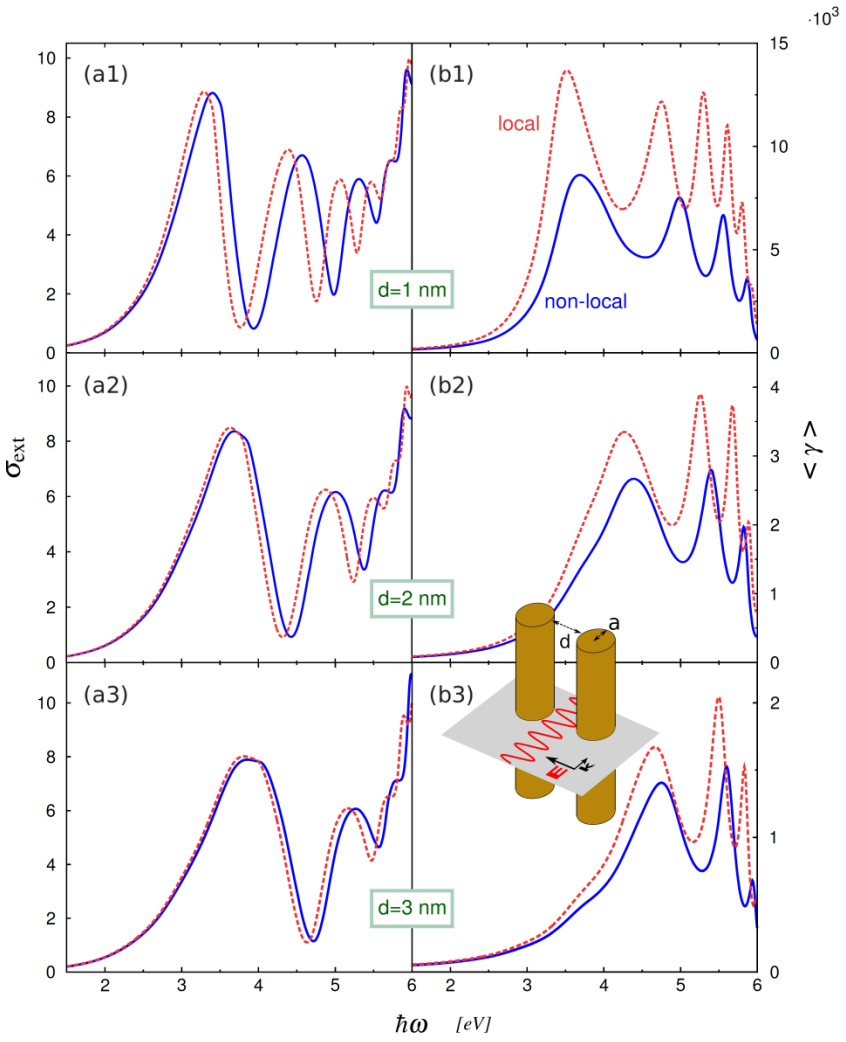

Figure 1.8 Nonlocal effects for nanowire dimers with various gap-width. The radius of each nanowire is 25 nm. 2D simulations of extinction cross sections and field enhancement at gap center of nanowire dimers with three gap-widths are shown: (a1-b1) d = 1 nm; (a2-b2) d = 2 nm; (a3-b3) d = 3 nm. (Adapted from Ref. [30])

As shown in Figure 1.8, the authors further studied the impact of nonlocal effects on both the far-field extinction and near-field enhancement of dimers of cylindrical nanowires. In all three cases, constituent nanowires have radii of 25 nm. As shown in Figure 1.7, for isolated nanowires with this radius, non-local effects are insignificant. Figure 1.8 indicates however that for nanowire dimers separated by small gaps, non-local

effects can be important. For all gap widths considered in Figure 1.8, the non-local model predicts extinction resonances and field enhancements that are blue-shifted and reduced, respectively, in comparison with the predictions of the local model. The differences are more significant for smaller gap-widths, confirming that it is for very small features sizes that non-local effects become important.

We have thus far considered non-local effects for the case of 2D plasmonic nanostructures. One would expect non-local effects to have similar impacts on the far-field and near-field optical properties of 3D plasmonic nanostructures. However, solving the hydrodynamic equation in 3D is computationally difficult. Typically, one exploits symmetry to reduce the 3D problem to 2D. Recently, Yu et al. developed a method termed a "local analogue model (LAM)" to simulate nonlocal effects for 3D nanostructures [31] using classical electromagnetic theory. The approach is also schematically illustrated in the inset of Figure 1.9. In this example, the authors simulate both the far-field and near-field optical properties of a dimer of two cylindrical wires with radii of 10 nm and a gap width of 0.2 nm. Since the gap-width is small, the local and non-local (solution to hydrodynamic equation) models give significantly different results. The idea behind LAM is to use an effective medium to take non-local effects into account. This means that the simulations only comprise classical electromagnetics, rather than solutions to the hydrodynamic equation. The parameters of the effective medium are chosen in a way that ensures that the far-field and near-field optical properties outside the metal region match those of the non-local model. The authors found this effective medium can be implemented by replacing gold near the surface by a modeling layer whose dielectric function ε_t and thickness Δd are related by:

$$\frac{\varepsilon_t}{\Delta d} = \frac{\varepsilon_b \varepsilon_m q_L}{\varepsilon_m - \varepsilon_b} \tag{1.25}$$

where ε_b is the dielectric constant of the background, ε_m is the dielectric function of the metal (typically given by the Drude model with plasma frequency ω_p and damping frequency γ), and $q_L = \sqrt{\omega_p^2 / \varepsilon_\infty - \omega(\omega + i\gamma)} / \beta$ is the longitudinal plasmon normal wave vector, which is inversely proportional to the decaying length of the surface charges. β is again the non-local coefficient which showed up in the hydrodynamic model. It should be noted that the modeling layer is inside the metal, meaning that the gap width is not affected. Figure 1.9 shows that the absorption cross sections and near-field enhancements of 2D metal nanowires predicted by the LAM method (with Δd = 0.1 nm) are in good agreement with the predictions of the non-local hydrodynamic model.

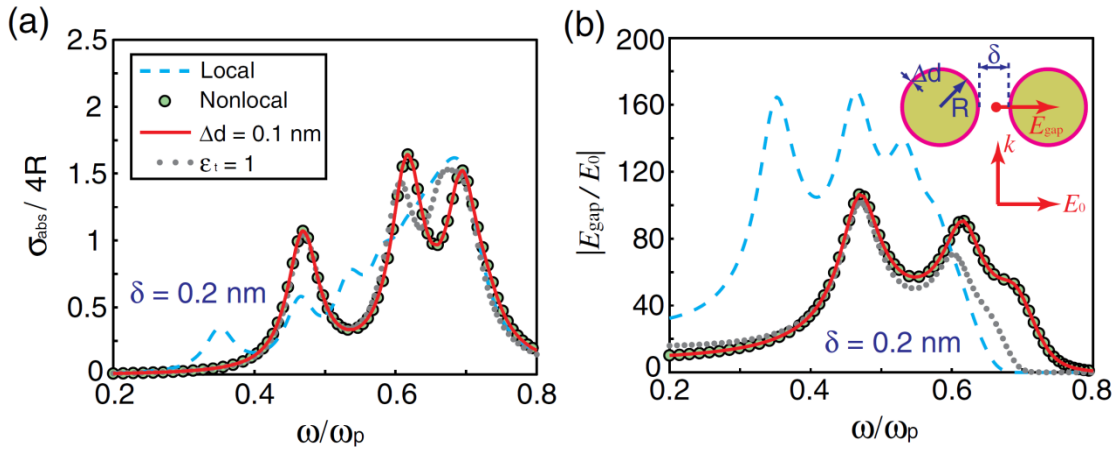

Figure 1.9 LAM model tested for 2D nanowire dimer. The radius of each nanowire is 10 nm, and the gap-width is 0.2 nm. (a) Absorption cross section simulated using different methods. (b) Field enhancement at gap center simulated using different methods. The inset shows the configuration of LAM method. (Adapted from Ref. [31])

The authors also test the effectiveness of this LAM method for 3D plasmonic nanostructures. In Figure 1.10, a dimer consisting of two conical gold nanoparticles with

a gap width of 0.5 nm is considered. Again, the non-local modeling predicts absorption cross section resonances that are blue-shifted and field enhancements that are reduced, in comparison to the local model. It can be seen that the predictions of the LAM method are in good agreement to those of the non-local model. The insets of Figure 1.10 compare the near-field distributions within the gap region, as calculated using the LAM method and by the non-local model (hydrodynamic equation). Although the field distributions are different within the gold, especially near the boundaries, the fields outside the gold are very similar. Thus we conclude that the LAM method captures non-local effects in 3D plasmonic structures well. We use this method to simulate nonlocal effects in Chapter 6.

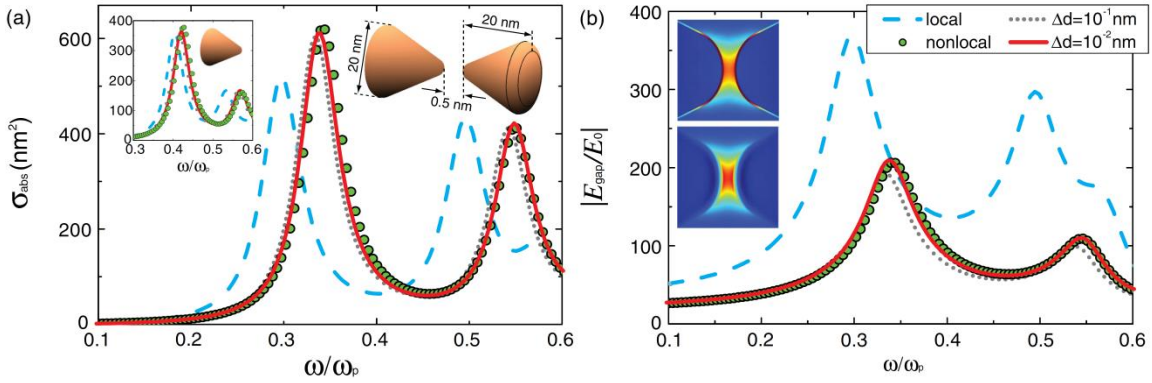

Figure 1.10 LAM model tested for 3D conical dimer. The gap-width is 0.2 nm. (a) Absorption cross section simulated using different fitting parameter Δd. (b) Field enhancement at gap center simulated using different fitting parameter Δd. The inset of (b) shows field distributions predicted by LAM method (top) and non-local model (bottom). (Adapted from Ref. [31])

1.3.2 Electron tunneling

Another quantum mechanical effect that is predicted to occur in plasmonic dimers as gap widths approach the angstrom scale is that of electron tunneling. This is depicted in

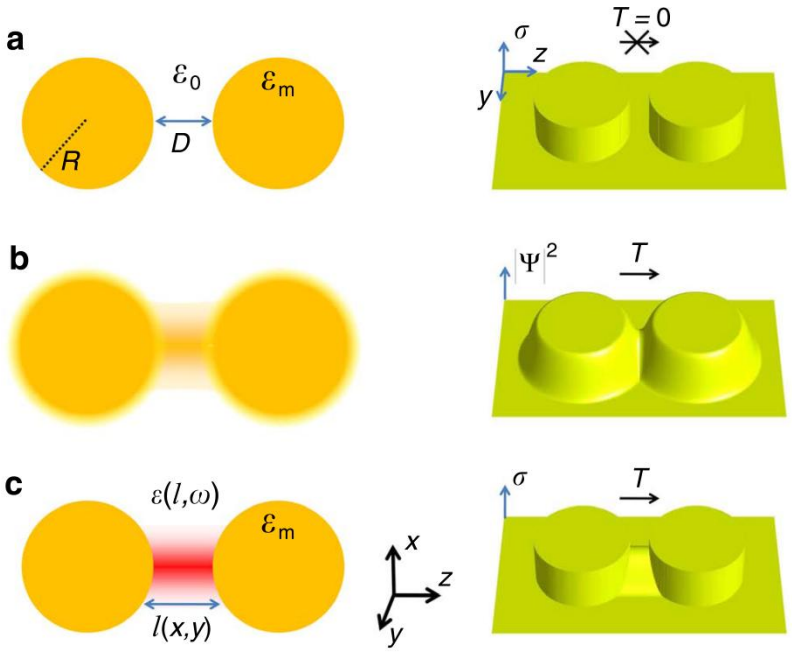

Figure 1.11 Schematic description of plasmonic dimer within classical and quantum mechanical treatments. (a) Classical model. (b) Full quantum mechanical model showing the wave nature of electrons at the boundaries. (c) Quantum corrected model (QCM) that uses effective medium to describe electron tunneling. (Adapted from Ref. [32])

Figure 1.11. We again consider the "wave" nature of the electrons. The electron densities do not completely fall to zero at the boundaries of the metal as shown in Figure 1.11(a); rather decay evanescently as a function of distance from the metal (Figure 1.11(b)). Therefore, for very small gap widths, the wavefunctions on the two sides of the gap region can overlap. The electrons from one side of the dimer can tunnel through the gap to reach the other side of the dimer. We also note that the transmission of electrons across the gap is expected to occur on a timescale far shorter than an optical cycle. Thus, the tunneling current adiabatically follows the field in the junction. Under this assumption, electrostatic approximation is still valid. Electron tunneling can thus be interpreted as introducing a "charge transfer" channel across the gap. As shown in Figure 1.6, large

field enhancement can be achieved with the BDP mode of the dimer, as charges of opposite sign accumulate on the two sides of the gap. One would therefore expect that the presence of tunneling would neutralize these charges, leading to the field enhancement being much smaller than predicted by classical electromagnetic theory.

As before, full quantum mechanical simulations that take into account electron tunneling effects are only numerically practical for nanoparticles whose diameters are smaller than 5 nm. To incorporate electron tunneling for "large" plasmonic structures, Esteban et al. developed a "quantum-corrected model (QCM)" that enables the effect of electron tunneling to be included in classical electromagnetic calculations. This is achieved by replacing the vacuum permittivity of the gap region by a Drude model that captures the tunneling process (Figure 1.11(c)). As indicated in Figure 1.11(c), different parts of the gap have different gap distance l, i.e. l is a function of (x,y). For a given gap distance l, the dielectric function of the gap region is given by:

$$\varepsilon(l,\omega) = 1 - \frac{\omega_g^2}{\omega(\omega + i\gamma_g(l))} \tag{1.26}$$

where ω_g is the effective plasma frequency, and taken to be the plasma frequency of gold, due to the consideration that the model should resemble the Drude model of gold for gap separation l=0; γ_g is the effective damping frequency, and is a function of gap distance l. The imaginary part of permittivity is related to the conductivity in the usual manner. We thus define the tunneling conductivity σ_0 as:

$$\sigma_0(l) = \frac{\omega_g^2}{4\pi\gamma_g(l)} \tag{1.27}$$

On the other hand, through full quantum mechanical calculations in the tunneling probability between two metallic parallel plates is considered, the tunneling conductivity σ_0 at the junction under bias $U=lE$ can be related to the tunneling current density J by:

$$\sigma_0(l) = l\,dJ/dU = l\frac{2}{(2\pi)^2}\int_0^{\Omega_F} T(\Omega,l)d\Omega \tag{1.28}$$

where Ω_F is the electron Fermi energy, $T(\Omega,l)$ is the energy Ω-dependent electron tunneling probability at each lateral position within the gap with separation l. Thus the separation dependent damping frequency can be obtained by combing Equation (1.27) and (1.28). Following this method, it is further found that γ_g generally follows an exponential increase with gap separation, given by:

$$\gamma_g(l) = \gamma_g(l=0)\exp(ql) \tag{1.29}$$

where $\gamma_g(l=0)$ is taken as the damping frequency of gold, as the effective Drude model should resemble that of gold for gap separation l=0; and q is a material dependent characteristic length from the exponential fit of $\gamma_g(l)$: for gold, q = 2.24 Å^{-1}.

The QCM can be implemented using classical electromagnetic simulations, with parameters as described above, to model the effect of electron tunneling. Figure 1.12 compares the predictions of a full quantum mechanical model, the QCM model, and a classical electromagnetic model of the extinction cross section and field enhancement gap for a dimer consisting of two sodium nanospheres with radii of 2.17 nm. There are three regimes can identified from the full quantum mechanical simulations in Figure 1.12(a)-(c). For gap distances D larger than 5 Å, no significant electron tunneling can occur. Thus the full quantum mechanical simulations in Figure 1.12(a)-(c) are almost identical to the CEM simulations of Figure 1.12(g)-(i). The lowest- energy boding dipolar plasmon (BDP)

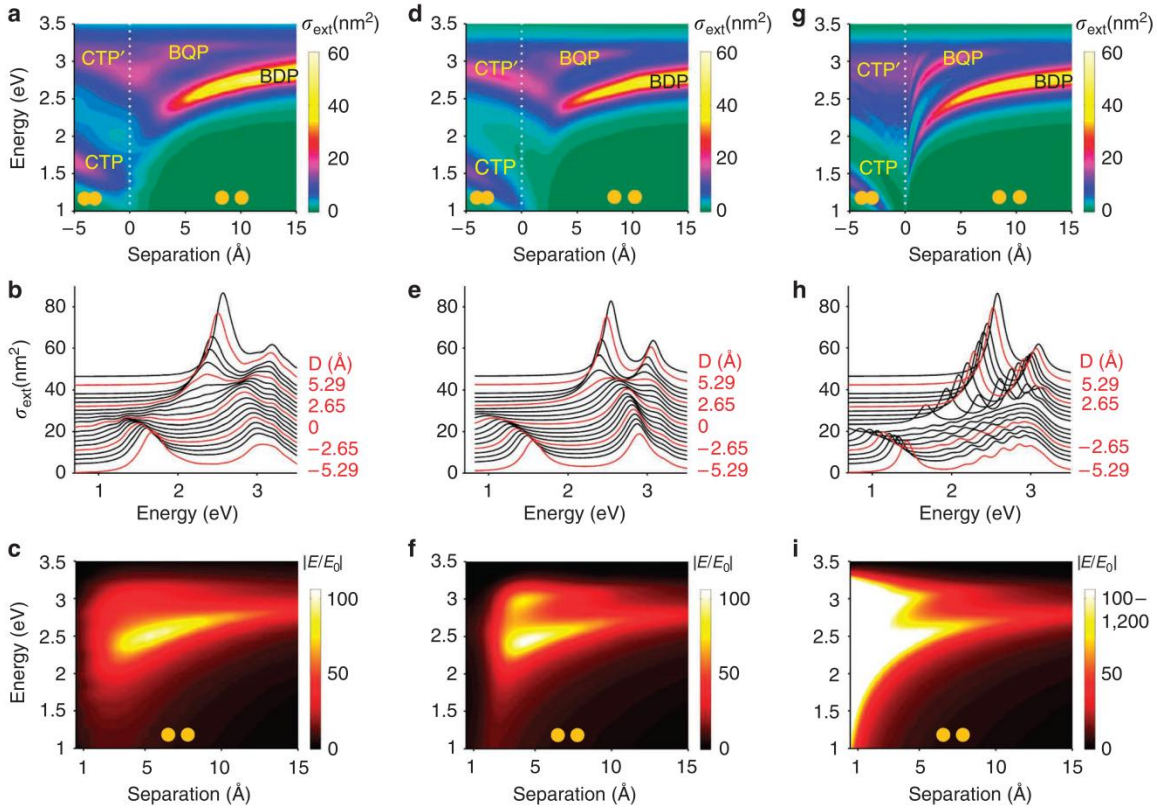

Figure 1.12 Optical response of a small metallic dimer simulated with quantum and classical models. (a-c) Full quantum mechanical simulations. (d-f) QCM simulations. (g-i) CEM simulations. Each row shows simulation of extinction cross section in color plot, extinction cross section in waterfall plot and field enhancement in gap center, respectively. (Adapted from Ref. [32])

and the bonding quadrupolar plasmon (BQP) at larger energy redshift as the separation distance becomes smaller. In the same regime, the field enhancement at resonance increase monotonically as the spheres approach each other. For gap distances *D* less than 1 Å, the conductance of the junction is large, either due to increased electron tunneling, or due to the two nanospheres becoming physically overlapped (for gaps < 0 Å). Charge transfer plasmon (CTP) modes are excited. These modes blue-shift with increasing overlap. CTPs are also predicted by CEM simulations, but only occur for overlapped structures. For gap distances *D* between 1 Å and 5 Å, the full quantum mechanical

simulations and CEM simulations show distinctively different features. In this regime, the full quantum mechanical simulations predict that the bonding modes gradually change to CTPs. This can be seen by examination of the extinction cross section plots. In addition, the field enhancement shows a considerable decrease in magnitude due to the emergence of electron tunneling. These features are not observed in the CEM simulations of Figure 1.12(g)-(i), but are successfully reproduced by the QCM simulations of Figure 1.12(d)-(f). This example demonstrates the effectiveness of the QCM method in modeling electron tunneling effect by classical simulations. In Chapter 6, we will employ this method for predicting the near- and far-field properties of planar dimer structure with angstrom scale gap widths. We will furthermore reveal the emergence of electron tunneling experimentally.

1.4 Surface-enhanced Raman scattering (SERS)

1.4.1 Raman scattering

The Raman process is a scattering phenomenon that is associated with the vibrational states of molecules. It was first discovered by Sir C. V. Raman in 1928. Raman scattering can be observed from most molecules. Here, we consider the Raman process using thiophenol as an example. This molecule is frequently used in Raman scattering investigations. Figure 1.13 shows its molecular structure and the Jablonski diagram. The thiophenol molecule consists of a benzene ring with an attached thiol group. Other than the electronic levels that are associated with the different energy levels of the electrons, the molecule also has vibrational states due to the fact that the relative positions of the

atoms that constitute the molecule can change. For example, the benzene ring can expand and shrink, leading to the "ring-breathing" mode of the molecule. The C-S bond can also be stretched or compressed, leading to the "C-S stretching" mode. The vibrational states are thus directly related to the molecular structure; measuring the energy levels of these states reveals the structure of the molecule.

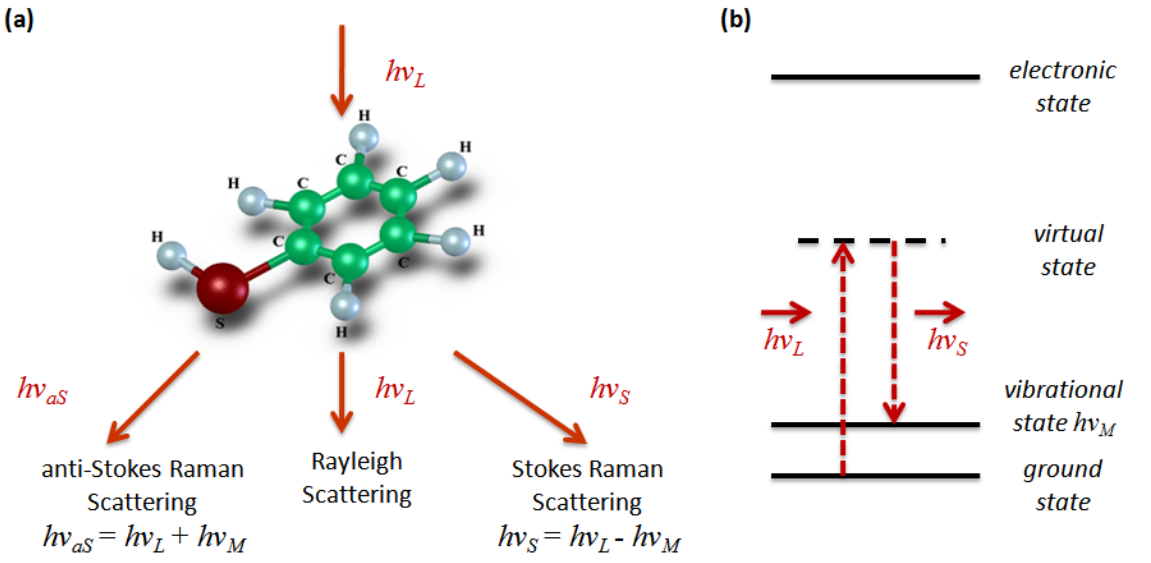

Figure 1.13 Raman scattering. (a) Light scattered by Raman molecule thiophenol. (b) Jablonski diagram of Stokes Raman scattering.

Raman scattering can be understood from the molecule's Jablonski diagram. Here, the scattering process can be considered to consist of the absorption of an incident photon and the spontaneous emission of a scattered photon. In the absorption process, the molecule is excited to a "virtual" state, as shown in Figure 1.13. This state is "virtual" in that it is an intermediate state in a multi-step quantum mechanical process: the final state of the molecule cannot be the "virtual" state; subsequent transitions ought to occur. In the quantum mechanical treatment of scattering processes, the "virtual" state can be viewed

as a mathematical construction of quantum mechanical perturbation theory. Almost immediately the molecule will emit a photon and return to a lower energy. In most cases, the emitted photon will have the same energy as the incident photon, and the molecule will return to its initial state; this is known as the "Rayleigh scattering". However, it is also possible that energy exchange occurs between the incident photon and the vibrational states of the molecule. This phenomenon is termed as "Raman scattering". Depending on the molecule's initial state, Raman scattering can take one of two categories. First, if the initial state of the molecule is the ground state, part of the incident photon energy will excite the molecule to one of its vibrational states, and the emitted photon will have less energy than the incident photon; this is known as the "Stokes Raman scattering". If the molecule is initially in one of its vibrational states, the emitted photon can have more energy than the incident photon, and the molecule returns to its ground state; this is known as the "anti-Stokes Raman scattering". In the remainder of this dissertation, the term "Raman scattering" typically refers to the "Stokes Raman scattering", unless otherwise emphasized.

To investigate the application of SPPs to Raman scattering, it is also useful to look at the classical model of Raman scattering. In classical electrodynamics, scattering from object whose size is much smaller than the wavelength can be approximated as being the radiation from a dipole. The moment of this dipole is induced by illumination by an external electromagnetic wave $\vec{E}$. These processes are shown in Figure 1.14. The Raman scattering process is modeled by defining the molecule's Raman polarizability $\vec{\alpha}_R$ such that the induced dipole moment $\vec{d}_R$ is given by:

$$\vec{d}_R = \vec{\alpha}_R \cdot \vec{E} \tag{1.30}$$

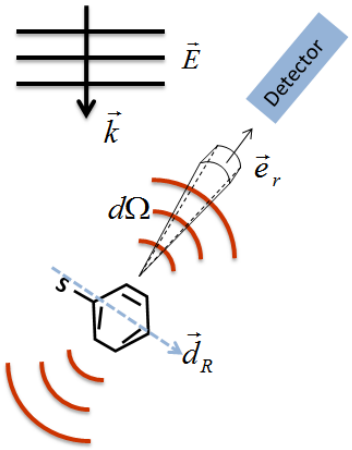

Figure 1.14 Classical model of Raman scattering. Raman scattering is modeled as the radiation from an induced Raman dipole.

The Raman polarizability $\vec{\alpha}_R$ is a tensor that is determined by the structure of the molecule. To find this tensor theoretically would require full quantum mechanical simulations of the molecule. The tensor is usually determined experimentally. To understand the connection between the scattered power and the Raman polarizability, we begin by considering the definition of scattering cross-section σ_{Scat}:

$$\sigma_{Scat} = P_{Scat} / I_{Inc} \tag{1.31}$$

where P_{Scat} is the measured scattering power, and I_{Inc} is the intensity of the illumination. The scattering cross-section into any given direction is given by the differential scattering cross-section:

$$\frac{d\sigma_{Scat}(\Omega)}{d\Omega} = \frac{dP_{Scat}(\Omega)}{d\Omega} \Big/ I_{Inc} \tag{1.32}$$

where Ω denotes the solid angle. In Raman scattering, each vibrational mode has its own differential scattering cross-section. The differential scattering cross-section is also a function of excitation wavelength. The differential Raman cross-section of the Raman

molecule typically refers to the value measured at the direction that is perpendicular to both the incident light and the incident polarization, also known as the 90°-configuration:

$$\frac{d\sigma_R}{d\Omega} = \frac{dP_R(90^\circ)}{d\Omega} \Big/ I_{Inc} \tag{1.33}$$

If the Raman scattering from the molecule is modeled as that from a linear dipole, the same differential Raman cross-section values are obtained for forward-scattering and back-scattering. For other detection directions, the radiation pattern of the molecule must be considered.

Now if we look back at the dipole approximation, the differential Raman cross-section can be related to the polarizability as:

$$\frac{d\sigma_R}{d\Omega} = \left(\frac{dP_{Rad}}{d\Omega}(90^\circ) \right) \Big/ I_{Inc} = \frac{\omega^4}{16\pi^2 \varepsilon_0^2 c^4} |\alpha_R|^2 \tag{1.34}$$

By measuring the scattering at 90° and by making use of Equations (1.33) and (1.34), the magnitude of Raman polarizability can be determined experimentally.

1.4.2 Surface enhanced Raman scattering (SERS)

Raman scattering is generally considered to be a very weak scattering process. For example, the total Raman cross-section (by integral of differential Raman cross-section over solid angle of 4π) for the 1581 cm^{-1} Raman line of a thiophenol molecule with excitation laser at 891 nm is measured to be 8.9×10^{-30} cm^2 [33]. For comparison, the absorption cross-section (related to fluorescence) of a Rhodamine 6G dye molecule with excitation laser at 532 nm is measured to be 4×10^{-16} cm^2 [34]. Raman scattering is therefore generally performed on large numbers of molecules.

Surface enhanced Raman scattering (SERS) is a technique that boosts Raman scattering signals. It was firstly discovered in the 1970s [35]. An example of a SERS measurement from this early work is shown in Figure 1.15. The upper figure shows a normal Raman scattering measurement from 50 mM pyridine in 0.1 M KCl solution. The two peaks at 1037 cm^{-1} and 1005 cm^{-1} correspond to the breathing modes of the pyridine ring. When a silver electrode is inserted into the solution, it is electrochemically roughened by KCl. At the same time, enhanced Raman scattering from pyridine is observed. The magnitude of the enhanced Raman scattering was initially attributed to the number of molecules adsorbed to the roughened electrode surface. It was realized, however, that the number of molecules involved was insufficient to account for the enhancement of the Raman signal. Rather, it was determined that the signal from each molecule was larger, i.e. "enhanced", due to the presence of the metal surface. This phenomenon is therefore referred to as "surface-enhanced" Raman scattering.

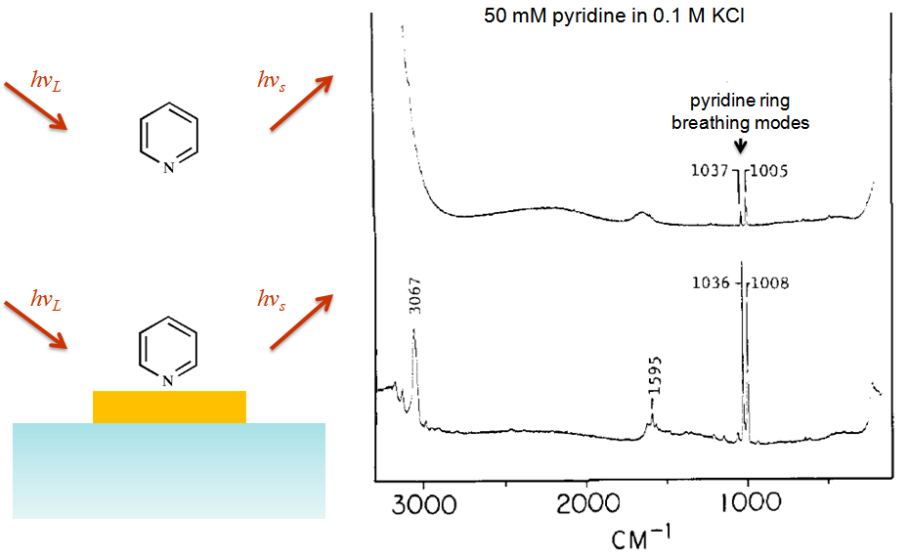

Figure 1.15 Surface enhanced Raman scattering observed from roughened electrode (Adapted from Ref. [35])

It is now generally understood that the enhancement of Raman scattering comes from two parts. In the classical model of Raman scattering, the induced Raman dipole moment is given by $\vec{d} = \vec{\alpha} \cdot \vec{E}$. The first part of the enhancement is the fact that, due to the presence of the metal surface in SERS, the Raman polarizability of the molecule can be larger, *i.e.* $|\alpha_{SERS}| > |\alpha_R|$. This is known as the "chemical enhancement" component of SERS. The second part of the enhancement is known as "electromagnetic enhancement". Due to plasmons excited on the metal, the local field at the position of the molecule can be larger that it would be, were the metal absent. In the emission process, the power radiated by a dipole with a given dipole moment can be larger due to the presence of the plasmonic nanostructure. The following two sections discuss these two enhancement mechanisms.

1.4.3 Chemical enhancement of SERS

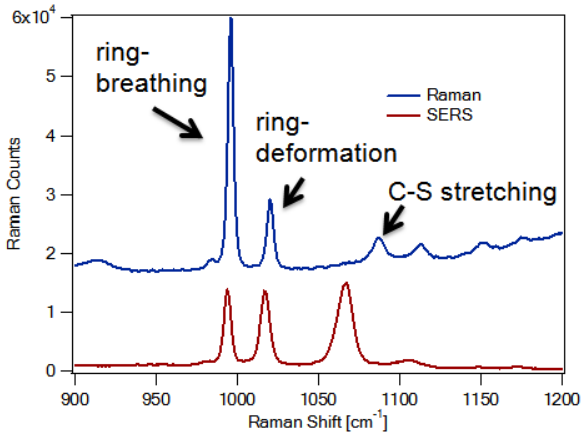

Figure 1.16 Raman and SERS spectra of thiophenol. Peak shift is observed for the C-S stretching mode. This mode also shows the largest enhancement.

There is some debate about the chemical enhancement mechanism. It can be indeed argued that the existence of chemical enhancement has still not been confirmed for all molecules. In this work, however, we frequently make use of thiophenol, for which it is generally agreed that chemical enhancement occurs. This can be seen by comparing its measured Raman scattering and SERS spectra (Figure 1.16). Three vibrational states can be seen, namely the ring-breathing mode, ring-deformation mode, and C-S stretching mode. A few observations can be made. First, the frequency of the C-S stretching mode is different in the SERS and Raman spectra, indicating a dramatic change in vibrational energy levels. Indeed, the thiol-group forms a chemical bond to the metals that are typically used in SERS (gold and silver) upon adsorption to the surface. It is also observed that the enhancement for the C-S stretching mode is much larger than the enhancements of the other two modes. Since the measurements are performed with laser excitation at 785 nm, these three modes only differ by about 10 nm in wavelength. The linewidth of plasmonic resonance is typically much larger than this wavelength span, meaning the change of electromagnetic enhancement over this wavelength range cannot explain the observed differences in the enhancements of these three modes. This supports the existence of chemical enhancement mechanism for thiophenol, especially for the C-S stretching mode.

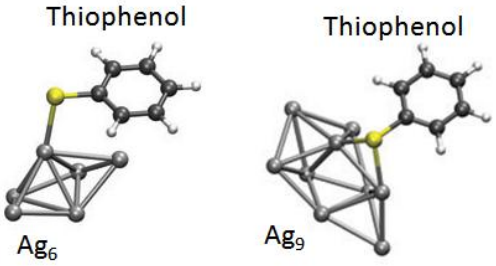

Figure 1.17 Adsorption of thiophenol on silver surface. The orientation of the molecule depends on the local cluster structure of the silver atoms. (Adapted from Ref. [36])

One mechanism that contributes to the chemical enhancement is associated with the adsorption of molecules on the surface, such as the binding sites and molecule orientation; this is termed “static chemical enhancement”. For example, the thiol group forms a chemical bond to metal surfaces such as gold and silver. This chemical boding changes the "static" Raman polarizability of the molecule. Saikin et al. calculated the Raman cross section of the thiophenol molecule when it binds to silver clusters using time-dependent density functional theory (TDDFT) [36]. The calculations show that the binding of thiophenol to silver clusters leads to an overall increase of the Raman cross sections of thiophenol. Moreover, as shown in Figure 1.17, depending on the structure of the silver atom cluster, the orientation of the thiophenol molecule can be different. For certain silver atom cluster structures, the calculated Raman cross section can be up to 10 times larger than that of isolated thiophenol. In addition to the "static" chemical enhancement, another mechanism that has been suggested is that of “resonance" enhancement that comes from “charge-transfer” transitions [37]. Figure 1.18 illustrates the Jablonski diagram of the molecule undergoing Raman scattering along with that of the metal. In the scattering process, the intermediate state does not have to be the “virtual” state described earlier, but can also be an unoccupied electronic state of the metal. In this model, the electron exchange exists during the absorption and emission part of the scattering process. The resultant Raman polarizability can be much larger than that of conventional Raman scattering (i.e. no metal surface). TDDFT calculations have shown that the charge-transfer mechanism could contribute a factor up to 10^2-10^3 to the overall SERS enhancement [36-38].

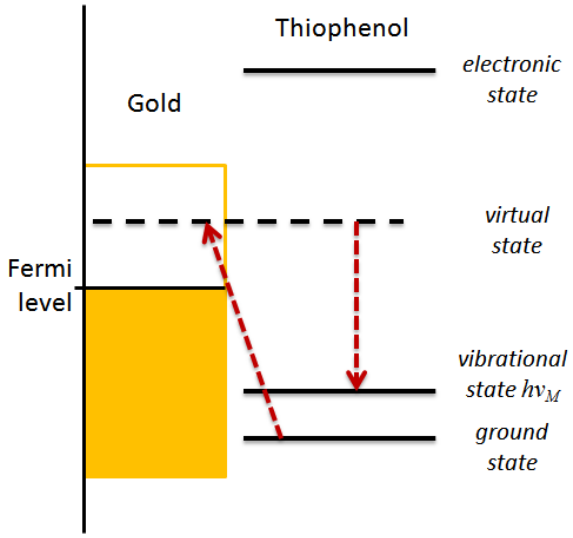

Figure 1.18 Jablonski diagram of charge-transfer mechanism of SERS. Electrons can transfer between the unoccupied states of gold and the thiophenol molecule.

1.4.4 Electromagnetic enhancement of SERS

The electromagnetic enhancement mechanism in SERS can be understood using classical electromagnetics. While debate continues regarding the nature of chemical enhancement, it is generally agreed that electromagnetic enhancement dominates in determining the total SERS enhancement. In what follows, I will show that by placing the molecule in the vicinity of a plasmonic nanostructure, provided that certain assumptions regarding the experimental configuration, the plasmon nanostructure and the molecule hold, the Raman scattering is enhanced by a factor equal to the fourth power of the local field enhancement. This is often referred as the $|E|^4$ approximation in SERS [39].

As shown in Section 1.4.1, in the classical model, a field $\vec{E}_0$ at frequency ω_{L} is incident on the molecule, thereby inducing a Raman dipole $\vec{d}_R = \vec{\alpha}_R \cdot \vec{E}_0$. Raman scattering is the radiation from this dipole at the Raman frequency ω_{R} with power

proportional to $\left|\vec{d}_R\right|^2$. This radiation is detected in the far field. As described below, in the SERS phenomenon, the electromagnetic enhancement originates from both excitation and radiation processes:

(1) Due to the plasmon resonance, the amplitude of the field $\vec{E}_{Loc}$ close to the metallic surfaces can be much larger than $\left|\vec{E}_0\right|$, leading to a local intensity enhancement factor $M_{Loc}(\omega_L)$ that contributes to enhancement of the SERS signal. Here, we assume the Raman tensor is isotropic, thus we have:

$$M_{Loc} = \left|\vec{E}_{Loc}\right|^2 \Big/ \left|\vec{E}_0\right|^2 \tag{1.35}$$

(2) The Raman dipole emission at frequency ω_R is affected by the plasmon nanostructure in two ways. First, the total radiated power can be enhanced through excitation of plasmon resonances of the nanostructure. Second, the radiation pattern can also be altered by the radiation pattern of the plasmon mode of the nanostructure. These effects lead to the radiated power per unit solid angle in a given (detection) direction $dP/d\Omega$ being modified by a radiation enhancement factor $M_{Rad}(\omega_R)$.

We now obtain $M_{Rad}(\omega_R)$ for the case of a back-scattered configuration, wherein Raman scattering is detected along the direction that is opposite to that of the incident plane wave (Figure 1.19(a)). In this configuration, the source Raman dipole $\vec{d}_R$ at position *O* is near the plasmon nanostructure, and generates the field $\vec{E}_\theta$ at the position of the detector *M*. Now we consider the reciprocal process by exchanging the positions of the dipole and detector (Figure 1.19(b)). We now have the situation where the dipole $\vec{d}_2$

radiates at position *M*, thereby generating a field $\vec{E}_2$ at position *O*. The optical reciprocity theorem [38] states that:

$$\vec{d}_2 \cdot \vec{E}_\theta = \vec{d}_R \cdot \vec{E}_2 \tag{1.36}$$

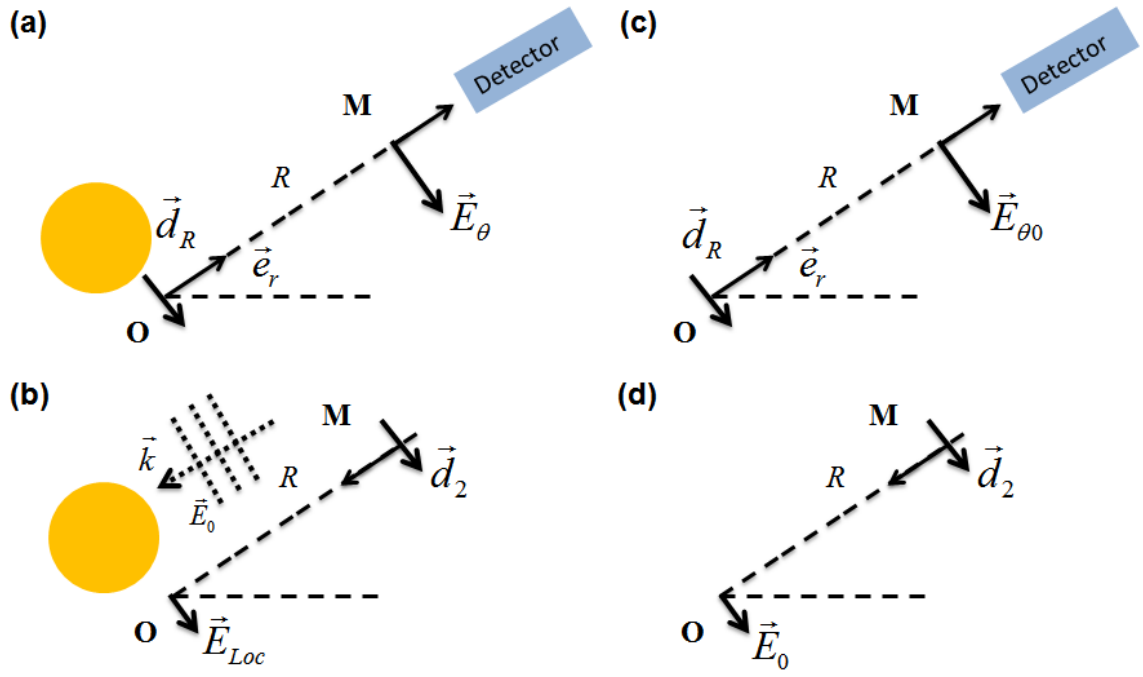

Figure 1.19 Radiation enhancement in SERS. (a) Schematic of Raman scattering in SERS. (b) Reciprocal process to Raman radiation in SERS. (c) Schematic of Raman scattering in conventional Raman (not SERS). (d) Reciprocal process to Raman radiation in conventional Raman (not SERS).

In a SERS experiment, the distance between *M* and *O* is usually very large compared to the wavelength. In Figure 1.19(b), therefore, the radiation from dipole $\vec{d}_2$ can be considered to be a plane wave when it reaches the plasmon nanostructure and point *O*. This reciprocal case thus is identical to the configuration used in the calculation of the near-field enhancement provided by a plasmon nanostructure under plane wave

excitation, meaning that $\vec{E}_2 = \vec{E}_{Loc}$. Moreover, since we have assumed the Raman tensor is isotropic, the induced Raman dipole $\vec{d}_R$ should be parallel to $\vec{E}_{Loc}$. We also assume a polarizer is placed in front of the detector to ensure that $\vec{d}_2$ is parallel to $\vec{E}_\theta$. The amplitude of the field at the detector position *M* is then given by:

$$E_\theta = d_R E_{Loc} / d_2 \tag{1.37}$$

A similar treatment can also be performed for conventional Raman scattering, *i.e.* without the plasmon nanostructure. The configurations are shown in Figure 1.19(c) and (d). The detected field amplitude at position M is given by:

$$E_{\theta 0} = d_R E_0 / d_2 \tag{1.38}$$

Here, E_{Loc} is replaced by E_0 due to the fact that the radiation from $\vec{d}_2$ at position *M* generates a plane wave with amplitude of E_0 at position *O*. By comparing Equations (1.37) and (1.38), the radiation enhancement factor $M_{Rad}(\omega_R)$ is found to be:

$$M_{Rad}(\omega_R) = \left| \frac{E_\theta}{E_{\theta 0}} \right|^2 = |E_{Loc}|^2 / |E_0|^2 \tag{1.39}$$

The total electromagnetic enhancement factor can thus be obtained by multiplying the local field enhancement factor and the radiation enhancement factor:

$$EF_{EM} = M_{Loc}(\omega_L) M_{Rad}(\omega_R) = |E_{Loc}|^4 / |E_0|^4 \tag{1.40}$$

which is the $|E|^4$ approximation for SERS. In deriving this, we have made five assumptions: (1) plane-wave excitation is employed; (2) only the back-scattered Raman signal is detected; (3) the component of the Raman scattering that is polarized parallel to the excitation polarization is detected; (4) the Raman tensor is isotropic; (5) the Stokes shift is zero. If these assumptions do not hold, then the electromagnetic enhancement

factor is not exactly equal to $|E|^4$. In most cases, however, the $|E|^4$ approximation holds to within an order-of-magnitude. In the following chapters, we will use this approximation to estimate SERS enhancement factors from numerical simulations. In some cases, we will calculate field enhancements at laser and Stokes wavelengths; i.e. assumption (5) will not be made.

The above derivation also emphasizes that a sufficiently large SERS enhancement factor is necessary to observe Raman scattering if the number of molecules is small. From Equation (1.30), it can be seen that the detected Raman signal is linearly proportional to the intensity of the external field. The same scaling relation exists for other linear optical process such as fluorescence. If the SERS enhancement factor is small, the Raman signal becomes buried in the background continuum, which can be fluorescence from the molecules undergoing the Raman scattering, or fluorescence from other molecules, or 1-photon luminescence of the metallic nanostructure. Since the intensities of all these components scale linearly with the intensity of the applied field, Raman scattering cannot be separated from the background simply by applying more power. On the other hand, consider that SERS intensity scales as the fourth power of the near-field enhancement, while surface-enhanced fluorescent intensity scales as the square of the near-field enhancement [40]. Therefore, large field "enhancement", rather than large field "intensity", is necessary to separate Raman scattering from the background continuum.

1.4.5 Measurement of SERS enhancement factor

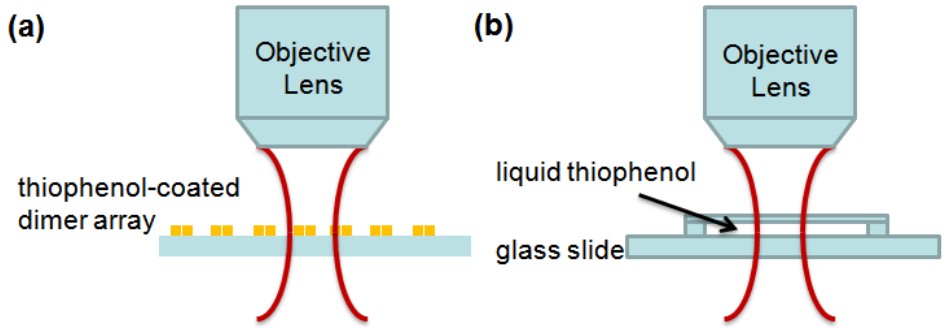

Figure 1.20 Schematic illustration of experimental configurations used for measurement of SERS enhancement factor. (a) SERS configuration. (b) Reference non-SERS (i.e. Raman) configuration.

Experimentally, the SERS enhancement factor for an individual plasmonic dimer is found from

$$EF = \frac{I_{SERS} / N_{SERS}}{I_{REF} / N_{REF}} \tag{1.41}$$

where I_{SERS} and I_{REF} are the intensities of a specific Raman line for the SERS configuration and reference non-SERS configuration, respectively. We consider the case of quantifying the SERS enhancement of thiophenol on pairs of gold nanostructures ("dimers"). In this thesis, we often consider the SERS enhancement of the Raman line of pure thiophenol at 1093 cm^{-1} that shifts to 1074 cm^{-1} in the SERS measurements [36]. The experimental setups are shown schematically as Figure 1.20. The intensity measured in each configuration is calculated as the integral of the Raman line of the measured spectrum. The background is subtracted before this integration is performed. The intensity is normalized by the laser power and CCD integration time. N_{SERS} and N_{REF} are the numbers of probed molecules in the laser spot for the SERS substrate and reference sample, respectively. For N_{SERS}, it is assumed that the thiophenol SAM is formed on all exposed surfaces of the gold dimers, i.e. on the top surfaces as well as on the side walls.

We assume that the thiophenol surface density is $\rho_s = 6.8 \times 10^{14}$ cm^{-2} [41]. N_{SERS} is thus given by $N_{SERS} = N_{dimer}\, \rho_s S$, where N_{dimer} is the number of dimers within the laser spot.

The number of molecules in the reference measurements, $N_{REF,}$ is calculated using the molecular weight and volume density of thiophenol, together with the detection volume. Following the approach of Le Ru et al. [42], the detection volume can be estimated as hA_{Laser}, where h is the effective height of the scattering volume, and A_{Laser} is the area of laser spot. The effective height h is measured by translating a reference silicon sample vertically through the focal volume, and recording the Raman signal at each vertical position. It is then calculated as the integral of the curve plotting the Raman intensity (for 520 cm^{-1} Raman line) as a function of vertical position, divided by the maximum Raman intensity. The value of the effective height is strongly related to the configuration of the experimental setup, such as the choice of the objective lens and the laser wavelength. Therefore, the effective height is measured for each group of measurements. In Chapter 2, the SERS measurements are made with an objective lens with a magnification of 20× and numerical aperture (NA) of 0.4. The measured effective height is 186 μm for a laser wavelength of 785 nm. In Chapter 3-5, the SERS measurements are made with an oil-immersion objective lens with a magnification of 100× and NA of 1.4. The measured effective height is 17.2 μm for a laser wavelength of 785 nm. In Chapter 6, the SERS measurements are made with an objective lens with a magnification of 100× and NA of 0.9. The measured effective height is 9.6 μm for a laser wavelength of 825 nm. Due to the limited choice of the long-pass/short-pass filters, this effective height is only measured for excitation laser at 825 nm. The values at other wavelengths are obtained by scaling the effective height h by a factor of (λ/825nm). A_{Laser}

is estimated from the image produced by the objective lens. This is determined at each laser wavelength. N_{REF} is found using $N_{REF} = N_A \rho h A_{Laser}/M$, where N_A is Avogadro's number, ρ is the thiophenol density, and M is the molar mass of thiophenol molecules.

References

[1] E. Ozbay, "Plasmonics: merging photonics and electronics at nanoscale dimensions.," Science **311**, 189–193 (2006).

[2] C. Kittel, *Introduction To Solid State Physics*, 8th ed. (John Wiley & Sons, Inc., 2005).

[3] E. Kretschmann and H. Raether, "Radiative decay of non-radiative surface plasmons excited by light," Z. Naturforsch. **23A**, 2135–2136 (1968).

[4] H. J. Lezec, A. Degiron, E. Devaux, R. a Linke, L. Martin-Moreno, F. J. Garcia-Vidal, and T. W. Ebbesen, "Beaming light from a subwavelength aperture.," Science **297**, 820–2 (2002).

[5] W. Zhu, A. Agrawal, and A. Nahata, "Direct measurement of the Gouy phase shift for surface plasmon-polaritons.," Opt. Express **15**, 9995–10001 (2007).

[6] T. W. Ebbesen, H. J. Lezec, H. F. Ghaemi, T. Thio, and P. A. Wolff, "Extraordinary optical transmission through subwavelength hole arrays," Nature **391**, 667–669 (1998).

[7] T. Xu, A. Agrawal, M. Abashin, K. J. Chau, and H. J. Lezec, "All-angle negative refraction and active flat lensing of ultraviolet light," Nature **497**, 470–474 (2013).

[8] W. Zhu, A. Agrawal, and A. Nahata, "Planar plasmonic terahertz guided-wave devices.," Opt. Express **16**, 6216–26 (2008).

[9] R. F. Oulton, V. J. Sorger, T. Zentgraf, R. Ma, C. Gladden, L. Dai, G. Bartal, and X. Zhang, "Plasmon lasers at deep subwavelength scale," Nature **461**, 629–632 (2009).

[10] K. Wang, E. Schonbrun, and K. B. Crozier, "Propulsion of gold nanoparticles with surface plasmon polaritons: evidence of enhanced optical force from near-field coupling between gold particle and gold film," Nano Lett. **9**, 2623–2629 (2009).

[11] N. Yu, J. Fan, Q. J. Wang, C. Pflügl, L. Diehl, T. Edamura, M. Yamanishi, H. Kan, and F. Capasso, "Small-divergence semiconductor lasers by plasmonic collimation," Nat. Photonics **2**, 564–570 (2008).

[12] A. Polman and H. A. Atwater, "Photonic design principles for ultrahigh-efficiency photovoltaics," Nat. Mater. **11**, 174–177 (2012).

[13] T. Ellenbogen, K. Seo, and K. B. Crozier, "Chromatic plasmonic polarizers for active visible color filtering and polarimetry.," Nano Lett. **12**, 1026–31 (2012).

[14] J. B. Pendry, a. J. Holden, D. J. Robbins, and W. J. Stewart, "Magnetism from conductors and enhanced nonlinear phenomena," IEEE Trans. Microw. Theory Tech. **47**, 2075–2084 (1999).

[15] N. Yu, P. Genevet, M. a Kats, F. Aieta, J.-P. Tetienne, F. Capasso, and Z. Gaburro, "Light propagation with phase discontinuities: generalized laws of reflection and refraction.," Science **334**, 333–337 (2011).

[16] N. Yu and F. Capasso, "Flat optics with designer metasurfaces," Nat. Mater. **13**, 139–150 (2014).

[17] J. P. Camden, J. a Dieringer, Y. Wang, D. J. Masiello, L. D. Marks, G. C. Schatz, and R. P. Van Duyne, "Probing the structure of single-molecule surface-enhanced Raman scattering hot spots," J. Am. Chem. Soc. **130**, 12616–12617 (2008).

[18] D. Wang, W. Zhu, M. D. Best, J. P. Camden, and K. B. Crozier, "Directional Raman scattering from single molecules in the feed gaps of optical antennas," Nano Lett. **13**, 2194–2198 (2013).

[19] M. Righini, P. Ghenuche, S. Cherukulappurath, V. Myroshnychenko, F. J. García de Abajo, and R. Quidant, "Nano-optical trapping of Rayleigh particles and Escherichia coli bacteria with resonant optical antennas," Nano Lett. **9**, 3387–3391 (2009).

[20] K. D. Ko, A. Kumar, K. H. Fung, R. Ambekar, G. L. Liu, N. X. Fang, and K. C. Toussaint, "Nonlinear optical response from arrays of Au bowtie nanoantennas.," Nano Lett. **11**, 61–5 (2011).

[21] Y. Zhang, F. Wen, Y.-R. Zhen, P. Nordlander, and N. J. Halas, "Coherent Fano resonances in a plasmonic nanocluster enhance optical four-wave mixing.," Proc. Natl. Acad. Sci. U. S. A. **110**, 9215–9219 (2013).

[22] L. Novotny and B. Hecht, *Principles of Nano-Optics* (Cambridge University Press, 2007).

[23] P. B. Johnson and R. W. Christy, "Optical constants of the noble metals.," Phys. Rev. B **6**, 4370–4379 (1972).

[24] Z. Yu and S. Fan, "Extraordinarily high spectral sensitivity in refractive index sensors using multiple optical modes.," Opt. Express **19**, 10029–10040 (2011).

[25] K. Wang, E. Schonbrun, and K. B. Crozier, "Propulsion of gold nanoparticles with surface plasmon polaritons: evidence of enhanced optical force from near-field coupling between gold particle and gold film.," Nano Lett. **9**, 2623–2629 (2009).

[26] J. M. McMahon, S. K. Gray, and G. C. Schatz, "Optical properties of nanowire dimers with a spatially nonlocal dielectric function," Nano Lett. **10**, 3473–3481 (2010).

[27] C. Cirac ì, R. T. Hill, J. J. Mock, Y. Urzhumov, A. I. Fern ández-Dom ínguez, S. A. Maier, J. B. Pendry, A. Chilkoti, and D. R. Smith, "Probing the ultimate limits of plasmonic enhancement," Science **337**, 1072–1074 (2012).

[28] J. Zuloaga, E. Prodan, and P. Nordlander, "Quantum description of the plasmon resonances of a nanoparticle dimer," Nano Lett. **9**, 887–891 (2009).

[29] K. J. Savage, M. M. Hawkeye, R. Esteban, A. G. Borisov, J. Aizpurua, and J. J. Baumberg, "Revealing the quantum regime in tunnelling plasmonics," Nature **491**, 574–577 (2012).

[30] G. Toscano, S. Raza, A.-P. Jauho, N. A. Mortensen, and M. Wubs, "Modified field enhancement and extinction by plasmonic nanowire dimers due to nonlocal response," Opt. Express **20**, 4176–4188 (2012).

[31] Y. Luo, A. I. Fernandez-Dominguez, A. Wiener, S. A. Maier, and J. B. Pendry, "Surface Plasmons and Nonlocality: A Simple Model," Phys. Rev. Lett. **111**, 093901 (2013).

[32] R. Esteban, A. G. Borisov, P. Nordlander, and J. Aizpurua, "Bridging quantum and classical plasmonics with a quantum-corrected model," Nat. Commun. **3**, 825 (2012).

[33] R. L. Aggarwal, L. W. Farrar, E. D. Diebold, and D. L. Polla, "Measurement of the absolute Raman scattering cross section of the 1584-cm^{-1} band of benzenethiol and the surface-enhanced Raman scattering cross section enhancement factor for femtosecond laser-nanostructured substrates," J. Raman Spectrosc. **40**, 1331–1333 (2009).

[34] W. Holzer, H. Gratz, T. Schmitt, A. Penzkofer, A. Costela, R. Sastre, and F. J. Duarte, "Photo-physical characterization of rhodamine 6G in a," Chem. Phys. **256**, 125–136 (2000).

[35] D. L. Jeanmaire and R. P. Van Duyne, "Surface Raman spectroelectrochemistry," J. Electroanal. Chem. **84**, 1–20 (1977).

[36] S. K. Saikin, R. Olivares-Amaya, D. Rappoport, M. Stopa, and A. Aspuru-Guzik, "On the chemical bonding effects in the Raman response: benzenethiol adsorbed on silver clusters.," Phys. Chem. Chem. Phys. **11**, 9401–9411 (2009).

[37] J. R. Lombardi, R. L. Birke, T. Lu, and J. Xu, "Charge-transfer theory of surface enhanced Raman spectroscopy : Herzberg-Teller contributions," J Chem. Phys. **10031**, 4174–4180 (1986).

[38] L. Zhao, L. Jensen, and G. C. Schatz, "Pyridine - Ag_{20} Cluster : A Model System for Studying Surface-Enhanced Raman Scattering," **128**, 2911–2919 (2006).

[39] E. C. Le Ru and P. G. Etchegoin, "Rigorous justification of the $|E|^4$ enhancement factor in Surface Enhanced Raman Spectroscopy," Chem. Phys. Lett. **423**, 63–66 (2006).

[40] A. Kinkhabwala, Z. Yu, S. Fan, Y. Avlasevich, K. Müllen, and W. E. Moerner, "Large single-molecule fluorescence enhancements produced by a bowtie nanoantenna," Nat. Photon. **3**, 654–657 (2009).

[41] A. D. McFarland, M. A. Young, J. A. Dieringer, and R. P. Van Duyne, "Wavelength-scanned surface-enhanced Raman excitation spectroscopy," J. Phys. Chem. B **109**, 11279–11285 (2005).

[42] E. C. LeRu, M. Meyer, and P. G. Etchegoin, "Surface Enhanced Raman Scattering Enhancement Factors: A Comprehensive Study," J. Phys. Chem. C **111**, 13794–13803 (2007).

Chapter 2 Lithographically fabricated plasmonic optical antennas with gap-widths well below 10 nm

Metal nanostructures that efficiently capture or radiate electromagnetic waves at optical frequencies offer a means to concentrate electromagnetic energy into deep sub-wavelength regions. Wessel noted that these structures can therefore be considered antennas [1]. Recent work has focused on more efficient designs, termed "optical antennas", which employ small gaps or very sharp tips [2–4]. Optical antennas present opportunities for ultra-sensitive spectroscopy, near-field scanning optical microscopy and compact subwavelength light sources [5–7]. However, the achievable feature sizes are usually determined by fabrication, being approximately given by the gap size or tip sharpness. Here, we report a top-down fabrication procedure to fabricate pairs of nanoparticles separated by a controllable gap size that can be as small as 3 nm. As an application, we show that the enhancement factors of surface-enhanced Raman scattering (SERS) increase significantly for smaller gap sizes, indicating greatly enhanced electromagnetic field within the gaps. We anticipate that the fabrication method we introduce here for nanoparticle pairs with nanoscale gaps would be useful not only for SERS, where it could potentially enable single molecule sensitivity, but also for other applications in plasmonics.

2.1 Lithographic nanofabrication using sacrificial layer

SERS has attracted renewed attention since the first demonstrations of single-molecule sensitivity [8,9]. Increasing the adoption of the SERS technique further, however, requires fabrication methods capable of routinely delivering reproducible substrates with high enhancement factors. Dimer structures, consisting of two metallic nanoparticles closely placed together, are among the simplest optical antenna structures that are confirmed to be single-molecule SERS active [10,11]. It is believed that the substantial electromagnetic field generated in dimer gaps is one of the main enhancement mechanisms in single-molecule SERS [12,13]. This motivates the development of a reproducible method for the fabrication of dimers with very small gaps, especially below 10 nm. Dimers patterned by electron-beam lithography (EBL) allow flexible design and controllable gap size, but face difficulties for gap sizes smaller than 10 nm, because of resolution limitations [14], although such small features have been demonstrated using advanced lithography tools or special substrates [15,16]. There have also been numerous efforts in fabricating reproducible dimer structures with sub-10nm gaps using chemical synthesis methods [17,18]. However, flexible control of dimer dimensions and location on device substrates is not easily available with chemical synthesis. Other proposed methods to achieve sub-10nm gaps include break junctions [19], electromigration [20], electrodeposition [21], and sacrificial-layers [22–25]. The fabrication of resonant optical dimer antennas, however, was not demonstrated in these previous works. In this work, we demonstrate arrays of dimers with controllable gap size well below 10 nm by combining EBL with the use of sacrificial layers. The measured SERS enhancement factors increase almost by two orders of magnitude by reducing the gap size from ~20 nm to ~3 nm. This

significant improvement confirms that there is substantial electromagnetic field generated within dimer gaps.

2.1.1 Fabrication steps

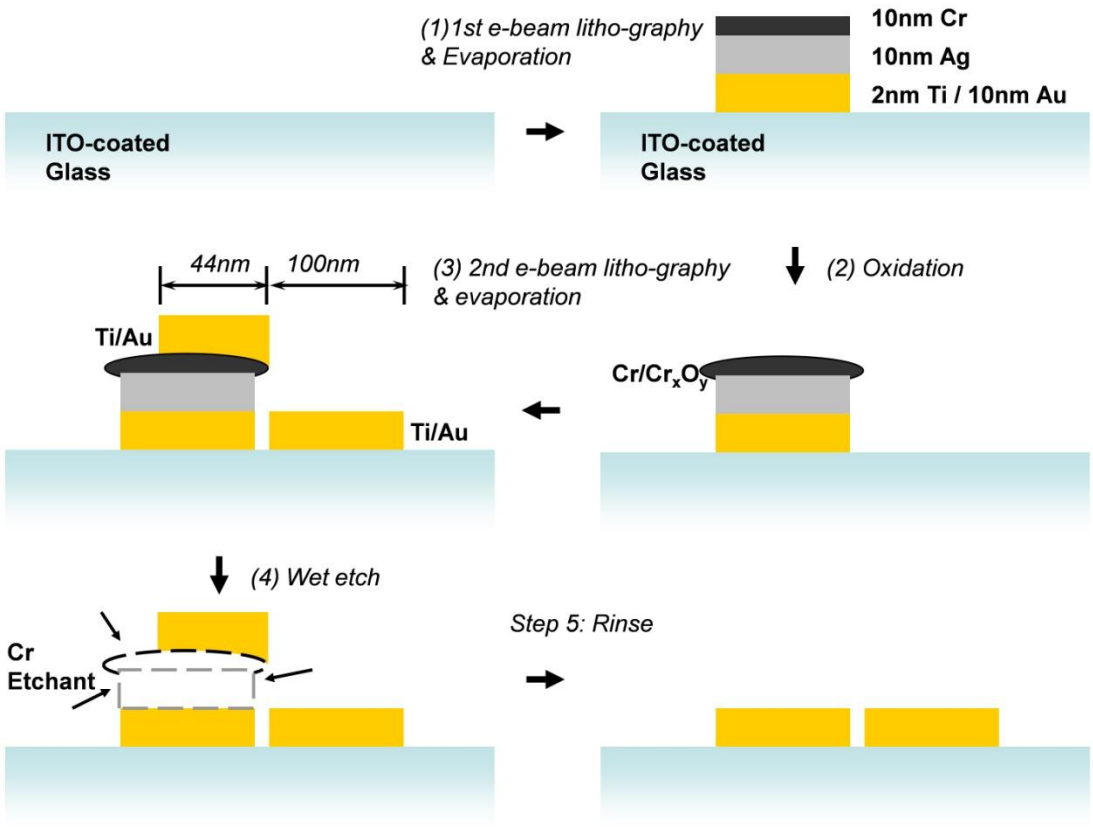

Figure 2.1. Schematic diagram of lithographic nanofabrication using sacrificial layer.

The fabrication method is shown schematically in Figure 2.1. The fabrication sequence was designed to yield a periodic array of dimer antennas, i.e. paired gold nanoparticles (Figure 2.2(a)), in which each nanoparticle consisted of a rectangle 100 nm long, 80 nm wide and 30 nm thick (Figure 2.2(b)). The outer edges of the nanoparticles were designed to be rounded, with a radius of curvature of 40 nm. The nanoparticle

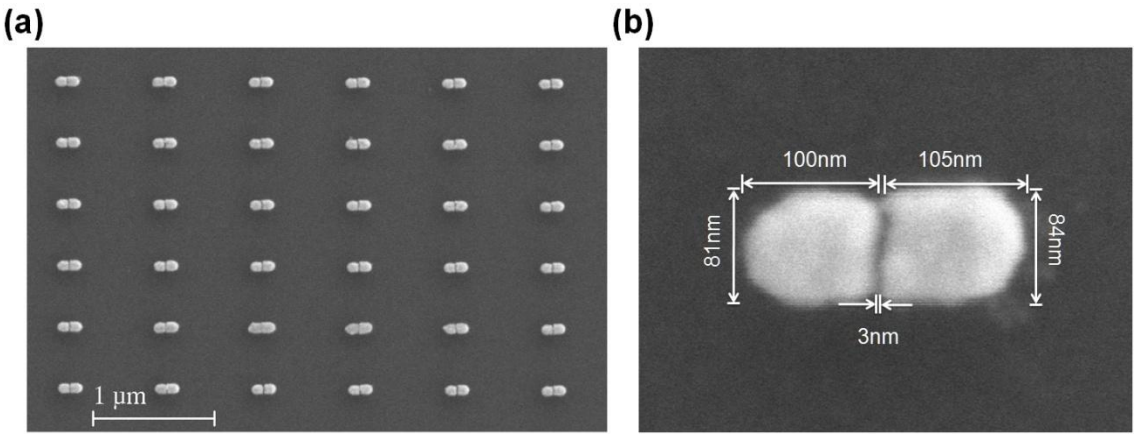

Figure 2.2. SEM images of fabricated dimers. (a) SEM of a fabricated dimer array obtained with 50K× magnification. (b) SEM of a dimer structure of fabricated array of (a), obtained with 420K× magnification.

dimers were fabricated in a two dimensional array, with the unit cell being 800 nm × 500 nm; and the overall size of each array being 70 μm × 70 μm. Indium tin oxide (ITO) coated glass (Sigma-Aldrich, surface resistivity 60-100 Ω/sq) was used as the substrate. SiO_2 was initially deposited on top of the ITO layer using plasma enhanced chemical vapor deposition (Nexx® PECVD) to a thickness of 50 nm to isolate the ITO-layer from the wet etching process. As shown in Figure 2.1, in Step (1), the left side of the dimer structure was defined by conventional EBL (Elionix® ELS-7000) and lift-off processes. Two alignment mark patterns, separated by 2.1 mm, were also fabricated in this step. In the evaporation step, titanium (2 nm, adhesion layer), gold (30 nm), silver (30 nm) and chromium (10 nm) were deposited. Evaporation rates for these materials were all set to be 1.5 Å/s. The lift-off process was then carried out, with the sample being soaked in acetone for > 4 hrs. In Step (2), the chromium layer was oxidized, either in ambient conditions (Figure 2.3(a)), or in an oxygen plasma stripper (Figure 2.3(b)) for a specific time, with 50 sccm O_2 flow rate and 20 W plasma power (Technics® Plasma Stripper).

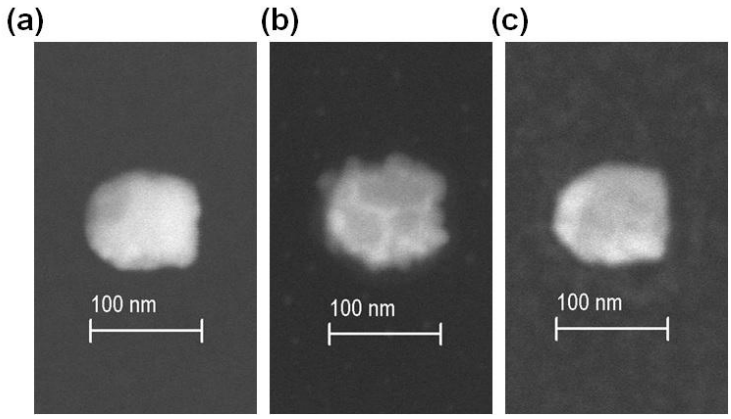

Figure 2.3. SEM of the effect of chromium oxidation. (a) After ambient oxidation. (b) 2 min oxygen plasma. (c) Pattern without silver/chromium layer produced for comparison purposes, obtained by etching the left-side pattern with chromium etchant just after the oxidation process.

As a result of the oxidation, the chromium layer expanded laterally on the order of several nanometers, resulting in it overhanging the edge of the silver layer. This can be seen by comparing Figure 2.3(a) and (b) with Figure 2.3(c). In Step (3), the right side of the dimer was defined by a second EBL, in which alignment marks were employed. In the evaporation step, only titanium (adhesion layer) and gold were deposited. The lift-off process usually took > 12 hrs. The length of the exposed pattern was chosen to be 144 nm, to result in an intentional overlap of 40 nm with the left side pattern, taking into account an anticipated lateral expansion of chromium layer of ~4 nm. During evaporation, therefore, the length of the nanoparticle formed on the substrate is 100 nm, with the remainder (44 nm) being deposited onto the chromium layer. Through this method, the alignment error typically achieved (<10 nm) between the first and second lithography steps do not modify the gap size, and only results in an alteration of the length of the right side nanoparticle that is a small fraction of its total length. In Step (4), the sample was then immersed in Chromium Etchant 1020 (Transene® Inc.) for 2 hrs. The silver and

chromium layers, along with the gold layer on top of them deposited in the second evaporation process, were wet etched away by etchant applied using a squeeze bottle. Finally, the sample was rinsed thoroughly and dried in Step (5), resulting in an array of dimers. It can be seen that the chromium layer served as the mask layer in this fabrication; the thickness is selected to ensure that the final gap size is well below 10 nm. The silver served as the spacer layer: it formed an undercut structure beneath the chromium layer, in a similar manner to a bilayer resist in typical lift-off processes. It was found that the thickness of the silver layer is crucial to the overall yield of nanoscale gaps, as the chromium layer would be otherwise too thin to separate the gold patterns.

Figure 2.2(a) shows scanning-electron microscope (SEM) images of a fabricated dimer array. Of the 6×6 dimer structures in the figure, 29 are considered "good", a yield of ~81%. Here, a "good" dimer is defined as a structure with no connections within the gap and no broken patterns. We believe that gap connections may have come from titanium/gold residues during the wet etching in Step (4) in Figure 2.1, or the evaporation in the Step (3) being not perfectly normal to the surface. Broken patterns, although not observed in Figure 2.2(a), may come from the wet etching step when removing silver and chromium. Figure 2.2(b) shows a high magnification SEM of a fabricated dimer. From the SEM, the gap size, here defined as the separation between the closest two points within the gap, is found to be 3 nm (see following discussions). The standard deviation of the gap sizes measured from 9 dimers within this array is ~1 nm. The fabrication results clearly demonstrate the ability of the method to fabricate dimer arrays with gaps well below 10 nm.

2.1.2 Determining gap size

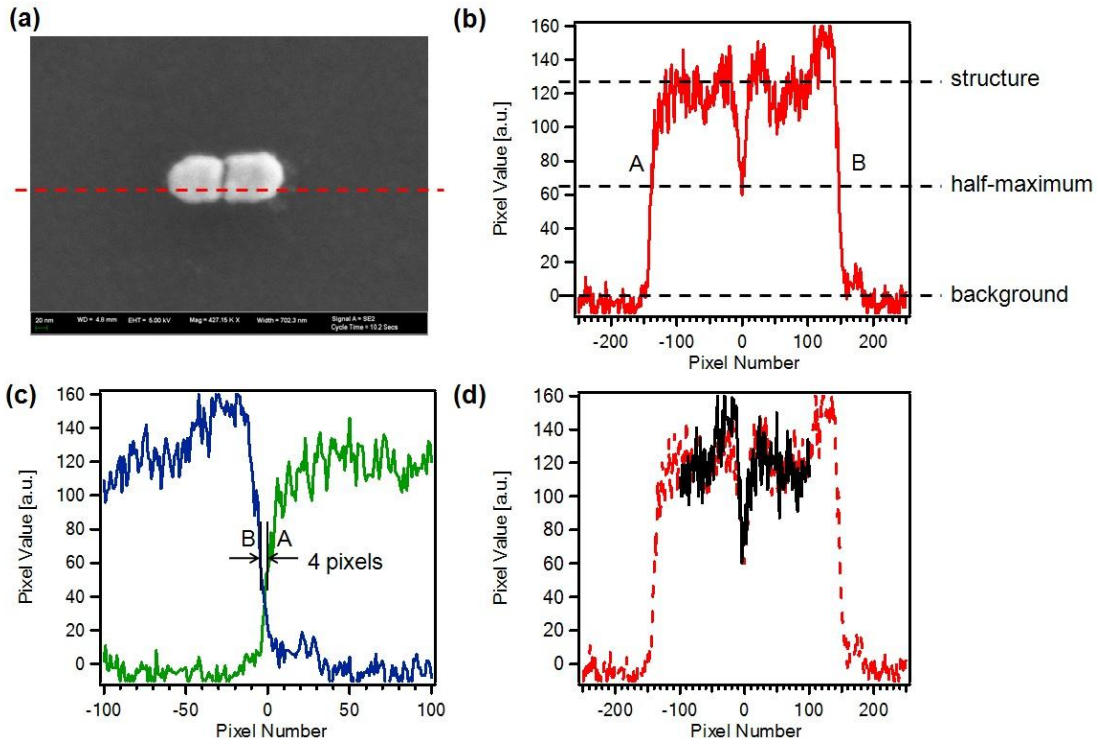

Figure 2.4. Characterization of gap size. (a) SEM of dimer structure obtained at 420K× magnification. Red dotted line represents the cross-section where b was taken. (b) Pixel brightness value of the cross-section. Background line is set to be at 0; line through structure is at 128; and half-maximum line is at 64. (c) Left edge (green) and right edge (blue) with A and B offset by 4 pixels. (d) The reconstructed dip (black solid line) with A and B offset by 4 pixels (3 nm). Also shown (red dashed line) is the cross-section of panel (b).

The determination of the antenna gap size is challenging using SEM. While the smallest gap sizes are comparable to the nominal resolution (< 2 nm, from manufacturer's data) of the field emission SEM used (Carl Zeiss® FESEM Ultra55), the interaction of the electron beam with the sample broadens the effective point spread function, widening the edge response. On the other hand, the relatively simple geometry of the optical antenna patterns enables determination of the system edge response. Once the edge response is

accounted for, the gap sizes can be determined accurately. The method is described below.

To ensure consistent characterization, the following procedure was taken for each fabricated dimer array to determine the gap size. First, SEM images were taken for nine randomly selected dimer structures in each dimer array. Magnification for each image was set to ~420 K×, with a typical image shown as Figure 2.4(a). The images are gray scale, with pixel values ranging from 0 (black) to 255 (white). Next, cross sections across the dimer gap were analyzed, as shown in Figure 2.4(b). In this figure, background subtraction has been performed. The background was found by determining the average grayscale value in the region surrounding the antenna from Figure 2.4(a) to be 72. The average grayscale value within the antenna structure was determined to be 128, and is shown in Figure 2.4(b) as a dashed line. The half-maximum value was therefore 64, and is also shown in Figure 2.4(b) as a dashed line.

It is now assumed that the edge response, including the effects of the finite size of the electron beam and its interaction with the sample, can be found from the image cross sections of the outer edges of the antenna. We assume that each image cross section can be considered to be the result of the convolution of the system point spread function with a pair of rectangle functions separated by a small gap, representing the actual antenna structure. The positions of the outer edges of the actual structure are therefore given by the half maximum positions in the image cross section (points A and B in Figure 2.4(b)). The image cross section around the gap can therefore be considered as the sum of two edge responses, offset from each other by the gap size. In Figure 2.4(c), we plot the image cross sections of the left and right outer edges as the green and blue curves,

respectively. The image cross sections have been translated so that points A and B are separated by 4 pixels. As shown in Figure 2.4(d), this results in the sum of the cross sections (black curve) having a modulation depth very close to that of the original image (dashed red curve, as shown as Figure 2.4(b)). Each pixel represents a distance of 0.68 nm. The retrieved gap size of 4 pixels is therefore equivalent to 3 nm.

2.1.3 Controlling gap size

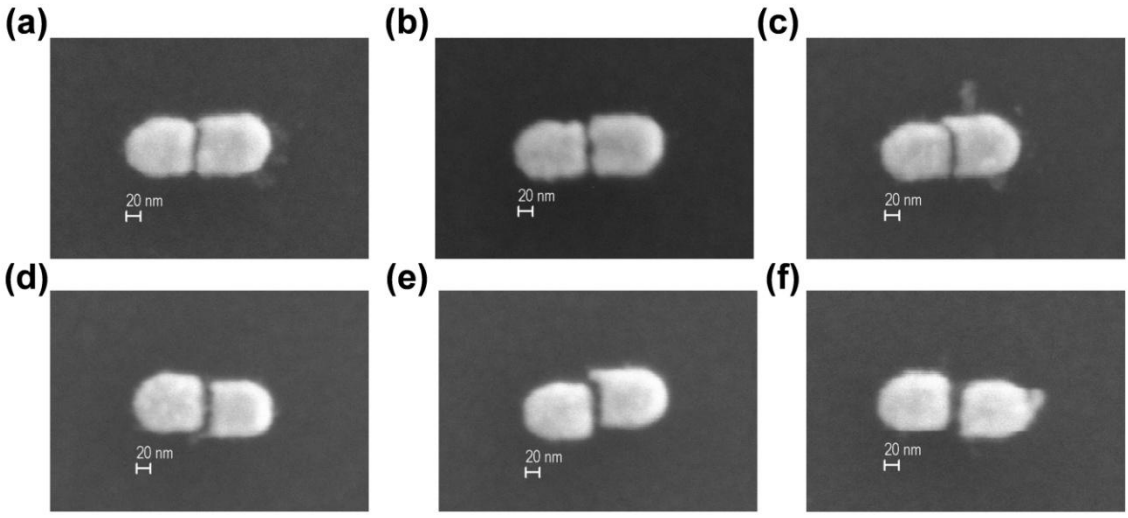

Figure 2.5 Effects of oxygen plasma time on gap size. SEMs of fabricated dimer structure by applying oxygen plasma for 0 min (a), 0.5 min (b), 1.0 min (c), 1.5 min (d), 2.0 min (e), and 3.0 min (f). SEMs obtained with 420K× magnification.

We demonstrate that the gap size can be controlled in an effective manner by varying fabrication parameters. As discussed, the gap size is determined by the lateral expansion of the chromium layer due to its oxidation. It has been suggested that the widths of nanoscale gaps intended for electrical measurements on molecules can be controlled by changing the thickness of the chromium deposited [23]. We tried this method, but found

a poor correlation between chromium thickness and gap size. We believe that this is due to the fact that this method relies on oxidation in ambient conditions, a process that is not well controlled. We therefore chose to use oxygen plasma to carry out the oxidation of Step (2) in Figure 2.1. Although this is not a standard oxidation method, it provides a convenient means for chromium oxidation and is demonstrated, as shown here, to enable reproducible control of the gap size. The plasma power and oxygen flow rate were fixed at 20 W and 50 sccm, respectively. The low plasma power ensures a slow oxidation rate of chromium; and the high oxygen flow rate ensures a relatively uniform oxidation. The duration of the plasma oxidation was used to control the gap sizes. Figure 2.5(a)-(f) show dimer structures fabricated with plasma times ranging from 0 min to 3 min. Four dimer arrays with sub-10-nm gaps were fabricated by applying plasma power for 1.5 min or less. The dimers of Figure 2.5(e) and (f) have gaps of 12 nm and 18 nm, respectively. Figure 2.6 shows the measured gap sizes produced with different plasma times. From the linear best fit to the data, the retrieved lateral oxidation rate is 5.0 nm/min, which is sufficiently slow to enable the fabrication of sub-10nm gaps in a controllable manner. The gap size

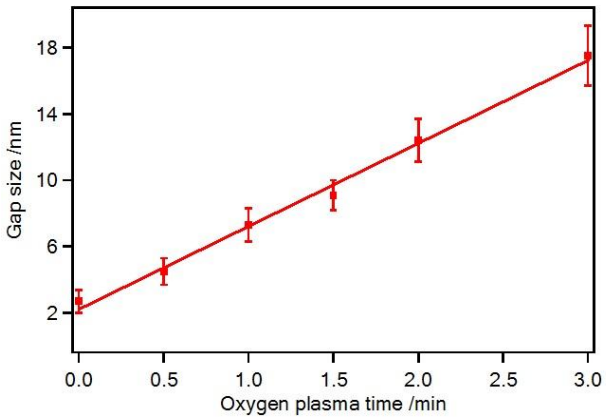

Figure 2.6. Gap size, determined from SEM, as a function of oxygen plasma time. Each error bar represents standard deviation of gap size for a particular dimer array, determined from nine randomly selected dimers within the array.

that results without the use of the oxygen plasma is ~2 nm. However, it should be noted that in addition to Step (3) of Figure 2.1, oxidation may occur in ambient conditions during other steps, such as resist baking for the second electron beam lithography.

2.2 Numerical simulations of the dimer antennas

Numerical electromagnetic simulations were performed by the finite-difference time-domain (FDTD) method. As shown in Figure 2.7, the dimensions of the simulated structures were identical to those of the designed dimers. The gap widths varied from 2 nm to 20 nm, to match the gap sizes achieved in fabrication. The dimers were made of gold and placed on top of a semi-infinite substrate. The substrate consisted of a 50 nm SiO_2 layer, a 20 nm ITO layer and a semi-infinite SiO_2 substrate. The refractive indices of the SiO_2 and the ITO layer were taken to be 1.45 and 1.65, respectively [7]. The gold permittivity was modeled by a multi-coefficient algorithm whose parameters were chosen to match the experimentally determined permittivity given by Ref. [26].

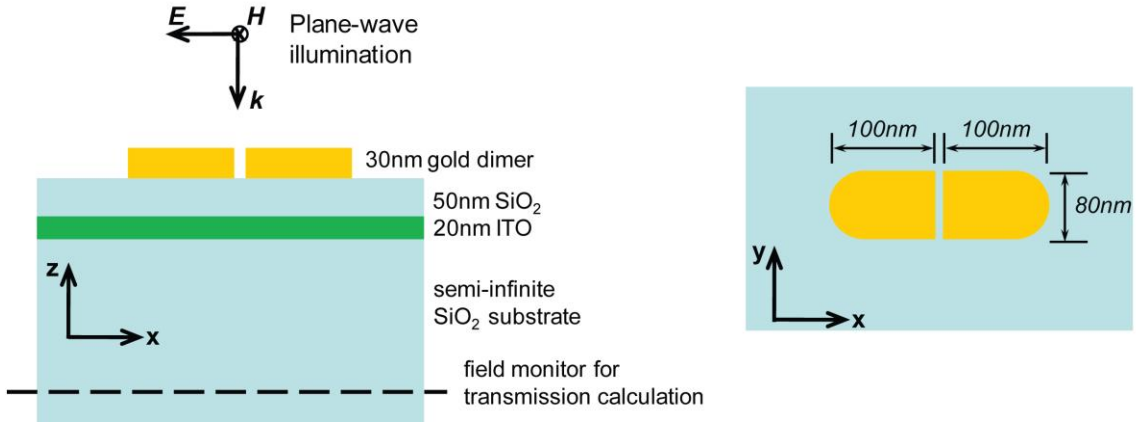

Figure 2.7 Schematic illustration of simulation geometry.

The periodic array was modeled using periodic boundary conditions (also exploiting symmetries) at the x-axis and y-axis boundaries, and perfectly-matched layers (PMLs) at the z-axis boundaries, with the orientation of the x-, y- and z- axes given in Figure 2.7. The total extent of the simulation space was 800 nm × 500 nm × 200 nm. The mesh size was set to be 0.5 nm × 0.5 nm × 0.5 nm within a region with dimensions 290 nm × 90 nm × 40 nm that enclosed the gold dimer pattern. A coarser mesh was used for the remainder of the computational volume. To confirm that the 0.5 nm mesh was sufficiently fine, simulations were also performed of a dimer with the narrowest gap (2 nm) with a mesh size of 0.25 nm. At an observation point in the gap center, the time- and frequency-domain results for the 0.25 nm and 0.5 nm meshes were seen to differ by less than 1%. This confirmed that the 0.5 nm mesh was sufficient, and this mesh size was therefore adopted in all the simulations in this Chapter.

A pulsed plane wave source, with a center wavelength of 800 nm and a bandwidth of 800 nm, was used to illuminates the dimer structure from the air side at normal incidence. The total simulation time was fixed at 100 fs, which was long enough for the electric fields to decay to less than 10^{-3} of the incident electric field.

The extinction cross-section of the dimer array was determined using a 2D steady-state field monitor. This monitor was placed 3 μm below the dimer plane, as shown in Figure 2.7. The extent of the monitor was 800 nm × 500 nm. The transmission of the dimer array, T_{Dimer}, was calculated as the integral of all the outgoing power through the monitor, normalized by the source power.[S9] In an analogous manner to the experimental measurements, the transmission through a bare substrate (i.e. without the gold dimer structure), T_o, was also calculated as the reference. The normalized transmission, T, is

then given by $T=T_{Dimer}/To$. The simulated extinction cross-section was again calculated by $C_{ext} = (1-T)\times A$, where A is the unit cell area.

Estimation of SERS electromagnetic enhancement factor (EM EF) was carried out by taking it as the product of the intensity enhancements at the laser and Stokes wavelengths, averaged over the dimer surface [27]. Simulations were performed to find the steady state field distributions at two wavelengths, whose separation was chosen to the model the 1074cm^{-1} Stokes shift; and whose arithmetic mean was equal to the dimer resonance wavelength. The incident field was a plane wave propagating toward the substrate (-z direction), with electric field polarized along the antenna axis (-x direction), and electric field magnitude 1 V/m. The magnitudes of the fields on a surface concentric to the gold surface S, with a 1 nm separation, were recorded. Note that the bottom surface, at the gold-glass interface, was not included as molecules cannot bind there. The spacing of 1 nm was chosen to represent the length of the benzenethiol molecule. The SERS EM EF was then estimated as:

$$EF = \frac{\iint_S \left|E_{total}(\nu_{Laser})\right|^2 \left|E_{total}(\nu_{Stokes})\right|^2 ds}{\iint_S ds} \qquad (2.1)$$

2.3 Extinction cross-section

The optical properties of the fabricated dimer array were investigated by evaluating white light transmission spectra measured with polarized illumination. As shown in Figure 2.8, a 10× objective lens (NA = 0.25) was used to focus the incident polarized light onto the dimer array. The transmitted light was collected by another 50× objective lens (NA = 0.55) into a spectrometer equipped with a thermoelectrically-cooled CCD array. An iris

was used at the image plane of the objective to ensure that only the light transmitted through the array was detected. Reference spectra were obtained by measuring the signal transmitted through a region of the sample away from the dimer array, that is, consisting of only the ITO-coated glass substrate with a layer of 50 nm SiO_2. These spectra were recorded under the same conditions as the spectra of the dimer arrays. The transmittance through each dimer array, T, was then found by dividing the dimer array spectrum by the reference spectrum. The extinction cross-section, C_{ext}, was then found using $C_{ext} = (1-T) \times A$, where A is the area of the unit cell.

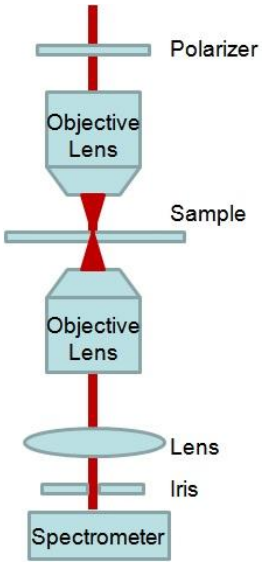

Figure 2.8. Experimental setup for measurement of extinction spectra of dimer arrays.

Figure 2.9(a) shows the extinction spectra of six typical samples retrieved from transmission spectra. Reducing the gap size red-shifts the resonance, which is consistent with theoretical predictions [28]. This is further FDTD simulation results shown in Figure 2.9(b). Resonance peaks from simulation slightly differ from those from measurement; but the trend is consistent. It may be due to the fact that the simulations take the dielectric constant of gold to be that of bulk gold, but this may not be the case, since it varies with grain structure [29]. Simulated resonance linewidths (full-width half-maximum of extinction spectrum) are ~50 - 70% smaller than measurements. This could be due to the

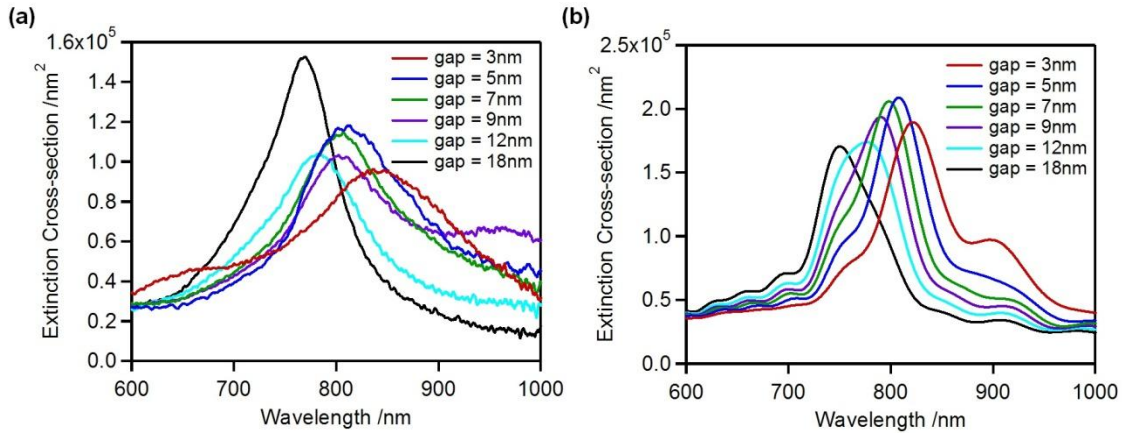

Figure 2.9. Extinction cross-sections for dimer arrays with different gap sizes. (a) Measured from measurement. (b) Retrieved from FDTD simulation.

non-uniformity of gap sizes within each array. It is also observed that the peak extinction cross-sections from measurement vary for different samples; this may be due to differences in fabrication yield between samples. For example, the yield of the 3nm-gap sample is estimated to be ~81%; while that of the 18 nm-gap structures is almost unity.

2.4 SERS measurements

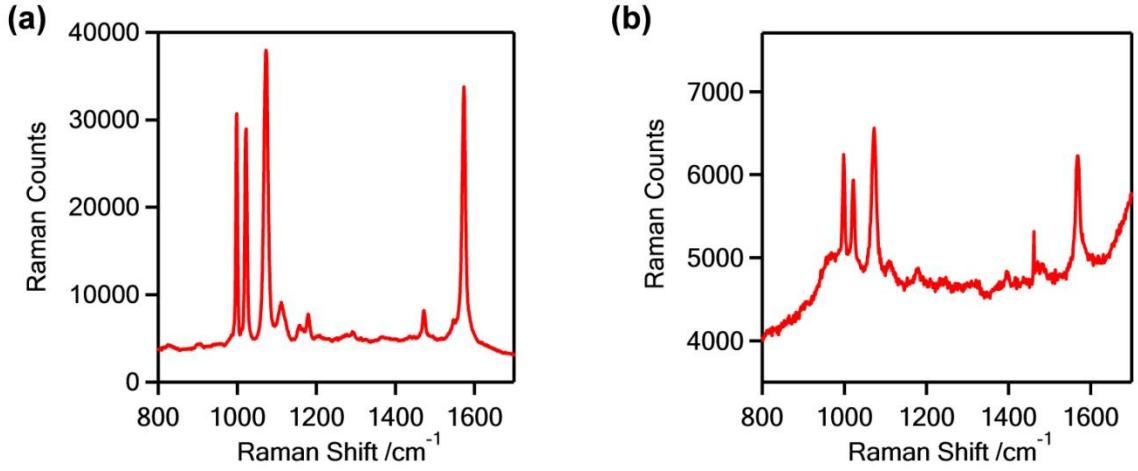

Figure 2.10. SERS measurement for dimer arrays with (a) 3 nm gaps and (b) 12 nm gaps.

One of the major applications of optical antennas is for SERS. As discussed, it is generally accepted that higher enhancement can be achieved with smaller gaps [13]. However, few systematic studies on the variation in enhancement factor with gap size in the sub-10 nm range have been performed, owing to the difficulties associated with fabrication in this size regime. On the other hand, the fabrication method we introduce here enables such a study. We begin by comparing the SERS signals from samples with 3 nm and 12 nm gaps, as shown in Figure 2.10(a) and (b). Self-assembled monolayers of thiophenol were formed on both samples (see Chapter 1). The excitation wavelength for each sample was selected such that the mean value of laser wavelength and Stokes wavelength matched the peak resonance of the dimer array, to ensure the largest enhancement factor [30]. Even with the smaller laser power, the Raman counts from the 3 nm gap sample were much larger than those from the 12 nm gap sample. Indeed, the measured SERS EF for the 1074cm^{-1} Raman line is 1.1x10^{8} for the 3 nm-gap sample; and 4.4x10^{6} for the 12 nm gap sample, representing a ~25 fold improvement with the reduced gap size. Figure 2.11(a) and (b) show the mappings of retrieved EFs over 75 μm × 75 μm

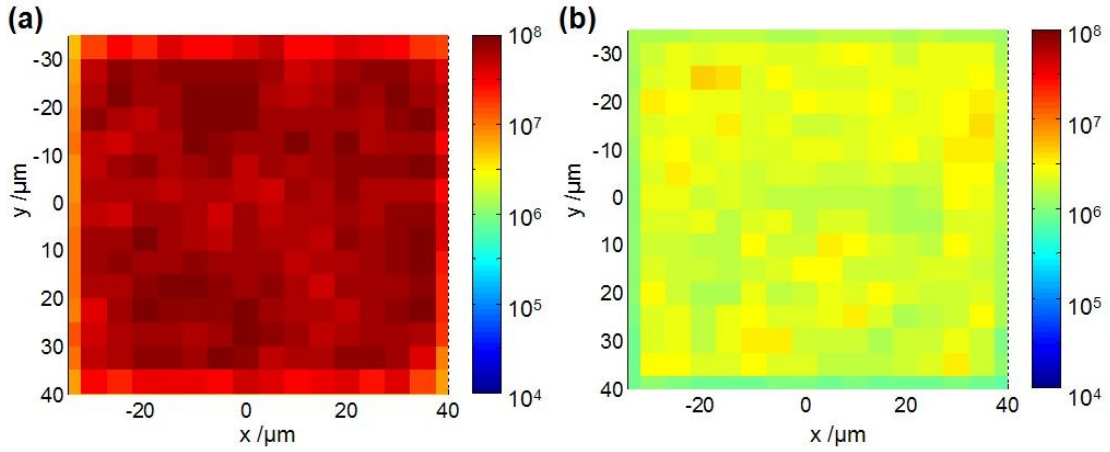

Figure 2.11. Mapping of retrieved enhancement factors over 75 μm × 75 μm dimer array with gap sizes of (a) ~ 3 nm and (b) ~ 12 nm.

dimer arrays with gap sizes of ~ 3 nm and ~ 12 nm, respectively. To understand the mechanism of this enhancement better, the steady-state field distributions calculated by FDTD are shown in Figure 2.12(a) and (b), using the method described in Section 2.2. The highest field intensity (square of electric field, $|E|^2$) enhancement in the 3 nm gap is ~6 times larger than that in the 12 nm gap. A rough estimation of SERS EF is often based on $|E|^4$ approximation [13,27], which indicates that the enhancement of the 3 nm gap antenna is ~36 fold higher than the 12 nm gap antenna. This is generally consistent with the improvement from the SERS measurement, while a more rigorous estimation of electromagnetic SERS EF (see Chapter 1) is used later.

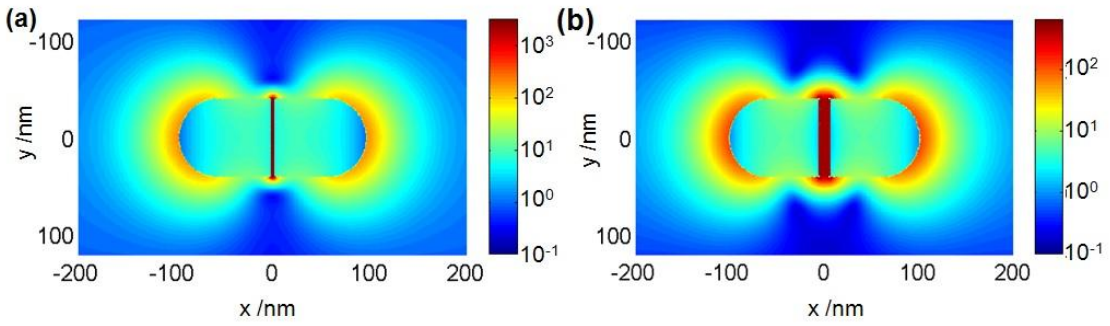

Figure 2.12. Steady-state field intensity distribution ($|E|^2$) calculated by FDTD method. Plane wave illumination was polarized along the antenna axes. Field intensity distribution is shown over center plane of dimer, 15 nm away from substrate. (a) For dimer structure 3 nm gaps at a wavelength of 821 nm. (b) For dimer structure 3 nm gaps at a wavelength of 776 nm.

Identical measurements can be performed for dimer structures with other gap sizes. SERS EFs, as a function of dimer gap size, are mapped out in Figure 2.13. The laser excitation wavelengths were again selected for each dimer array to ensure maximum enhancement factor. Raman signal integration time for all the measurements were 5s. In

Figure 2.13, samples with the same gap size exhibit different enhancement factors. This is likely to be due to differences in structural morphology between samples with the same gap size. FDTD simulations were also performed for structures with various gap sizes to determine the expected EM EF. As shown in Figure 2.13, the simulated EM EFs were ~75 times smaller than from the measured SERS EFs. Because the SERS measurements include the effects of chemical and electromagnetic enhancement [10,31], we estimate that most of this discrepancy is due to chemical enhancement. Although detailed explanation requires close examination of individual dimer structure and is beyond the scope here, it is on the same order as that noted by Talley *et al*. [32], although Lombardi and Birke find that in other cases it can be much higher [33].

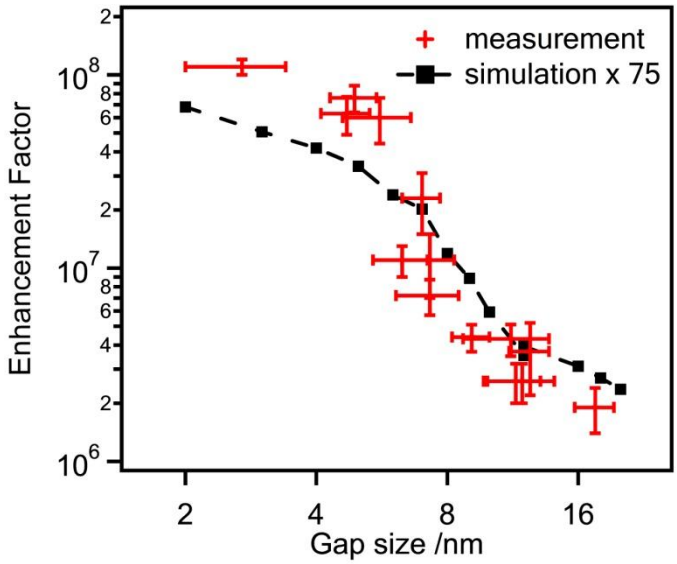

Figure 2.13. Measured SERS EF and simulated EM EF as a function of gap size. Each experimental data point was obtained from measurements made on a different sample. EF error bars represent the standard deviation in measured EF for each sample, determined from measurements made at nine points on the sample. Gap size error bars represents standard deviation of gap size for a particular dimer array, determined from nine randomly selected dimers within the array. EM EF was calculated by the FDTD method, and was multiplied by 75× to enable comparison to experimental data.

The SERS measurements reveal the effect of substantially enhanced electromagnetic field generated in dimer gaps [34]. From Figure 2.13, for gap size larger than 10 nm, the EFs are ~10^6. This case means that the EF is not significantly improved over that obtained from isolated patterns [14], representing weak enhancement within the gap between the two gold nanoparticles [12]. When the gap size is reduced to ~10 nm or less, EF approaches ~10^7. This is the strong enhancement case: due to the small distance between the particles, localized surface plasmon resonance of each particle is further amplified by the other, thereby significantly enhancing the field in the gap. When the gap size is further decreased to 5 nm or below, or even 3 nm as demonstrated here, EF can exceed 10^8, approaching the requirement for single molecule detection [35]. It should be pointed out that typical SERS single-molecule SERS active dimer structure consist of two silver nanocrystals, which would provide stronger surface plasmon resonance than the amorphous gold patterns employed here. Therefore the enhancement for these dimers is expected to be larger than that of the structures fabricated here. However, our lithographically fabricated dimer structure can be integrated with other plasmonic structures to achieve even higher enhancement factor [36,37], and therefore represents progress toward the goal of reproducible single molecule SERS substrates.

2.5 Conclusions

In conclusion, we have developed a fabrication procedure based on a sacrificial layer for the lithographic fabrication of optical antennas with gaps well below 10 nm. We

demonstrate that the gap size can be effectively controlled by oxidizing the sacrificial layer using oxygen plasma. Localized electromagnetic fields can be significantly enhanced within the nanoscale gaps, as indicated by SERS measurements. This work enhances the ability to fabricate reproducible SERS substrates using a top-down method with high enhancement factor. Moreover, by offering an accessible approach to fabricate features well below 10 nm, we anticipate that this technique will enable the fabrication of novel plasmonic structures otherwise not possible with standard techniques.

References

[1] J. Wessel, "Surface-enhanced optical microscopy," J. Opt. Soc. Am. B **2**, 1538 (1985).

[2] R. D. Grober, R. J. Schoelkopf, and D. E. Prober, "Optical antenna: Towards a unity efficiency near-field optical probe," Appl. Phys. Lett. **70**, 1354 (1997).

[3] K. B. Crozier, A. Sundaramurthy, G. S. Kino, and C. F. Quate, "Optical antennas: Resonators for local field enhancement," J. Appl. Phys. **94**, 4632–4642 (2003).

[4] L. Novotny, "Effective Wavelength Scaling for Optical Antennas," Phys. Rev. Lett. **98**, 266802 (2007).

[5] P. Mühlschlegel, H.-J. Eisler, O. J. F. Martin, B. Hecht, and D. W. Pohl, "Resonant optical antennas," Science **308**, 1607–1609 (2005).

[6] H. Ko, S. Singamaneni, and V. V Tsukruk, "Nanostructured surfaces and assemblies as SERS media.," Small **4**, 1576–1599 (2008).

[7] M. G. Banaee and K. B. Crozier, "Mixed Dimer Double-Resonance," ACS Nano **5**, 307–314 (2011).

[8] K. Kneipp, Y. Wang, H. Kneipp, L. T. Perelman, I. Itzkan, R. R. Dasari, and M. S. Feld, "Single Molecule Detection Using Surface-Enhanced Raman Scattering (SERS)," Phys. Rev. Lett. **78**, 1667–1670 (1997).

[9] S. Nie and S. R. Emory, "Probing Single Molecules and Single Nanoparticles by Surface-Enhanced Raman Scattering," Science **275**, 1102–1106 (1997).

[10] A. M. Michaels and L. Brus, "Ag Nanocrystal Junctions as the Site for Surface-Enhanced Raman Scattering of Single Rhodamine 6G Molecules," J. Phys. Chem. B **104**, 11965–11971 (2000).

[11] H. Xu, E. Bjerneld, M. Käll, and L. Börjesson, "Spectroscopy of Single Hemoglobin Molecules by Surface Enhanced Raman Scattering," Phys. Rev. Lett. **83**, 4357–4360 (1999).

[12] J. Aizpurua, G. W. Bryant, L. J. Richter, and F. J. García de Abajo, "Optical properties of coupled metallic nanorods for field-enhanced spectroscopy," Phys. Rev. B **71**, 1–13 (2005).

[13] H. Xu, J. Aizpurua, M. Kall, and P. Apell, "Electromagnetic contributions to single-molecule sensitivity in surface-enhanced raman scattering," Phys. Rev. E **62**, 4318–4324 (2000).

[14] N. Félidj, J. Aubard, G. Lévi, J. Krenn, M. Salerno, G. Schider, B. Lamprecht, a. Leitner, and F. Aussenegg, "Controlling the optical response of regular arrays of gold particles for surface-enhanced Raman scattering," Phys. Rev. B **65**, 1–9 (2002).

[15] A. W. Clark and J. M. Cooper, "Optical properties of multiple-split nanophotonic ring antennae.," Adv. Mater. **22**, 4025–4029 (2010).

[16] M. D. Fischbein and M. Drndić, "Nanogaps by direct lithography for high-resolution imaging and electronic characterization of nanostructures," Appl. Phys. Lett. **88**, 063116 (2006).

[17] H. Wang, C. S. Levin, and N. J. Halas, "Nanosphere arrays with controlled sub-10-nm gaps as surface-enhanced raman spectroscopy substrates.," J. Am. Chem. Soc. **127**, 14992–3 (2005).

[18] D.-K. Lim, K.-S. Jeon, H. M. Kim, J.-M. Nam, and Y. D. Suh, "Nanogap-engineerable Raman-active nanodumbbells for single-molecule detection.," Nat. Mater. **9**, 60–67 (2010).

[19] J.-H. Tian, B. Liu, X. Li, Z.-L. Yang, B. Ren, S.-T. Wu, N. Tao, and Z.-Q. Tian, "Study of molecular junctions with a combined surface-enhanced Raman and mechanically controllable break junction method.," J. Am. Chem. Soc. **128**, 14748–14749 (2006).

[20] D. R. Ward, N. K. Grady, C. S. Levin, N. J. Halas, Y. Wu, P. Nordlander, and D. Natelson, "Electromigrated nanoscale gaps for surface-enhanced Raman spectroscopy.," Nano Lett. **7**, 1396–1400 (2007).

[21] M. J. Banholzer, J. E. Millstone, L. Qin, and C. a Mirkin, "Rationally designed nanostructures for surface-enhanced Raman spectroscopy.," Chem. Soc. Rev. **37**, 885–897 (2008).

[22] J. Tang, Y. Wang, C. Nuckolls, and S. J. Wind, "Chemically responsive molecular transistors fabricated by self-aligned lithography and chemical self-assembly," J. Vac. Sci. Technol. B Microelectron. Nanom. Struct. **24**, 3227 (2006).

[23] a. Fursina, S. Lee, R. G. S. Sofin, I. V. Shvets, and D. Natelson, "Nanogaps with very large aspect ratios for electrical measurements," Appl. Phys. Lett. **92**, 113102 (2008).

[24] H. Im, K. C. Bantz, N. C. Lindquist, C. L. Haynes, and S.-H. Oh, "Vertically oriented sub-10-nm plasmonic nanogap arrays.," Nano Lett. **10**, 2231–6 (2010).

[25] S. Lee, J. Shin, Y.-H. Lee, S. Fan, and J.-K. Park, "Directional photofluidization lithography for nanoarchitectures with controlled shapes and sizes.," Nano Lett. **10**, 296–304 (2010).

[26] P. B. Johnson and R. W. Christy, "Optical constants of the noble metals.," Phys. Rev. B **6**, 4370–4379 (1972).

[27] E. C. Le Ru and P. G. Etchegoin, "Rigorous justification of the |E|4 enhancement factor in Surface Enhanced Raman Spectroscopy," Chem. Phys. Lett. **423**, 63–66 (2006).

[28] P. Nordlander, C. Oubre, E. Prodan, K. Li, and M. I. Stockman, "Plasmon hybridization in nanoparticle dimers," Nano Lett. **4**, 899–903 (2004).

[29] K.-P. Chen, V. P. Drachev, J. D. Borneman, A. V Kildishev, and V. M. Shalaev, "Drude relaxation rate in grained gold nanoantennas.," Nano Lett. **10**, 916–922 (2010).

[30] A. D. McFarland, M. A. Young, J. A. Dieringer, and R. P. Van Duyne, "Wavelength-scanned surface-enhanced Raman excitation spectroscopy," J. Phys. Chem. B **109**, 11279–11285 (2005).

[31] S. K. Saikin, R. Olivares-Amaya, D. Rappoport, M. Stopa, and A. Aspuru-Guzik, "On the chemical bonding effects in the Raman response: benzenethiol adsorbed on silver clusters.," Phys. Chem. Chem. Phys. **11**, 9401–9411 (2009).

[32] C. E. Talley, J. B. Jackson, C. Oubre, N. K. Grady, C. W. Hollars, S. M. Lane, T. R. Huser, P. Nordlander, and N. J. Halas, "Surface-enhanced Raman scattering from individual Au nanoparticles and nanoparticle dimer substrates.," Nano Lett. **5**, 1569–1574 (2005).

[33] J. R. Lombardi and R. L. Birke, "A Unified Approach to Surface-Enhanced Raman Spectroscopy," J. Phys. Chem. C **112**, 5605–5617 (2008).

[34] S. Lal, N. K. Grady, G. P. Goodrich, and N. J. Halas, "Profiling the near field of a plasmonic nanoparticle with Raman-based molecular rulers.," Nano Lett. **6**, 2338–2343 (2006).

[35] E. C. LeRu, M. Meyer, and P. G. Etchegoin, "Surface Enhanced Raman Scattering Enhancement Factors: A Comprehensive Study," J. Phys. Chem. C **111**, 13794–13803 (2007).

[36] Y. Chu, M. G. Banaee, and K. B. Crozier, "Double-Resonance Plasmon Substrates for Surface-Enhanced Raman Scattering Stokes Frequencies," ACS Nano **4**, 2804–2810 (2010).

[37] D. Wang, T. Yang, and K. B. Crozier, "Optical antennas integrated with concentric ring gratings: electric field enhancement and directional radiation.," Opt. Express **19**, 2148–2157 (2011).

Chapter 3 Raman emission pattern from dimer antennas and energy momentum spectroscopy

Optical antennas employ the localized surface plasmon resonances (LSPRs) of metal nanoparticles to enhance light–matter interactions [1]. Engineered optical antennas boost the efficiency by which light can be focused into subwavelength regions. Similarly, in the reciprocal process, optical antennas boost the transmission of energy to the far-field. Recently, interest has emerged on shaping the emission patterns of nanoscale emitters with directional optical antenna designs [2–6]. A common goal of these efforts is to collimate emission into one direction, thereby enabling efficient detection even with low numerical aperture (NA) objective lenses. It is well established that emission patterns from nanoscale emitters can be directly imaged in the back focal planes of high-NA objective lenses [7]. This technique has very high sensitivity, even at the single molecule level. Using the back focal plane technique, directional antennas, such as Yagi–Uda designs and periodic plasmonic structures, have been shown to efficiently collimate the emission from quantum dots and fluorescent molecules [3,5].

Since the first demonstrations of single molecule sensitivity [8,9], much emphasis in SERS substrate design has been on finding nanostructures with larger electric field enhancement. Recently, the importance of directionality in SERS has been recognized. That Raman scattering can be collimated by directional optical antennas has been termed

"beamed Raman scattering" [10,11] and directional SERS (DERS) [12]. These concepts have been employed in SERS substrates achieving very high EFs (average value ~10^{10}) [13] and for single molecule sensitivity [14]. One of the challenges facing the direct observation of beamed Raman scattering is that Raman cross sections are weak, typically orders of magnitude smaller than fluorescence cross sections. Shegai et al. addressed the problem of measuring the angular distribution of SERS from Rhodamine 6G molecules adsorbed on individual gold nanoparticle aggregates [4]. A microscope objective was used to focus laser light onto each aggregate and to collect the emission, with Rayleigh scattered laser light removed with a long pass filter (LFP). The angular distribution of emitted light could be directly monitored in the Fourier plane of the optical microscope. There was no provision, however, to distinguish between the emission patterns of the Raman lines and that of the broad background continuum. The latter comes from fluorescent emission of the Raman molecules or the substrate or even photoluminescence of the metallic structure itself [15,16].

An improved version of the "back focal plane" technique, namely energy momentum spectroscopy (hereon referred as the "EMS technique"), has recently been developed to measure both the spectral and angular characteristics of the emission patterns of nanoscale emitters [17]. A spectrometer measures the spectrum of each pixel in the back focal plane of the objective lens, enabling the emission pattern for each wavelength of interest to be determined. In this chapter, we use the EMS technique to measure the radiation patterns of multiple Raman lines of dimer antenna on top of dielectric substrates. In the following chapters, we study more complex optical antenna designs, and directly and unambiguously observe the "beamed Raman scattering" effect.

3.1 Simulation of Raman emission pattern

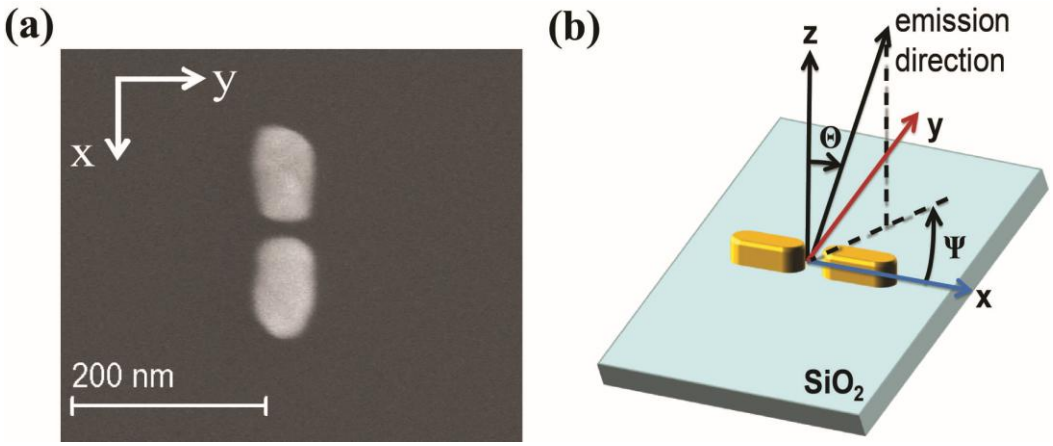

Figure 3.1. Dimer antenna on dielectric substrate. (a) SEM image of one dimer antenna under study. (b) Definition of the Cartesian coordinates and spherical coordinates to describe the Raman emission pattern.

The dimer antennas are fabricated by electron-beam lithography on a glass cover-slip coated with indium tin oxide (ITO). The SEM image of one dimer antenna under study is shown in Fig. 3.1(a). It consists of two gold nanorods that are both 117 nm long and 65 nm wide. They are separated by a gap of 13 nm. Large near-field enhancement within the small gap region ensures a large SERS enhancement factor. To increase the signal-to-background ratio, measurements are made from arrays of optical dimer antennas rather than from a single dimer antenna. The unit cell of the array (0.5 μm × 1.5 μm) is chosen to be large in order to minimize near-field coupling between adjacent dimer antennas. To further reduce background fluorescence, a non-resonant Raman molecule (thiophenol) is used, formed on the dimer antennas as a self-assembled monolayer (SAM). In the following simulations/experiments, the laser excitation wavelength is maintained at λ = 785 nm, meaning that the 1074 cm^{-1} Raman line occurs at λ = 857 nm. The dimensions of the dimers are designed such that its peak LSPR

resonance matches this wavelength. We also perform experiments and simulations for the Raman lines 415 cm^{-1} (λ = 811 nm) and 1586 cm^{-1} (λ = 896 nm), as a way of determining the dispersion of emission patterns.

The model to study the Raman emission pattern is depicted in Figure 3.1(b), which shows a dimer antenna placed on top of a glass substrate. The simulations are performed for single, isolated antennas, rather than for the entire array. Indeed, we found no differences between applying periodic boundary conditions (PBC) and perfect-matched-layer (PML) conditions in simulating the LSPRs peaks of the antennas. Although in experiments, the thiophenol molecules coat the antenna surface uniformly, the largest Raman dipole is induced within the gap region, due to the greatly enhanced near-fields there. For the simulations, therefore, we place an electric Raman dipole in the center of the gap region with a random orientation. It should be noted that we also performed simulations for x-, y- and z-oriented dipoles, but found no differences in the emission patterns. The antenna orientation and emission angles (Θ, Ψ) are schematically illustrated as Fig. 3.1(b). We simulate the emission patterns into all spherical angles. The upper hemisphere is air and the lower hemisphere is a glass substrate with n = 1.5. The simulation is performed based on finite-element method (FEM) using the RF Module of the COMSOL® Multiphysics package. The simulation domain is defined in spherical coordinates, with a spherical PML at the outermost layer of the computational region. The emission pattern is then found using COMSOL's far-field calculation method, which is based on the Stratton-Chu formula.

Fig. 3.2 shows the simulated Raman radiation pattern at λ = 857 nm. In the emission process, the Raman dipole excites the dipolar LSPR mode of the dimer antenna

[15]. If the Raman dipole frequency coincides with LSPR frequency, as is the case here, the emission pattern of Raman scattering will be dominated by the dipolar mode of the dimer antenna [6]. Therefore, although the orientation of the Raman dipole is arbitrary, Figure 3.2 can be seen to follow the typical emission pattern for a horizontal dipole radiating above dielectric substrate. It can be seen that the majority of the radiated power goes into the substrate; is mainly within the yz-plane that is perpendicular to the dipole orientation; and occurs symmetrically into two lobes which are just beyond the critical angle for total internal reflection at the air-dielectric interface.

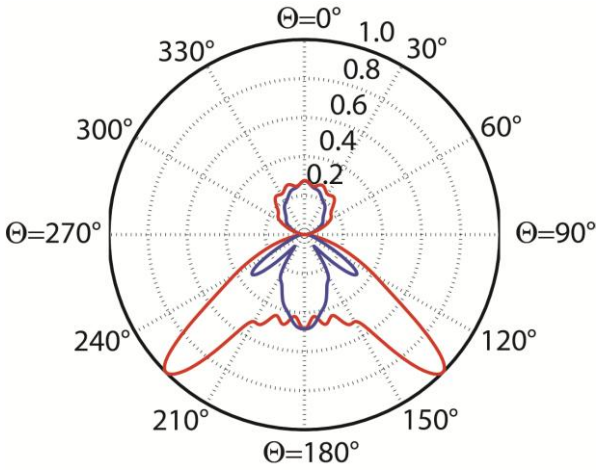

Figure 3.2. FEM simulation of the emission pattern, in which an arbitrarily oriented Raman dipole is placed at the gap center of the dimer antenna. The region below the line from Θ = 90° to Θ = 270° represents the dielectric substrate. Red: emission pattern in yz-plane (Ψ = 90 °); blue: emission pattern in xz-plane (Ψ = 0 °).

3.2 Energy momentum spectroscopy (EMS)

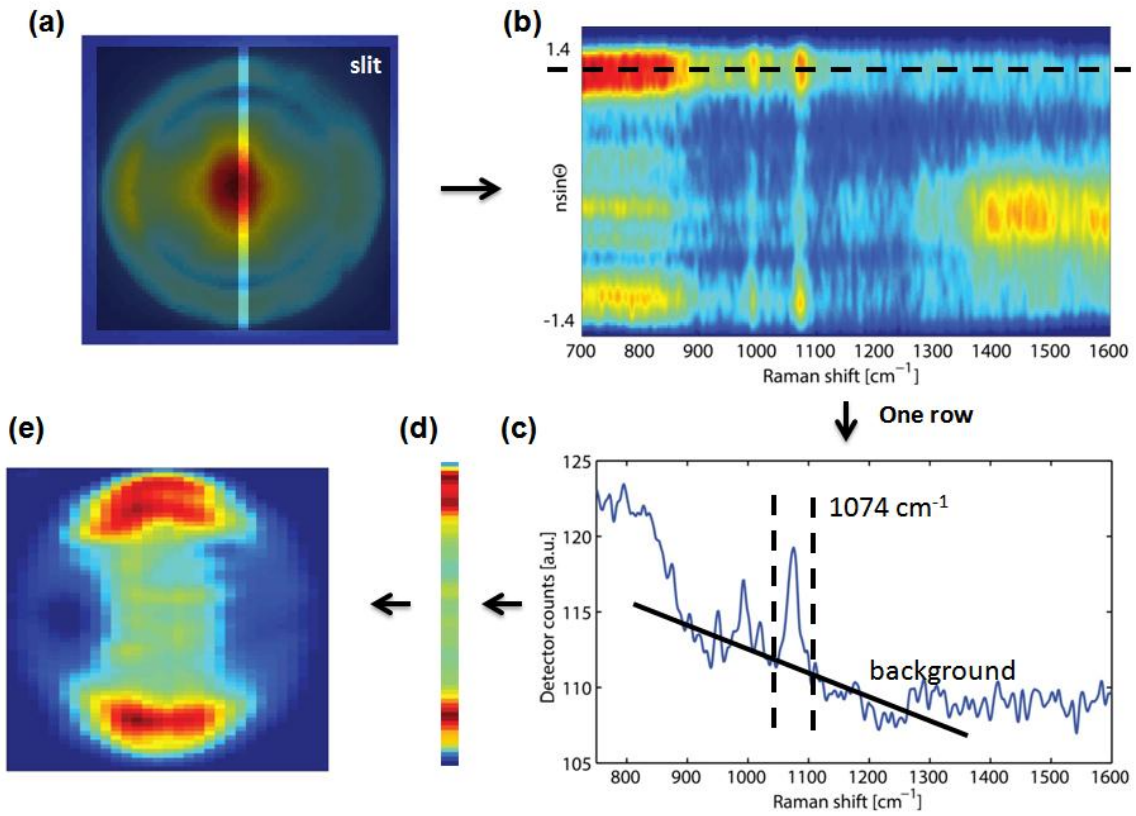

Figure 3.3. Measuring the Raman emission patterns by energy-momentum spectroscopy. (a) Typical emission pattern from the back focal plane of the objective lens. A vertical column is selected by a narrow slit, shown as the grey region. (b) Spectrograph of the vertical column, as recorded by spectrometer CCD. (c) Raman spectrum of one row of the spectrograph in (b). (d) Reconstructed column of Raman emission pattern. (f) Reconstructed Raman emission pattern by scanning the slit horizontally.

In the "back focal plane" technique, the light intensity distribution at the back focal plane of a microscope objective lens is used to find the radiation patterns from nanoemitters such as fluorescent molecules [7]. Along similar lines, we employ the EMS technique to observe the Raman emission pattern. As shown in Figures 2.10, SERS spectra typically consist of distinct Raman peaks on top of a broad background continuum. A band-pass filter (BPF) can be used to select a narrow frequency range of a SERS spectrum.

Nonetheless, the use of BPF with direct CCD imaging does not provide a means for extracting the emission pattern of a Raman line from the luminescent background [15,16].

EMS allows separation of Raman signal from the background. This method is described in Figure 3.3. The sample used here consists of dimer antennas placed on glass substrate. Figure 3.3(a) is a typical emission pattern measured from the back focal plane of the objective lens. We then use a narrow slit to select one vertical column of this emission pattern. This is depicted in Figure 3.3(a), in which the slit is denoted by gray shading. The entrance slit of spectrometer is wide open. We do not stop it down as there is no provision for moving it horizontally, which would be needed in order to sample the back focal plane image.

We then use another lens to create an image this back focal plane column at the entrance slit of the spectrometer. Figure 3.3(b) shows a typical spectrograph measured on the spectrometer CCD camera. The image represents a two-dimensional (2D) spectral map, with the x-axis being the wavelength and the y-axis being the vertical position. Each row of this spectrograph represents the spectrum of each row in the selected vertical column. The sharp and bright red lines represent the Raman peaks. The lateral dispersion shown in the figure is mainly due to the toroidal mirrors of the spectrometer (Princeton Instruments®, SP.2300i). It can be reduced with a lower resolution grating or using a region of the CCD with a smaller lateral extent. The vertical asymmetry is due to the slight rotational misalignment of the CCD camera equipped with the spectrometer and can be easily fixed in data analysis. One row of pixels of the image of Figure 3.3(b) is plotted as Figure 3.3(c), and shows a typical Raman spectrum with Raman peaks and a luminescent background. The background (black line in Figure 3.2d) is a linear fit of

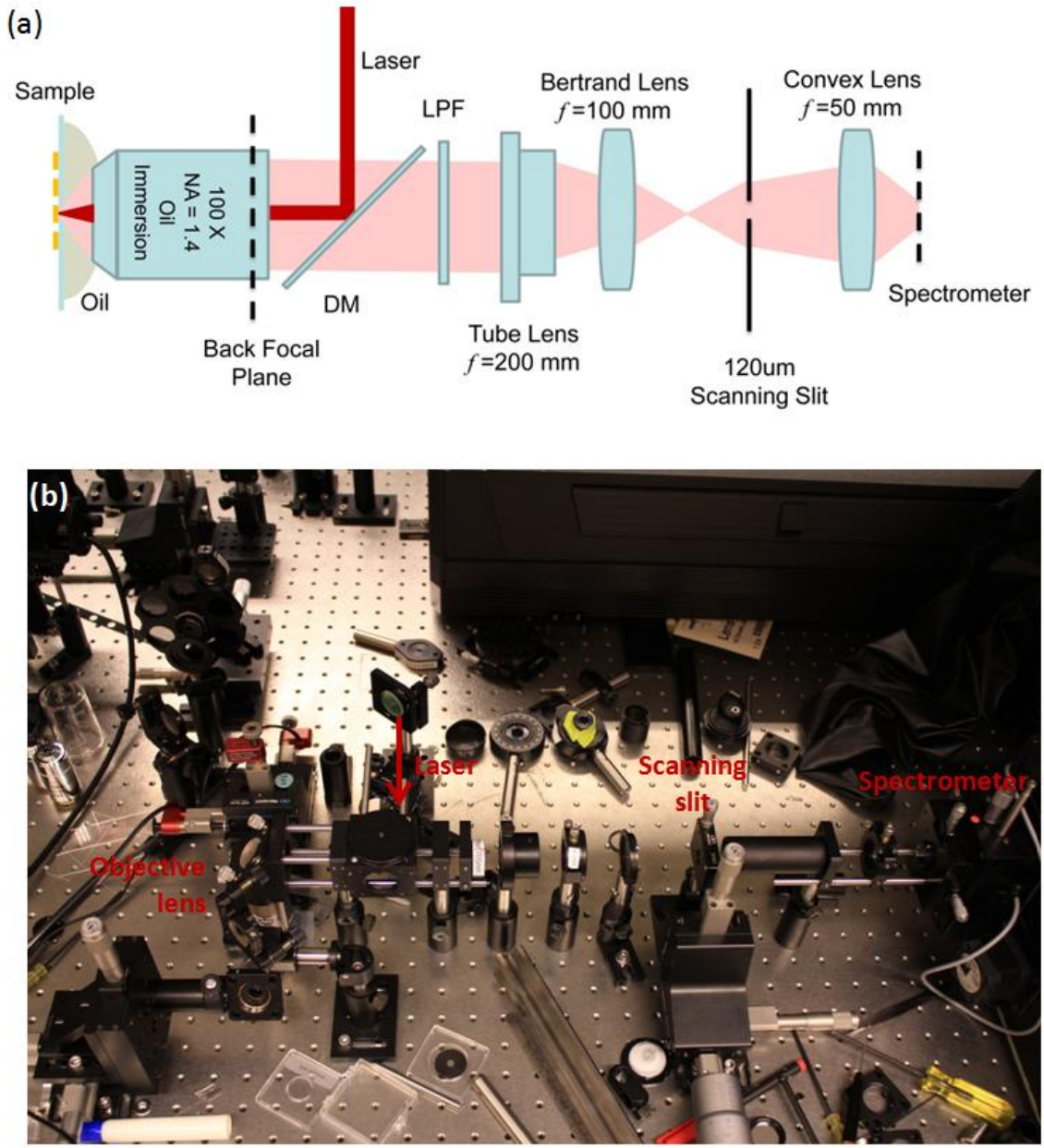

Figure 3.4. Experimental setup for energy momentum spectroscopy (EMS). The far-field emission pattern from the sample is found by imaging the back focal plane of the objective lens. LPF: long-pass filter. DM: dichroic mirror. (a) Schematic diagram. (b) Photograph of optical setup.

detector counts in the region of 840 nm to 850 nm and 860 nm to 870 nm, which are just away from the three Raman peaks around 857 nm. From this, the counts of the Raman line of interest (e.g. 1074 cm^{-1}) can be found. This procedure is repeated for each pixel

within the vertical column (Figure 3.3(d)). It is also repeated for each column of the back focal plane image by scanning the slit horizontally. This yields the emission pattern for the Raman line of interest (e.g. 1074 cm^{-1}), as shown in Figure 3.3(e). The fact that the circular outline of the reconstructed image has a radius corresponding to the NA of the lens enables the image to be calibrated.

The experimental setup of EMS measurements is shown in Figure 3.4. A polarized continuous wave (CW) laser with a wavelength of 785 nm and a power of 9.3 mW is focused by an objective lens onto the sample. For the measurements in this chapter, the objective lens is oil-immersion (Nikon 100×, NA = 1.40, infinity corrected, immersion oil n = 1.5). The Raman scattering from the thiophenol molecules is collected by the same objective lens. A long pass filter (λ = 785 nm) is placed in the optical path to block the Rayleigh scattered laser light. A convex lens with focal length of 100 mm acts as a Bertrand lens to create a first image plane of the objective lens back focal plane. A slit (120 μm wide), mounted on a translation stage to move it transverse to the optical path, is placed at this image plane of back focal plane. Another convex lens with a focal length of 50 mm creates a second image plane of back focal plane at the spectrometer entrance slit, with a demagnification factor of 3.2 times from the first image plane. This results in the back focal plane image matching the size of the CCD in the spectrometer. The alignments of the Bertrand lens and reimaging lens are checked by moving each along the optical axis, and verifying that the images observed by the CCD camera expand or shrink symmetrically about the lens position. The scanning slit enables us to select a column from the back focal plane image. Each pixel in the column is dispersed horizontally by the spectrometer grating. In this way, each row in the spectrometer CCD

represents the spectrum of each pixel of the column of the back focal plane image. Scanning the slit enables different columns from the back focal plane image to be selected. The step size of the translation stage is 20 μm and typically 46 measurements are recorded to reconstruct the final emission pattern. Since the radius of the emission pattern corresponds to NA of the objective lens, each pixel of the momentum space image has a horizontal width corresponding to a momentum of (2/46)NA=0.045NA. In the vertical direction, each pixel of the momentum space image corresponds to a momentum of 0.030NA, which is determined by the vertical pixel numbers of the CCD camera. Data binning of groups of 2×2 raw pixels is performed to increase signal-to-noise ratio. For the measurements made on those antennas, each pixel of the momentum space image corresponds to 0.09NA × 0.06NA.

3.3 Observing Raman emission pattern from dimer antennas

As discussed, simulations (Figure 3.2) predict that Raman scattering from molecules on a dimer antenna primarily occurs into the substrate and with a characteristic pattern. We thus focus on measuring the Raman emission pattern into the substrate. The measured SERS emission pattern at λ = 857 nm (1074 cm^{-1} Raman line) found using the EMS technique is shown as Figure 3.5. As depicted in Figure 3.1(b), the dimer antennas are oriented such that their longer axes are parallel to the laser polarization ($\Psi = 0°$, x-axis). Figure 3.5 can be understood as being in a polar coordinate system, with the origin at the center of the circular pattern [7]. The radial coordinate r corresponds to the polar angle Θ of Raman emission according to $r = |n\sin\Theta|$, where n = 1.5 for the glass cover-slip. The

outline of the circle represents the numerical aperture of the objective lens (NA = 1.4). The angular coordinate corresponds to the azimuth angle Ψ of Raman emission.

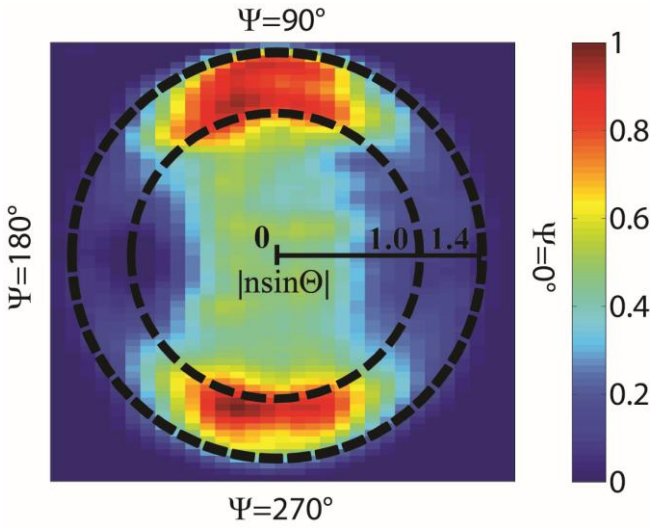

Figure 3.5. Raman emission pattern of thiophenol 1074 cm^{-1} Raman line retrieved from EMS measurements. Color map represents the scattering intensity normalized by the maximum intensity. Inner and outer black dashed circles indicate the critical angle at the air-glass interface and the NA of objective lens, respectively.

With the defined coordinates, we can estimate that the two main emission lobes of the Raman scattering from the dimer antennas peak in the following directions: (Θ = 139.5°, Ψ = 100°) and (Θ = 139.5°, Ψ = 260°). It can be seen that the azimuthal angles are close to the expected values of Ψ = 90° and 270°. Both measured polar angles Θ are close to the critical angle at the air-glass interface (138.2 °) within the measurement resolution. The full-width-at-half-maximum (FWHM) contours of the two beams have widths of (ΔΘ = 22°, ΔΨ = 48°) and (ΔΘ = 15°, ΔΨ = 48°). We define the front-to-back (F/B) ratio as the ratio of integrated emission power within these two FWHM contours. The ratio between the power radiated into +y (Ψ = 90 °, defined as forward direction) and

-y (Ψ = 270°, defined as backward direction) is very close to unity (1.01), as expected from the symmetry of the dimer antenna.

One powerful attribute of the EMS technique is that it allows reconstruction of the emission patterns of the different Raman lines from one set of measurements, with the only limitation being the spectrometer bandwidth. Figure 3.6(a) and (b) show measured Raman emission patterns corresponding to the Stokes Raman lines of 415 cm^{-1} and 1586 cm^{-1}, respectively. For the Raman line at 415 cm^{-1}, the radiation peaks at (Θ = 139.1°, Ψ = 90.0°) and (Θ = 139.1°, Ψ = 273°), with a measured F/B ratio of 1.12. For the Raman line at 1586 cm^{-1}, the radiation peaks at (Θ = 140.6°, Ψ = 87°) and (Θ = 140.6°, Ψ = 273°), with a measured F/B ratio of 1.09. Figures 3.5 and 3.6 indicate that, for this structure, the different Raman lines have similar radiation patterns. This is because these Raman lines are enhanced by the same dipolar mode of the dimer antenna, whose radiation pattern varies little over the wavelengths of the different Raman lines [2].

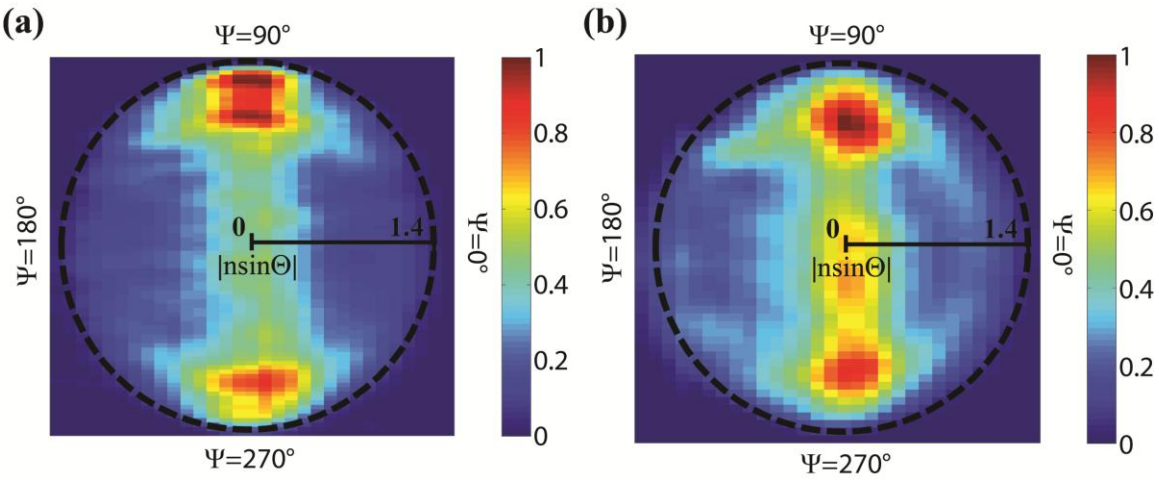

Figure 3.6. Raman emission pattern for (e) 415 cm^{-1} Raman line and (f) 1586 cm^{-1} Raman line, retrieved from same measurement as Fig. 3.5.

3.4 Conclusions

In conclusion, we directly observe the Raman emission pattern from dimer antennas placed on dielectric substrates. Dimer antennas are a very common design for SERS substrates, but most of the enhanced Raman scattering occurs into the substrate, peaking around the critical angle. Therefore, in the absence of an oil-immersion objective with a high NA, this light is trapped by the substrate. One could roughen the backside of the substrate for better light extraction, but the objective lens would still need to have a large NA. In addition, the LSPR of dimer antennas is broad, with the different Raman lines therefore having quite similar emission patterns. If the different Raman lines had different emission patterns, then an extra degree-of-freedom in the design of sensor systems based on SERS would be provided. With these considerations in mind, we consider two directional antenna designs in the following chapters.

References

[1] K. B. Crozier, A. Sundaramurthy, G. S. Kino, and C. F. Quate, "Optical antennas: Resonators for local field enhancement," J. Appl. Phys. **94**, 4632–4642 (2003).

[2] T. H. Taminiau, F. D. Stefani, F. B. Segerink, and N. F. van Hulst, "Optical antennas direct single-molecule emission," Nat. Photon. **2**, 234–237 (2008).

[3] A. G. Curto, G. Volpe, T. H. Taminiau, M. P. Kreuzer, R. Quidant, and N. F. van Hulst, "Unidirectional emission of a quantum dot coupled to a nanoantenna.," Science **329**, 930–933 (2010).

[4] T. Shegai, B. Brian, V. D. Miljković, and M. Käll, "Angular distribution of surface-enhanced Raman scattering from individual au nanoparticle aggregates.," ACS Nano **5**, 2036–2041 (2011).

[5] H. Aouani, O. Mahboub, E. Devaux, H. Rigneault, T. W. Ebbesen, and J. Wenger, "Plasmonic antennas for directional sorting of fluorescence emission.," Nano Lett. **11**, 2400–2406 (2011).

[6] K. G. Lee, X. W. Chen, H. Eghlidi, P. Kukura, R. Lettow, A. Renn, V. Sandoghdar, and S. Go, "A planar dielectric antenna for directional single-photon emission and near-unity collection efficiency," Nat. Photon. **5**, 166–169 (2011).

[7] M. A. Lieb, J. M. Zavislan, and L. Novotny, "Single-molecule orientations determined by direct emission pattern imaging," J. Opt. Soc. Am. B **21**, 1210–1215 (2004).

[8] K. Kneipp, Y. Wang, H. Kneipp, L. T. Perelman, I. Itzkan, R. R. Dasari, and M. S. Feld, "Single Molecule Detection Using Surface-Enhanced Raman Scattering (SERS)," Phys. Rev. Lett. **78**, 1667–1670 (1997).

[9] S. Nie and S. R. Emory, "Probing Single Molecules and Single Nanoparticles by Surface-Enhanced Raman Scattering," Science **275**, 1102–1106 (1997).

[10] D. Wang, T. Yang, and K. B. Crozier, "Optical antennas integrated with concentric ring gratings: electric field enhancement and directional radiation.," Opt. Express **19**, 2148–2157 (2011).

[11] Y. Chu, W. Zhu, D. Wang, and K. B. Crozier, "Beamed Raman: directional excitation and emission enhancement in a plasmonic crystal double resonance SERS substrate.," Opt. Express **19**, 20054–20068 (2011).

[12] A. Ahmed and R. Gordon, "Directivity enhanced Raman spectroscopy using nanoantennas.," Nano Lett. **11**, 1800–1803 (2011).

[13] D. Wang, W. Zhu, Y. Chu, and K. B. Crozier, "High Directivity Optical Antenna Substrates for Surface Enhanced Raman Scattering.," Adv. Mater. **24**, 4376–4380 (2012).

[14] A. Ahmed and R. Gordon, "Single molecule directivity enhanced Raman scattering using nanoantennas.," Nano Lett. **12**, 2625–2630 (2012).

[15] D. P. Fromm, A. Sundaramurthy, A. Kinkhabwala, P. J. Schuck, G. S. Kino, and W. E. Moerner, "Exploring the chemical enhancement for surface-enhanced Raman scattering with Au bowtie nanoantennas.," J Chem. Phys. **124**, 61101 (2006).

[16] M. Beversluis, A. Bouhelier, and L. Novotny, "Continuum generation from single gold nanostructures through near-field mediated intraband transitions," Phys. Rev. B **68**, 115433 (2003).

[17] T. H. Taminiau, S. Karaveli, N. F. van Hulst, and R. Zia, "Quantifying the magnetic nature of light emission," Nat. Commun. **3**, 979 (2012).

Chapter 4 Raman emission pattern from Yagi-Uda antennas

Molecules can be identified through their Raman scattering spectra, as these are associated with their characteristic vibrational energy states. Surface-enhanced Raman scattering (SERS) is a technique that uses nanostructures to enhance the Raman cross-section of molecules by orders of magnitude. To achieve larger enhancement has been the main focus in design of such nanostructures. Recently, the importance of directionality of SERS has been recognized, since it facilitates efficient excitation and efficient collection [1]. At radio frequencies, Yagi–Uda antennas are frequently used for their directional properties. Nanoscale YU antennas [2,3] have been shown to produce directional emission from quantum dots [4]. In this chapter, we discuss the application of Yagi–Uda antenna for SERS, and experimentally demonstrate that a nanoscale Yagi–Uda antenna can effectively direct Raman scattering into one specific direction.

4.1 Nanoscale Yagi–Uda antenna design

Like its radio frequency counterpart, the nanoscale Yagi–Uda antenna has three components: the feed, the reflector and the directors. One such Yagi–Uda antenna design is shown in Figure 4.1(a). The feed boosts the excitation of, and emission from, nanoscale

emitters. Here, it is a dimer antenna that has the same dimension as the one described in Chapter 3, whose LSPR peaks at wavelength of λ = 857 nm, as shown by the measurements of Figure 4.1(b). The reflector and directors provide antenna directivity. The widths of both the reflector and directors are 65 nm, while the length is varied to achieve the Yagi–Uda functionality at an operating wavelength of 857 nm. The reflector has length 187 nm. The LSPR of this reflector is around λ = 902 nm, which is red-shifted compared to the operating wavelength of 857 nm, as shown in Figure 4.1(b). The three nanoparticles to the right of the feed antenna are directors. The length of each director is 139 nm. The LSPR of these directors is around λ = 765 nm, which is blue-shifted compared with the operating wavelength. The distances between the nanoparticles also play an important role in Yagi–Uda antenna design [2]. The reflector is 187 nm from the feed, while the distance between the feed and its adjacent director is 214 nm. The spacing between each director is also 214 nm.

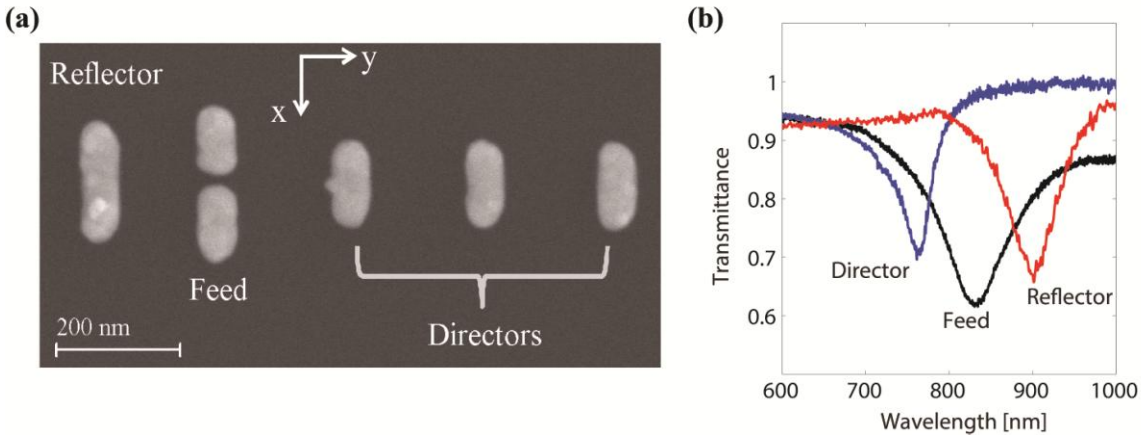

Figure 4.1. Nanoscale Yagi–Uda antenna design. (a) SEM image of one fabricated Yagi–Uda antenna with the feed, the reflector, and the directors. (b) LSPR measured for these Yagi–Uda antenna components.

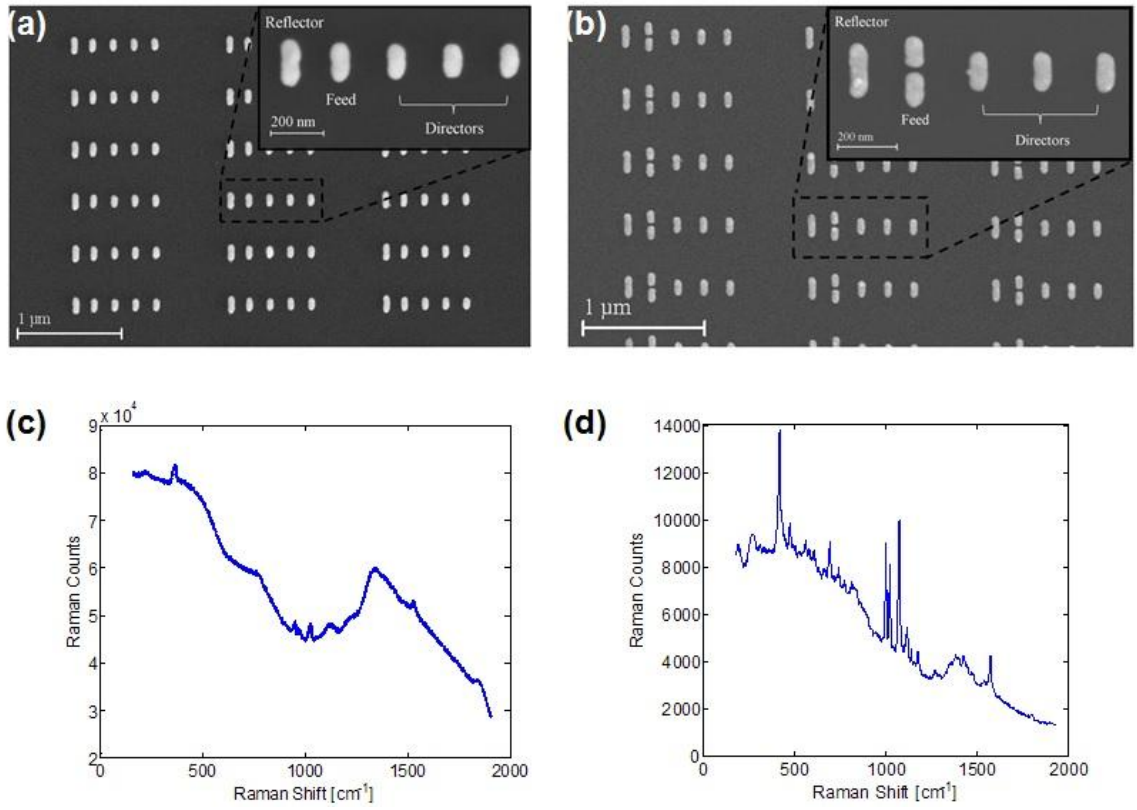

Figure 4.2. Yagi–Uda antennas with different feed antennas. SEM images of Yagi–Uda antennas with nanoparticle (a) monomer and (b) dimer as feed. SERS spectra measured for Yagi–Uda antennas with nanoparticle (c) monomer and (d) dimer as feed.

As distinct from previous nanoscale Yagi–Uda antenna designs, we use a dimer antenna, rather than a single nanorod monomer, as the feed antenna in order to use the gap mode [5] to further enhance Raman scattering [6]. This would allow us to achieve a high signal-to-background ratio in the EMS measurements. For comparison purposes, we fabricate Yagi–Uda antennas with identical reflectors and directors, but different feed structures, as shown in Figure 4.2(a) and (b), respectively. The operating wavelengths of both Yagi–Uda antenna designs are still at 857 nm. A laser power of 9.3 mW is used for the SERS measurements on the Yagi–Uda with the monomer, while 2.4 mW is used for Yagi–Uda with the dimer. The procedures used for the SERS measurements are the same

as those described in Chapter 1. The SERS enhancement factor (EF) is then found to be 9.6×10^5 for Yagi–Uda with the monomer and 7.4×10^6 for Yagi–Uda with the dimer. The dimers, therefore, achieve an ~8 times improvement in SERS EF over the monomers.

4.2 Measured Raman emission pattern

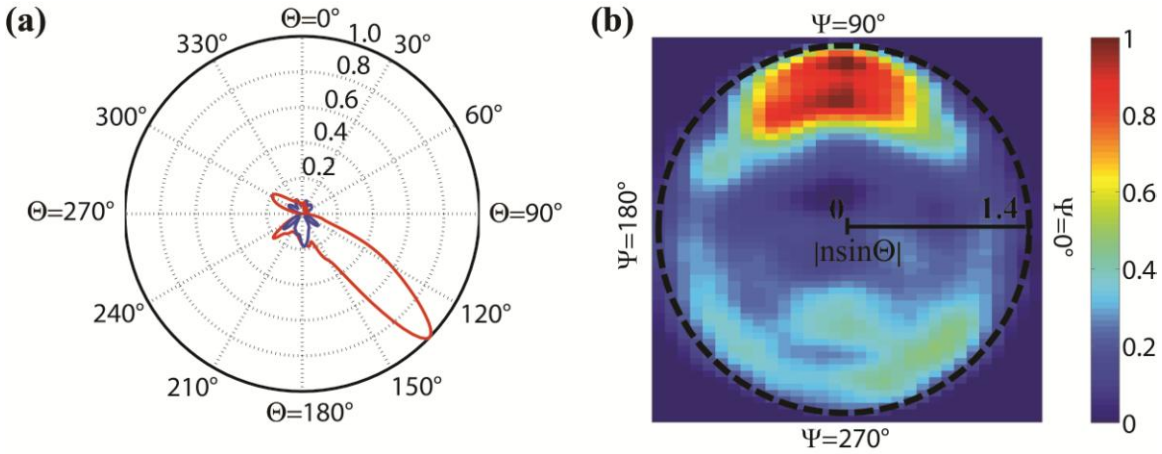

Figure 4.3. Raman emission pattern of Yagi–Uda antenna. (a) FEM simulation of emission pattern resulting from an electric dipole (free space wavelength λ = 857 nm) placed in center of gap of feed element of YU antenna. Red: emission pattern in yz-plane; blue: emission pattern in xz-plane. (b) Emission pattern of thiophenol 1074 cm^{-1} Raman line retrieved from EMS measurements. Color map represents the normalized scattering intensity. Black dashed circles denote NA of objective lens.

We investigate the Raman emission patterns of the Yagi–Uda antennas by simulating the far-fields resulting from a dipole placed in each of these structures. As described in Chapter 3, the antennas are made in arrays for experimental convenience. The Yagi–Uda antenna simulations, however, are performed for single, isolated antennas, rather than for the entire array. Figure 4.3(a) shows the simulated radiation pattern, found

by situating an electric dipole with a free space wavelength of $\lambda = 857$ nm in the center of gap of the feed, and monitoring the far-field intensities. It can be seen that most of the Raman scattering is predicted to occur in the forward direction, with the backward scattering being suppressed. The F/B ratio is predicted by the simulation to be ~4.4.

To observe directional emission from the Yagi–Uda antennas, we form a SAM of thiophenol on the feed sections only. This is achieved by coating the sample with a layer of e-beam resist (PMMA), then performing electron-beam lithography and development to open windows in the resist on the feed sections. Figure 4.3(b) shows the measured emission pattern of the 1074 cm^{-1} Raman line. An underlying ring shape pattern can be seen, similar to that occurring for a dipolar mode radiating above a dielectric substrate shown in Figure 3.2. One key difference of Figure 4.3(b) from Figure 3.2, however, is that the Raman scattering is now predominantly emitted into the direction at ($\Theta = 137.5°$, $\Psi = 90.0°$), with the FWHM contour having widths of $\Delta\Theta = 42°$ and $\Delta\Psi = 70°$. The angle of Ψ is consistent with the forward direction of the Yagi–Uda antenna (pointing from reflector to director). The measured F/B ratio is 2.21, indicating the Yagi–Uda antenna effectively directs Raman scattering into the forward direction.

We also study the directivity of the emission patterns of other Raman lines. Figures 4.4(a) and (b) show the measured emission patterns for the Raman lines at 415 cm^{-1} and 1586 cm^{-1}, respectively. The radiation in the forward direction is still larger than that in backward direction in both cases. However, the measured F/B ratio for Figure 4.4(a) is 1.34 and that for Figure 4.4(b) is 1.15. From these measurements, we can estimate that our design of Yagi–Uda antennas has an F/B ratio above unity over a

bandwidth of 85 nm. This is the same order of magnitude as the FWHM of the LSPR of each nanoparticle, or pair of nanoparticles, of the Yagi–Uda antenna.

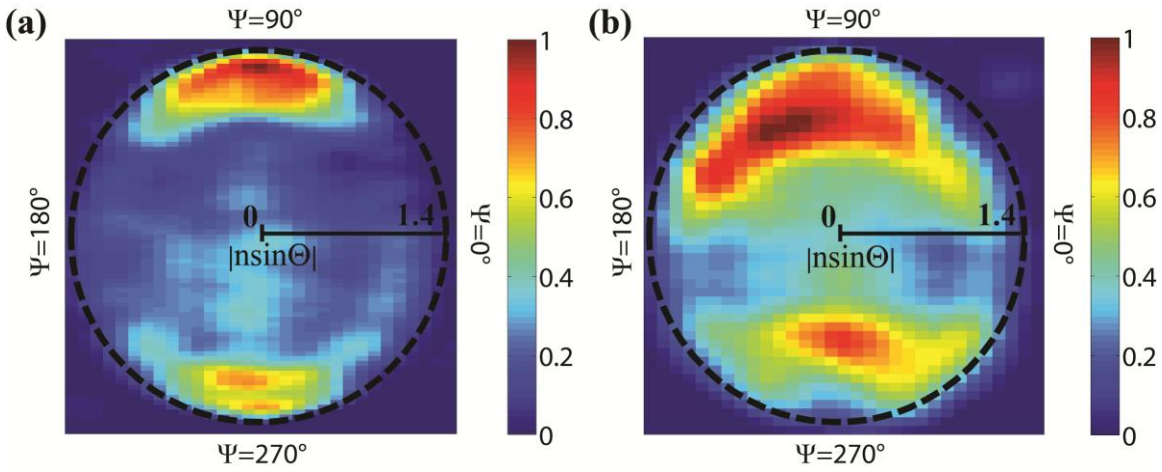

Figure 4.4. Measured emission patterns from Yagi–Uda antennas at (e) 415cm^{-1} Raman line and (f) 1586 cm^{-1} Raman line.

4.3 Functionality of directors and reflector

Yagi–Uda antennas rely on the near-field coupling between the LSPRs on the feed, directors and reflector to achieve directional radiation. The high EF provided by the feed dimer antenna enables us to study the functionalities of each component of the Yagi–Uda antenna. Figure 4.5(a) shows a Yagi–Uda antenna with the same design as before, but without the directors. Again, a SAM of thiophenol is formed solely on the feed dimer part. Figure 4.5(b) shows the emission pattern of the 1074 cm^{-1} Raman line found using the EMS technique. It can be seen that majority of the scattering radiates into forward direction with an F/B ratio of 3.56. The azimuthal FWHM of $\Delta\Psi = 85°$ is, however, larger than that of the full Yagi–Uda design. The results confirm that the reflector reflects

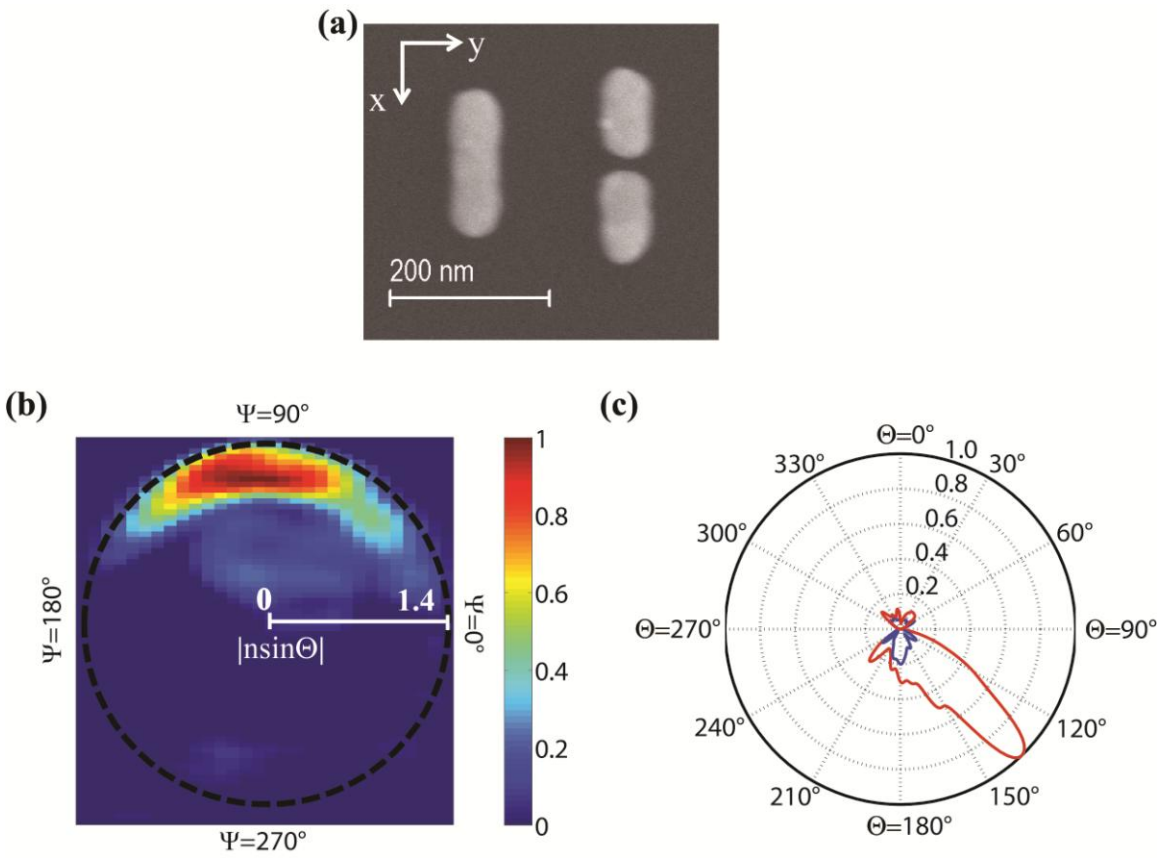

Figure 4.5. Function of the reflector in Yagi–Uda antenna. (a) SEM and (b) measured emission pattern at 1074 cm^{-1} Raman line from Yagi–Uda antenna without directors. (c) FEM simulation of emission pattern from Yagi–Uda antenna without directors. Red: emission pattern in yz-plane; blue: emission pattern in xz-plane.

radiation into the forward direction, thereby increasing the F/B ratio. This trend is also confirmed by simulations, where the Yagi–Uda antenna without directors (Figure 4.5(c)) is predicted to achieve a F/B ratio of 3.75.

We next perform experiments on a Yagi–Uda antenna with the same design as before, but without the reflector (Figure 4.6(a)). The emission pattern of the 1074 cm^{-1} Raman line is found by the EMS technique (Figure 4.6(b)). Due to the absence of reflector, a significant amount of Raman scattering is visible in the backward direction, with the F/B ratio reduced to 1.42. However, the radiation is more confined in the

azimuthal direction, with the azimuthal FWHM being $\Delta\Psi = 71°$, a reduction of ~16% over the director-free Yagi–Uda antenna. This trend is again confirmed by simulations. The Yagi–Uda antenna without reflectors (Figure4.6(c)) is predicted to achieve a F/B ratio of 1.71. Therefore, we conclude that the reflectors increase the F/B ratio; while the directors shape the radiation pattern of the main lobe to reduce its angular spread.

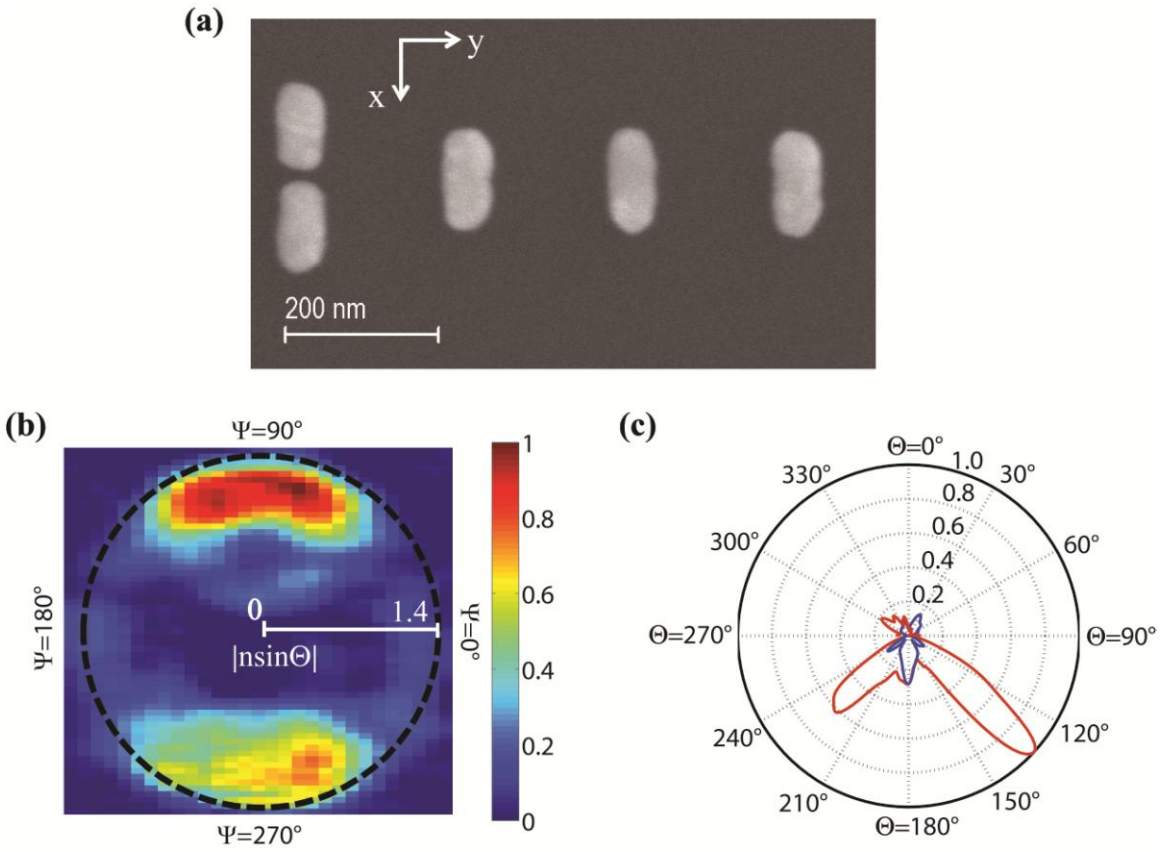

Figure 4.6. Function of the directors in Yagi–Uda antenna. (a) SEM and (b) measured emission pattern at 1074 cm^{-1} Raman line from Yagi–Uda antenna without reflectors. (c) FEM simulation of emission pattern from Yagi–Uda antenna without reflectors. Red: emission pattern in yz-plane; blue: emission pattern in xz-plane.

4.4 Conclusions

In conclusion, we measure the Raman scattering radiation patterns modified by nanoscale Yagi-Uda antenna. By modifying the feed structure using a dimer antenna, the overall SERS intensity is significantly enhanced. Through the emission pattern measurements, the reflector and director antennas in Yagi–Uda antenna design effectively directs Raman scattering into forward direction. Raman emission patterns at different Raman lines indicate that the working bandwidth of the designed Yagi–Uda is around 85 nm. The study of directional Raman scattering would further facilitate optical antenna designs to achieve efficient excitation and efficient collection for SERS.

References

[1] Y. Chu, W. Zhu, D. Wang, and K. B. Crozier, "Beamed Raman: directional excitation and emission enhancement in a plasmonic crystal double resonance SERS substrate.," Opt. Express **19**, 20054–20068 (2011).

[2] T. Kosako, Y. Kadoya, and H. F. Hofmann, "Directional control of light by a nano-optical Yagi – Uda antenna," Nat. Photon. **4**, 312–315 (2010).

[3] D. Dregely, R. Taubert, J. Dorfmüller, R. Vogelgesang, K. Kern, and H. Giessen, "3D optical Yagi-Uda nanoantenna array.," Nat. Commun. **2**, 267 (2011).

[4] A. G. Curto, G. Volpe, T. H. Taminiau, M. P. Kreuzer, R. Quidant, and N. F. van Hulst, "Unidirectional emission of a quantum dot coupled to a nanoantenna.," Science **329**, 930–933 (2010).

[5] M. Schnell, A. Garcia-Etxarri, A. J. Huber, K. Crozier, J. Aizpurua, and R. Hillenbrand, "Controlling the near-field oscillations of loaded plasmonic nanoantennas," Nat. Photon. **3**, 287–291 (2009).

[6] W. Zhu, M. G. Banaee, D. Wang, Y. Chu, and K. B. Crozier, "Lithographically fabricated optical antennas with gaps well below 10 nm.," Small **7**, 1761–1766 (2011).

Chapter 5 Beamed Raman scattering from dimer antennas integrated with plasmonic substrate

In surface-enhanced Raman scattering (SERS), the Raman cross-section of molecules adsorbed to nanostructures can be increased by orders of magnitude. SERS has attracted renewed attention lately, spurred by demonstrations of single-molecule sensitivity [1]. Increasing the adoption of the SERS technique further, however, requires fabrication methods capable of routinely delivering reproducible substrates with high average SERS EFs. In Chapter 2, we have demonstrated lithographically fabricated optical antennas with gap size well below 10 nm and shown SERS EFs of 1.1×10^8. On the other hand, the combination of dimer antennas with propagating surface plasmon polaritons on planar metal surfaces [2] or metal-insulator-metal waveguides [3,4] has been studied as a means for achieving beamed Raman scattering or DERS. Here, we integrate the dimer antennas with plasmonic substrate that consists of a gold film and one-dimensional (1D) gratings. This integrated device boosts the overall SERS EF ~77 times, as the incident field is efficiently coupled to the dimer gap center. We also show that the collection efficiency is improved by using such integrated device. Beamed Raman scattering is observed and hence allows efficient Raman detection using objective lens with low NA.

5.1 Integrated device with improved SERS EF

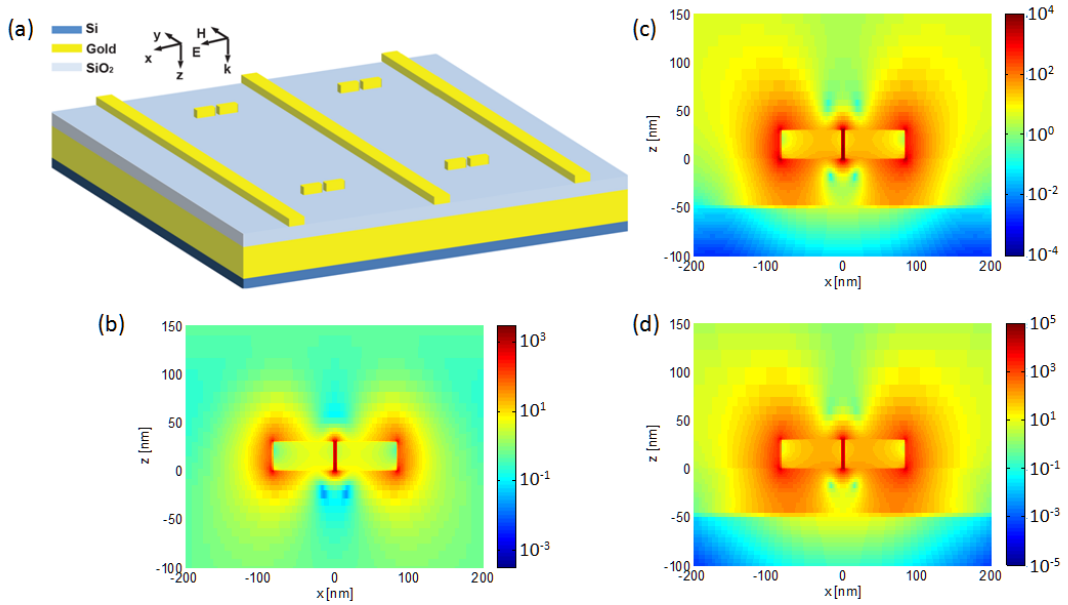

Figure 5.1 Simulation of integrated structure. (a) Schematic of the integrated structure: a two-dimensional (2D) gold dimer antenna array on top of the plasmonic substrate. The plasmonic substrate consists of a gold film, a SiO_2 spacer layer, and 1D gold gratings. (b-d) Intensity enhancement ($|E|^2$) on xz-plane through center of different structures. (b) Dimer antenna with 4 nm gap on SiO_2 substrate; (c) the integrated device but without 1D gold grating; and (d) the integrated structure.

As shown in Figure 5.1(a), the structure we introduce integrates dimer antennas with a plasmonic substrate. The plasmonic substrate consists of a gold film, an SiO_2 spacer layer and a 1D grating of gold nanostrips. In the simulation, the dimer antennas are pairs of gold rods, each 80 nm long, 60 wide, and 30 thick, separated by a gap of 4 nm. They exhibit a localized surface plasmon resonance at 800 nm, and all simulations are performed at this wavelength. This wavelength is in between the excitation laser wavelength (785 nm) and the 1074 cm^{-1} Raman line of thiophenol (857 nm), in order to provide plasmonic enhancement for both wavelengths [5]. We first calculate the field intensity enhancement ($|E|^2$) of an array of optical antennas on a glass substrate, with

periods of 730 nm along the x- and y-axes, respectively, using the FDTD method. This enhancement represents the field intensity ($|E|^2$) normalized to the field intensity of the illumination (normally-incident plane wave, Figure 5.1(a)). In Figure 5.1(b), the field intensity enhancement is plotted along an xz cross section through the antenna, with peak enhancement 1.8×10^3. We next consider the addition of a reflector, consisting of a gold film (120 nm thick) and a SiO_2 spacer (50 nm thick). This layer simultaneously supports surface plasmon polaritons (SPPs) and increases field enhancement because of image charges [3]. Figure 5.1(c) shows the field intensity enhancement in this configuration, with peak enhancement 1.1×10^4. This is ~ 6 times larger than the maximum intensity without the reflector. We next consider the addition of the 1D grating of gold nanostrips. Grating strips are used to diffract free space illumination into surface waves on the gold film with SiO_2 spacer, in a way that maximizes the field enhancement around the dimer antennas. Each grating strip is 100 nm wide and 30 nm thick. The antennas are positioned at the midpoints between the strips. The peak intensity enhancement is therefore increased to 3.5×10^4 (Figure 5.1(d)). This is ~ 3 times larger than the antenna plus reflector and ~ 19 times larger than the antennas-on-glass. We therefore expect a large SERS EF from this structure, with the grating increasing the excitation field and collimating the Raman scattering.

Fabrication of the device is performed by e-beam lithography and lift-off. First, gold and SiO_2 are deposited onto a silicon substrate to form the reflector. Next, gratings are fabricated by e-beam lithography and lift-off. Alignment marks are also fabricated in this step. A thin SiO_2 layer (2 nm) is deposited on the grating so that later, when the substrate is soaked in thiophenol, molecules are adsorbed to the antennas, rather than

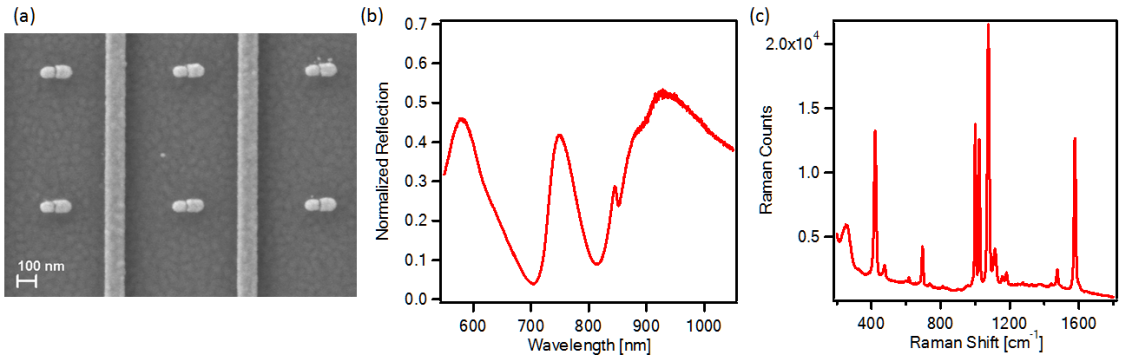

Figure 5.2 Characterization of integrated device. (a) SEM of structure: plasmonic nanogap antennas integrated with reflector and grating. (b) Measured reflection spectrum of structure normalized to reflection of gold film plus SiO_2 spacer. (c) SERS spectrum of thiophenol monolayer on structure. Laser excitation at λ=784 nm, with power of 0.62 mW. A 5× objective lens (NA=0.15) used to focus the illumination and collect the Raman signal. Integration time of the detector is 5 s.

gratings. Dimer antennas with ~ 4 nm gaps are fabricated, using the method of Chapter 2. The use of alignment marks ensures that the antennas are formed at the midpoints between strips (to within 5 nm). Figure5. 2(a) shows an SEM of the fabricated structure. Figure 5.2(b) shows the normalized reflection spectrum of the sample. Hybridization between the SPPs and localized surface plasmons on the gold strips leads to a resonance at 700 nm and a (weaker) resonance at 900 nm. Due to the fact that the illumination is not purely at normal incidence, with the objective lens provides a range of incident angles, a resonance at 850 nm is excited [6]. Most importantly, there is a resonance at 810 nm, arising from the localized surface plasmon resonance of the antennas that, amongst the resonances discussed, provides the largest near field enhancement. At this wavelength, surface waves are diffracted by the grating strips to produce enhanced fields at the antenna locations. Figure 5.2(c) shows the SERS spectrum of a self-assembled thiophenol monolayer formed on the antennas. The excitation wavelength for each sample is selected such that the mean value of the laser and Stokes wavelengths matches the antenna

resonance (810 nm), to ensure the largest enhancement factor. By comparing the SERS spectrum to the Raman spectrum measured from pure thiophenol, the EF is found to be 8.5×10^{9} for the 1074 cm^{-1} Raman line. We assume that all exposed gold surfaces are covered by monolayers of thiophenol. The EF represents the average enhancement of all of these molecules, rather than that of only the molecules in the hot spots of the antenna gaps, for which the enhancement should be far higher. The EF from antennas with similarly-sized gaps on glass has previously been shown to be 1.1×10^{8} in Chapter 2. The addition of the reflector and 1D grating, therefore, increases the EF by ~ 77 times.

5.2 Simulation of Raman emission pattern from periodic structures — Optical reciprocity theorem and bandstructure

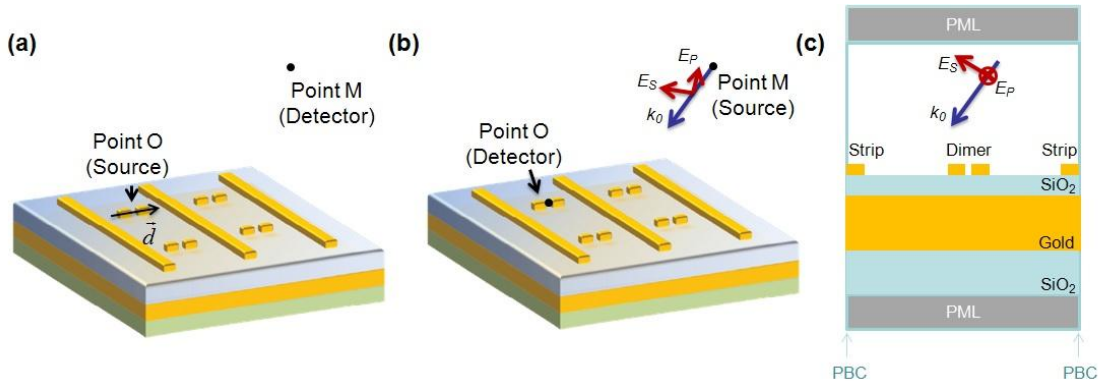

Figure 5.3. Optical reciprocity theorem (ORT) for simulating the emission from periodic structures. (a) Schematic depicting situation in which a single dipole $\vec{\boldsymbol{d}}$, is placed in the center gap of a dimer antenna. (b) Schematic depicting complementary simulation, in which a plane wave is obliquely incident on the 2D dimer array. (c) Schematic depicting cross-section of complementary simulation in which a plane wave is obliquely incident on the unit cell of the 2D dimer array, with PBC on both sides.

Periodic effects are important for the SERS substrate consisting of the dimer antennas on the plasmonic substrate. To simulate the emission pattern from such integrated device, the goal is to find the emission pattern generated when a dipole $\vec{d}$ is located in the center gap of one of the dimers of the array; it is schematically shown in Figure 5.3(a). This cannot be directly simulated, i.e. using the method outlined in the Chapter 4 but with periodic boundary conditions, since this would model the case of an array of coherent dipoles. That situation differs from that encountered in our experiments.

The optical reciprocity theorem (ORT) permits us to find the emission patterns using the results of a complementary set of simulations that find the fields at the gap center for plane waves incident on the structure in different directions. The ORT states that the field $\vec{E}$ created at a given point M by a dipole $\vec{d}$ at point O is related to the field $\vec{E}_2$ at O created by a dipole $\vec{d}_2$ at M according to $\vec{d} \cdot \vec{E}_2 = \vec{d}_2 \cdot \vec{E}$. The ORT is especially useful for simulations on SERS, and is described in detail elsewhere [2,7]. Here we use this method to simulate the emission pattern from the device consisting of dimer antennas on the plasmonic substrate.

In the complementary set of simulations we perform, the fields at the gap center are found for plane waves incident from different directions (Θ, Ψ), as shown in Figure 5.3(b). To simulate this structure, periodic Bloch boundary conditions (PBC) are applied at the x- and y-boundaries of the simulation space (Figure 5.3(c)). As described further elsewhere [2,7], to find the polar and azimuthal polarization components of the far-field emission, the complementary set of simulations need to include both TE and TM polarization. By applying the ORT to the results of the complementary set of simulations, the emission patterns from the integrated structure are found, which will be shown later.

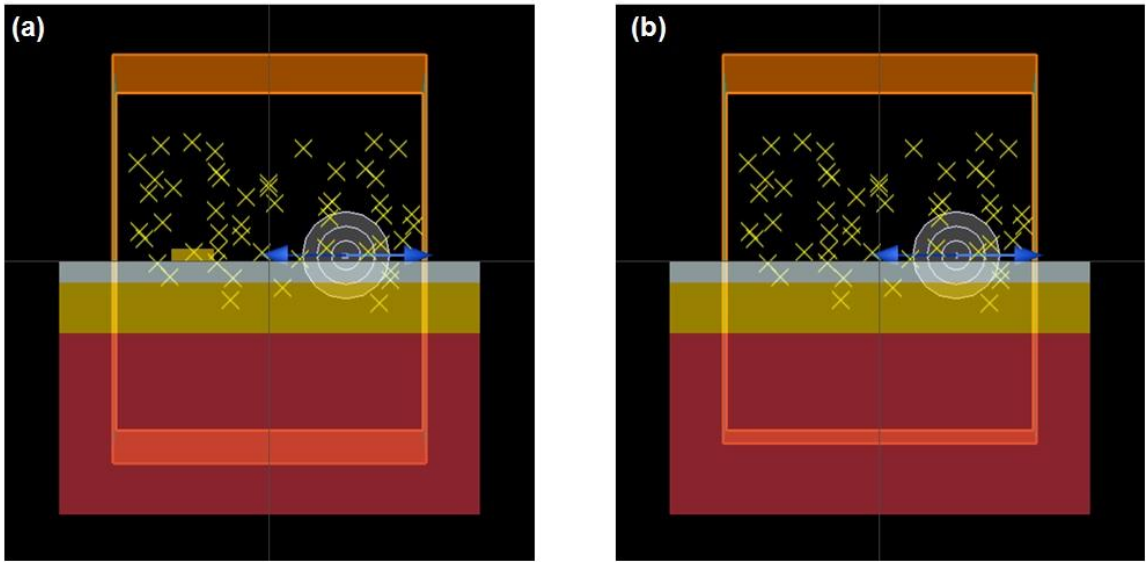

Figure 5.4. FDTD simulation domain to calculate bandstructures of plasmonic substrate along (a) x-axis and (b) y-axis. Blue arrows: electric dipole source. Yellow crosses: randomly placed field monitors. Orange frame: FDTD simulation domain; yellow block: gold; gray block: SiO_2; red block: silicon.

The bandstructure of the plasmonic substrate along the x- and y-axes are calculated separately using 2D finite-difference time-domain (FDTD) method (Lumerical®). A time-domain technique is used here as it allows calculation of broadband response with one simulation. The simulations employ a point dipole with Bloch boundaries to find what modes can be excited in the plasmonic substrate. It should be noted that this simulation configuration differs from that employed in Figure 5.3, since we are interested here in finding the bandstructures rather than the emission pattern. As is described in the following text, these bandstructure simulations explain the important features of the observed beamed Raman scattering. Along the x-axis, the simulation domain encloses one unit cell (periodicity of 730 nm) of the structure (Figure 5.4(a)). The structure consists of layer of SiO_2 and gold on a silicon substrate, and there are gold strips on the SiO_2 layer. The region above the structure is air. Along the y-axis, the simulation

domain encloses one unit cell (periodicity of 730 nm) of the structure (Figure 5.4(b)). The structure is the same as that used for the simulations along the x-axis, but without the gold strips. The region above the structure is air. PBCs are used at the x-axis/y-axis boundaries and PMLs are used at the z-axis boundaries. A horizontally-oriented dipole is placed at a distance of 15 nm from the SiO_2 surface to represent the dipolar mode of the dimer antenna. The dipole is placed at the midpoint between the strips (for the x-axis simulations). Groups of time-domain monitors are placed at random locations within the simulation domain. This eliminates the possibility of symmetry preventing some of the modes from being detected. The time-domain waveforms are apodized to amplify the long-lasting resonance modes. The frequency response is then calculated from these apodized waveforms using the fast Fourier transform (FFT) and summed up over the different monitor points. Thus the intensity map of the bandstructures represents the relative coupling efficiency between the surface modes of the plasmonic substrate with the dimer dipolar mode at each frequency. The simulations are swept across the Bloch conditions from $k = 0$ to $k = \pi/G$ to acquire the frequency response at different wavenumber. This generates the 2D bandstructures shown in the following sections.

5.3 Beamed Raman scattering observed from integrated structure

We again use EMS technique described in Chapter 4 to measure the Raman emission pattern from the integrated structure. As distinct from previous measurements, an air

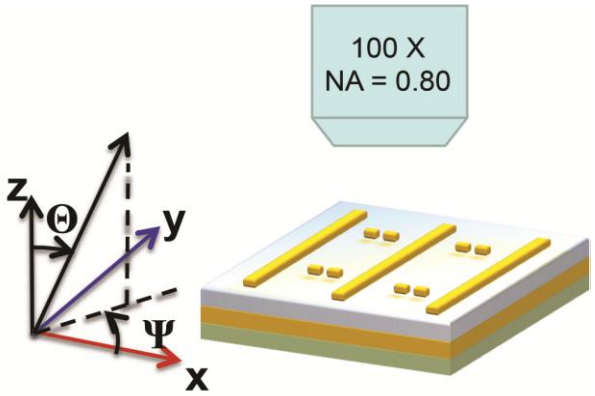

Figure 5.5. Schematic diagram of EMS measurements for the integrated structure., along with the definition of the spherical coordinates.

objective lens (Nikon 100×, NA = 0.8) above the sample is used to excite the Raman scattering and to measure the emission pattern, as shown in Figure 5.5. Figure 5.6(a) shows the direct imaging of the emission pattern of the 1074 cm^{-1} Raman line. No data binning is performed; hence each pixel in this momentum space image corresponds to a momentum of 0.045NA × 0.030 NA. It is observed that the largest Raman scattering is at $\Theta = 0°$ and decreases rapidly at larger angles. The FWHM polar angle of the main lobe is $\Delta\Theta = 6°$ in the x-direction ($\Psi = 0°$) and $\Delta\Theta = 57°$ in the y-direction ($\Psi = 90°$). This substantial collimation of the Raman scattering in the x-direction is due to the fact that both the incident laser polarization and the gold strip periodicity are in this direction. An important consequence is that objective lenses with low NAs can be used with this device without much loss in light collection.

In addition to the emission peak around $\Theta = 0°$, Figure 5.6(a) shows bright and dimmed circular contours. These contours are confirmed in the simulation of Figure 4d. This simulation predicts the emission pattern at $\lambda = 857$ nm that would result, were a point dipole placed in the gap of a dimer antenna. Based on Section 5.2, rather than

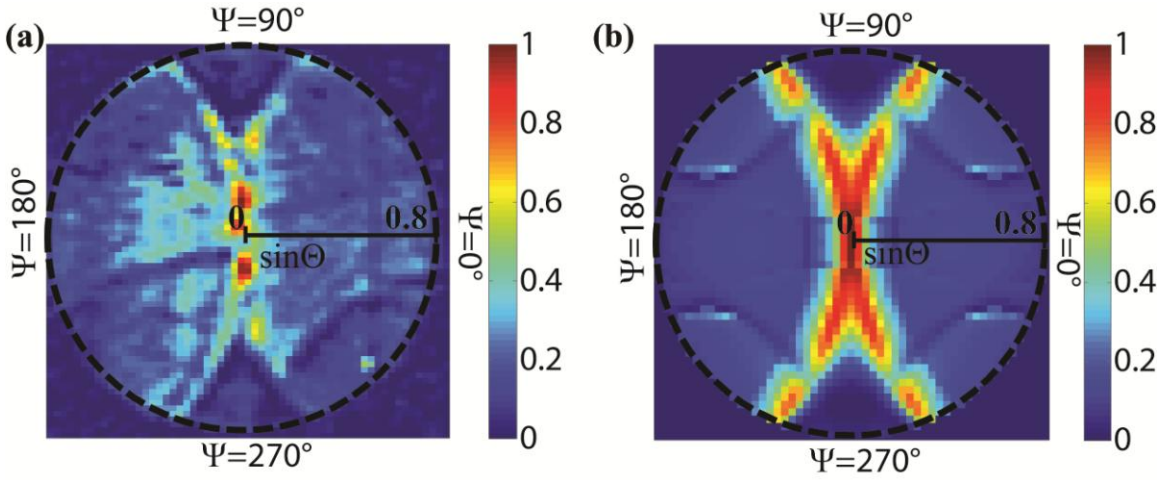

Figure 5.6. Emission pattern of thiophenol 1074 cm^{-1} Raman line. (a) Retrieved from EMS measurements. Color map represents the normalized scattering intensity. Black dashed circle denotes NA of objective lens. (b) Simulated emission pattern (normalized).

simulating this configuration directly, we simulate the fields in the gap that result when plane waves are incident on the device from various angles. We then use these results with the optical reciprocity theorem to predict the emission pattern shown in Figure 5.6(b) [2].

We now discuss the physical interpretation of the emission pattern. To begin, we note that the enhanced Raman scattering from the dimer antenna can be coupled to the surface modes of the plasmonic substrate that can then be diffracted into free space by the 2D dimer antenna array. Therefore, considering this diffraction effect, conservation of momentum in the xy-plane requires:

$$\vec{k}_{in-plane}(\omega) = \pm m\vec{G}_x \pm n\vec{G}_y + \vec{k}_s(\omega) \quad (1)$$

where ω is the frequency of Raman scattering, $\vec{k}_{in-plane}$ is the wavevector of Raman scattering projected in xy-plane, m and n are integers, $\vec{G}_x$ ($\vec{G}_y$) is the reciprocal lattice wavevector of the 2D dimer array along the x (y) axis, and $\vec{k}_s$ is the wavevector of the

surface modes supported by the plasmonic substrate. To facilitate physical interpretation, we simplify the problem as much as possible. Rather than using 3D modeling to find $\vec{k}_s(\omega)$ along all directions within the xy-plane, we instead solely consider waves propagating along the x- and y-axes. We calculate the bandstructures of the plasmonic substrate that shows the dispersion relations $k_{sx}(\omega)$ and $k_{sy}(\omega)$ along each of these axes using the method described in Section 5.2. The modeled structure contains the following layers: air/SiO_2/gold/silicon. The gold dimer antennas are not included explicitly in the modeled structure. Their periodicity, however, is implicitly included through the use of $\vec{G}_x$and $\vec{G}_y$. For waves propagating along the x-axis, the gold strips serve as strong

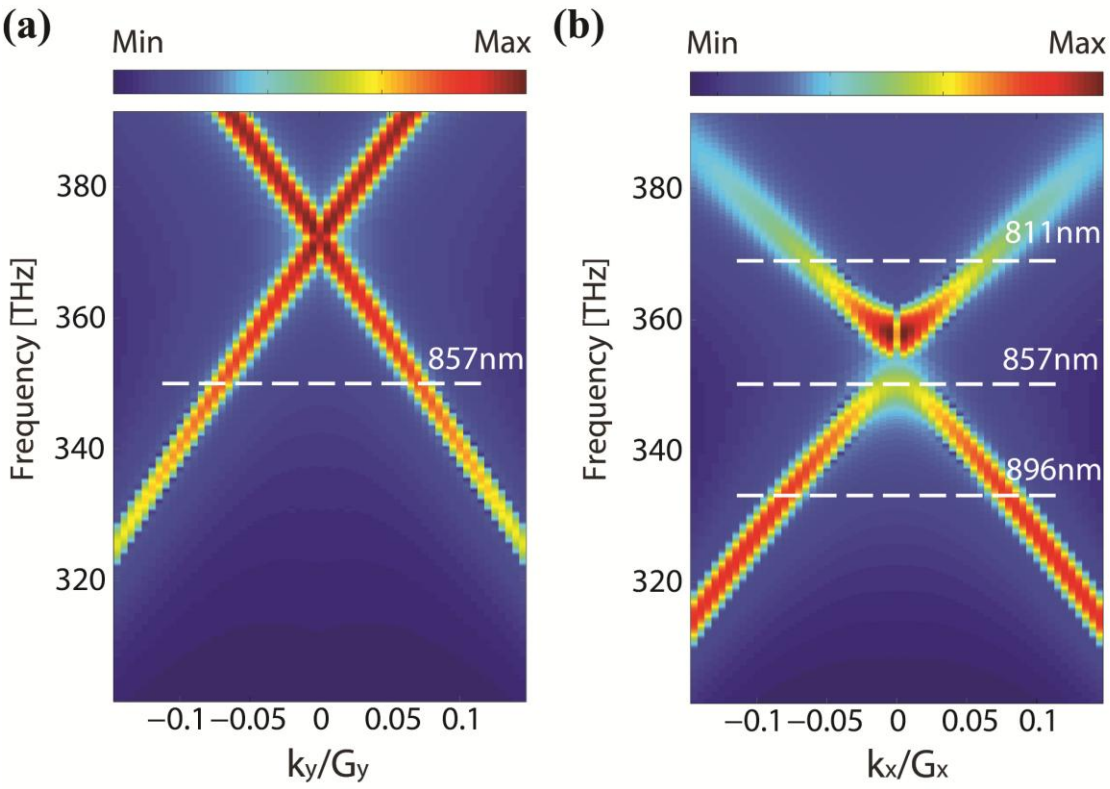

Figure 5.7. Bandstructures of the plasmonic substrate. Color map represents the normalized intensity of the coupled surface modes in log-scale. (a) Bandstructure along y-axis. (b) Bandstructure along x-axis.

periodic scatterers. We therefore include these strips in the modeled structure when finding $k_{sx}(\omega)$. On the other hand, for waves propagating along the y-axis, the gold strips do not serve as periodic scatterers, and we do not include them in the modeled structure. The excitation of surface modes is monitored via sample points randomly positioned within the simulation domain, whose sum is plotted as the color scale in Figures 5.7 (see Supporting Information). The modeled bandstructure along the y-axis is shown as Figure 5.7(a). In a manner analogous to the empty-lattice approximation [8], two dispersion curves can be seen to cross at k_y = 0. These originate from the surface waves shifted by reciprocal lattice vectors $(\pm\vec{G}_y, 0)$. The modeled bandstructure along the x-axis is shown as Figure 5.7(b). It can be seen that there are two dispersion curves that again originate from the surface waves shifted by reciprocal lattice vectors $(\pm\vec{G}_x, 0)$. This time, there is an anti-crossing at k_x = 0. This is akin to what is seen in dielectric photonic crystals [9], and arises from the strong scattering provided by the gold strips.

For any given frequency ω, the right-hand side of Equation (1) represents dispersion contours $\vec{k}_s(\omega)$ of the surface modes offset by integral multiples of the reciprocal lattice vectors of the structure. Figure 5.8 depicts the case for the wavelength of λ = 857 nm. Here, we approximate the dispersion contours as ellipses with semi-axes of $k_{sx}(\omega)$ and $k_{sy}(\omega)$. The detection process is limited by the objective lens NA, marked as the dotted black circle. Note that only the relevant dispersion contours are shown, i.e., those with features within the objective lens NA. At the wavelength of λ = 857 nm, Figure 5.7(b) indicates that the two dispersion curves centered at $(\pm\vec{G}_x, 0)$ meet at k_x = 0, due to the fact that the surface wave propagation constant in the x-direction k_{sx} of the plasmonic substrate matches G_x. Similarly, at the same wavelength, Figure 5.7(a)

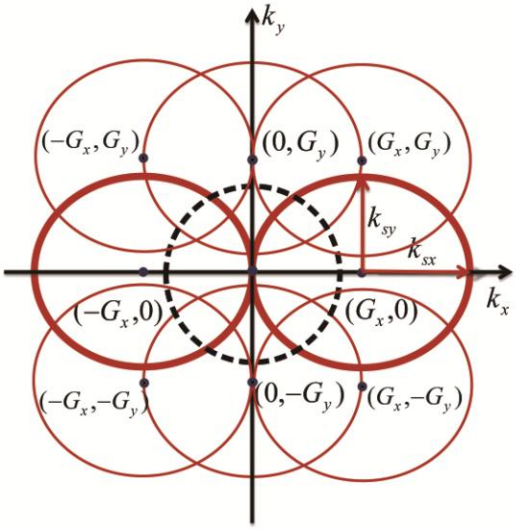

Figure 5.8. Diagram of conservation of momentum in xy-plane according to Equation (1). Dashed black circle represents the NA of objective lens.

indicates that k_{sy} is smaller than G_y. Therefore the 2D momentum diagram in Figure 5.8 shows that two ellipses whose centers lie on x-axis tangentially contact at the origin. This is clearly observed in Figure 5.6. Furthermore, the two ellipses whose centers lie on the y-axis do not touch at the origin. This feature is more difficult to see, but is present in Figure 5.6. Figure 5.8 also indicates that parts of the elliptical momentum contours centered at $(\pm\vec{G}_x, \pm\vec{G}_y)$ are also within the objective lens NA. These features are seen as the four partial ellipses around Ψ = 45 °, 135 °, 225 °and 315 °in Figure 5.6.

5.4 Beamed Raman scattering at other Raman lines

Grating structures usually diffract different frequency components into different directions. As the wavelength moves away from that for which the design is optimized (λ

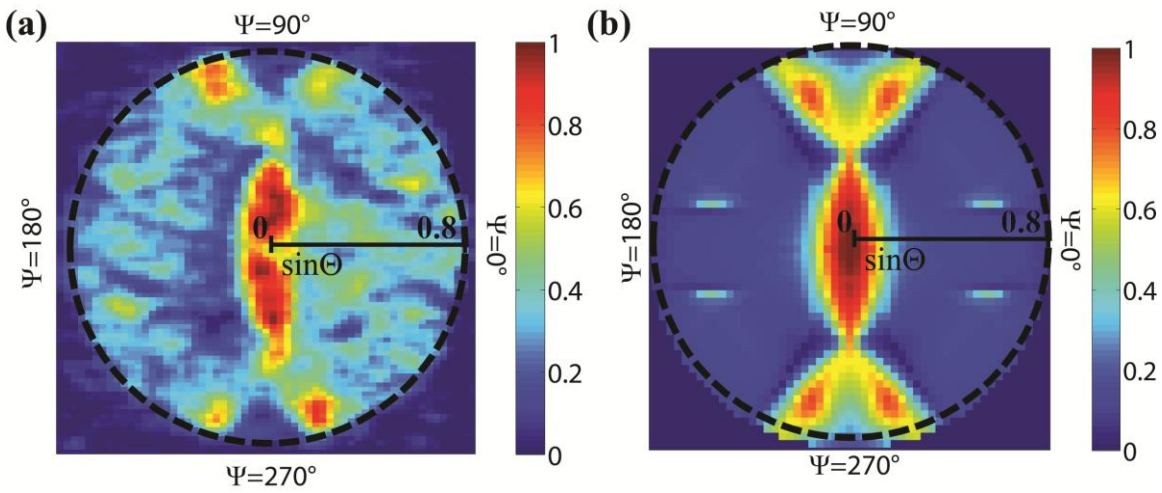

Figure 5.9. Emission pattern of thiophenol 415 cm^{-1} Raman line. (a) Measured by EMS method. (b) Simulated based on ORT method.

= 857 nm), the Raman scattering from the device starts to deviate from being largely surface normal. Figure 5.9(a) shows the EMS measurement results for the Raman line of 415 cm^{-1}. The peak radiation is at $\Theta = 0°$, but the FWHM is increased to $\Delta\Theta = 12°$. This agrees well with the simulation result shown in Figure 5.9(b), which shows peak radiation at $\Theta = 0°$ and an FWHM of $\Delta\Theta = 15°$. Interestingly, both the measured and simulated emission patterns at this wavelength appear to show two intersecting ellipses. This can be understood by considering the surface modes of the plasmonic substrate according to Equation (1). As shown in Figure 5.8, at wavelength of $\lambda = 811$ nm (415 cm^{-1} Raman line), the surface wave propagation constant in the x-direction k_{sx} of the plasmonic substrate becomes larger than G_x, with $|k_x| = |k_{sx} - G_x| = 0.065G_x$. Therefore, in the 2D momentum space along xy-plane, the two ellipses along x-axis shown in Figure 5.8 now have semi-major axes longer than G_x. Therefore the 2D emission patterns in Figure 5.9 show two intersecting ellipses. According to Equation (1), this momentum mismatch would result in two Raman beams being emitted at angles of Θ

= ±4.1 °. However, due to the surface modes having finite linewidths, the two ellipses overlap, resulting in the maximum at Θ = 0 °.

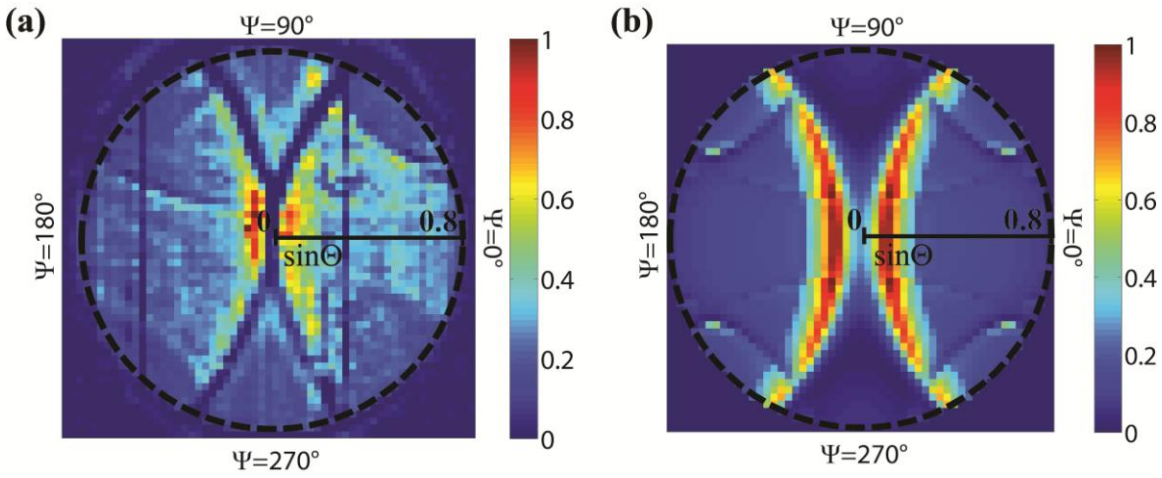

Figure 5.10. Emission pattern of thiophenol 1586 cm^{-1} Raman line. (a) Measured by EMS method. (b) Simulated based on ORT method.

Figure 5.10(a) shows the EMS measurement result for the Raman line at 1586 cm^{-1}. Two radiation branches can be clearly observed with peaks at Θ = ±4 °, in reasonable agreement with the simulations (Figure 5.10(b)) that predict radiation peaks at Θ = ±5 °. We again interpret this phenomenon by referring to Figure 5.8. At a wavelength of λ = 896 nm (1586 cm^{-1} Raman line), the surface wave propagation constant in the x-direction k_{sx} of the plasmonic substrate becomes smaller than G_x, with $|k_x| = |k_{sx} - G_x| = 0.080G_x$. Thus the emission patterns of Figure 5.10 show two ellipses that do not touch. The value of the in-plane momentum predicted by Figure 5.8 suggests that Raman scattering would be mainly diffracted into directions of Θ = ±5.6 °, which is consistent with the experiments (Figure 5.10(a)) and the predictions of simulations (Figure 5.10(b)).

5.5 Conclusions

In conclusion, we have used the energy-momentum spectroscopy technique to directly observe the beamed Raman scattering effect. This technique allows Raman scattering to be distinguished from the broad luminescent background continuum that typically occurs in SERS, thereby enabling the Raman emission patterns from different plasmonic structures to be unambiguously measured. Using this technique, we demonstrate that directional Raman scattering can be achieved by placing additional plasmonic structures around the dimer antennas. In Chapter 4, the Yagi–Uda antenna, these additional structures are directors and reflector. In this chapter, these additional structures are a gold film, a spacer, and gold strips. In both cases, the Raman scattering is shaped into a narrow beam, permitting its efficient collection by a low NA objective lens. This could be advantageous for practical applications in which SERS substrates are used for sensing. The present work is the first direct observation of beamed Raman scattering to the best of our knowledge, and we believe this technique will prove helpful for developing SERS substrates with high collection efficiency.

References

[1] S. Nie and S. R. Emory, "Probing Single Molecules and Single Nanoparticles by Surface-Enhanced Raman Scattering," Science **275**, 1102–1106 (1997).

[2] Y. Chu, W. Zhu, D. Wang, and K. B. Crozier, "Beamed Raman: directional excitation and emission enhancement in a plasmonic crystal double resonance SERS substrate.," Opt. Express **19**, 20054–20068 (2011).

[3] D. Wang, W. Zhu, Y. Chu, and K. B. Crozier, "High Directivity Optical Antenna Substrates for Surface Enhanced Raman Scattering.," Adv. Mater. **24**, 4376–4380 (2012).

[4] A. Ahmed and R. Gordon, "Directivity enhanced Raman spectroscopy using nanoantennas.," Nano Lett. **11**, 1800–1803 (2011).

[5] A. D. McFarland, M. A. Young, J. A. Dieringer, and R. P. Van Duyne, "Wavelength-scanned surface-enhanced Raman excitation spectroscopy," J. Phys. Chem. B **109**, 11279–11285 (2005).

[6] Y. Chu, M. G. Banaee, and K. B. Crozier, "Double-Resonance Plasmon Substrates for Surface-Enhanced Raman Scattering Stokes Frequencies," ACS Nano **4**, 2804–2810 (2010).

[7] E. C. Le Ru and P. G. Etchegoin, "Rigorous justification of the |E|4 enhancement factor in Surface Enhanced Raman Spectroscopy," Chem. Phys. Lett. **423**, 63–66 (2006).

[8] C. Kittel, *Introduction To Solid State Physics*, 8th ed. (John Wiley & Sons, Inc., 2005).

[9] K. Crozier, V. Lousse, O. Kilic, S. Kim, S. Fan, and O. Solgaard, "Air-bridged photonic crystal slabs at visible and near-infrared wavelengths," Phys. Rev. B **73**, 115126 (2006).

Chapter 6 Quantum mechanical limit to plasmonic enhancement: observation by SERS

In previous chapters, we have shown that plasmonic resonances benefit both excitation and emission of Raman scattering. The experimental measurements are explained well by classical electromagnetics. In Chapter 2, for example, I have shown that SERS EF increases with reduced gap-width. In this Chapter, we consider a regime where quantum effects become important. Only recently has it become appreciated that phenomena such as nonlocality [1–4] and electron tunneling [5–10] can emerge as feature sizes approach atomic length-scales. Here, we unambiguously demonstrate the emergence of electron tunneling at optical frequencies for metallic nanostructures with gap-widths in the single-digit angstrom range. Moreover, for the first time to the best of our knowledge, we experimentally demonstrate that the emergence of electron tunneling limits the maximum achievable plasmonic enhancement. We reach this conclusion via surface-enhanced Raman scattering (SERS) measurements. This phenomenon is likely to be of crucial importance for other applications that exploits plasmonic field enhancement. The platform developed in this work could pave the way for understanding quantum mechanical effects in more complex plasmonic nanostructures and could enable future applications of quantum plasmonics.

6.1 Fabrication of dimers with angstrom-scale gaps

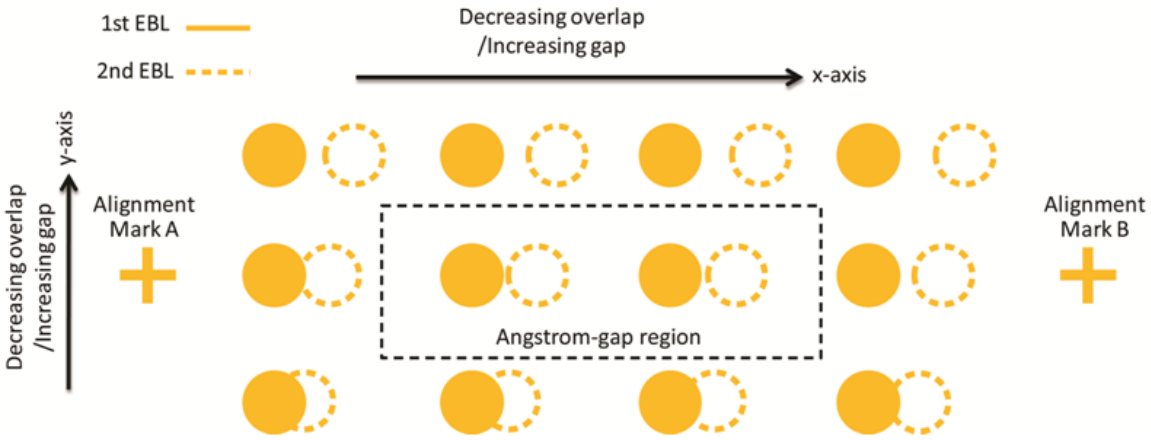

Figure 6.1 Schematic depiction of the two-step EBL process for the fabrication. Solid objects represent patterns in the first EBL. Dashed objects represent patterns in the second EBL, aligned to the first EBL. This two-step EBL process generate array of dimers with gap-width increasing from the lower-left corner to upper-right corner.

Top-down fabrication of plasmonic nanostructures traditionally makes use of electron-beam lithography (EBL), evaporation and the lift-off process. This allows flexible design and high yield [11], but the achievable feature sizes are limited by the resolution of the electron-beam resist and other factors [12]. Here, we show that this limit can be circumvented by a two-step EBL process that permits the fabrication of metallic dimers separated by angstrom-scale gaps (Figure 6.1). The nanoparticles constituting the dimers are gold disks with diameters of 90 nm and thicknesses of 20 nm, on top of a 1 nm-thick titanium adhesion layer. The first exposure starts with locating the SiN window using the scanning electron microscope (SEM) capability of the Elionix F-125. Then, an array of nanodisks, with diameters of 90 nm, is patterned such that the center of the array matches the center of the SiN window. The periodicity of the array is chosen 4 μm × 4 μm in order to minimize the coupling between adjacent nanostructures. The array has an overall

extent of 300 μm × 300 μm, i.e. slightly larger than the extent of the SiN window. This is done to ensure that the entire extent of the SiN window is filled with nanodisks. Two cross-shape alignment marks are also patterned in this exposure. After resist development, titanium (1 nm) and gold (20 nm) are evaporated, and lift-off is performed in acetone.

A second exposure is performed, aligned to the first. This consists of another array of nanodisks, again with diameters of 90 nm. The locations of the nanodisks are designed such that the two arrays, if aligned perfectly, would form an array of dimers with gap size ranging from –40 nm (i.e. overlapped) to +40 nm, gradually increasing by 0.05 nm for each successive dimer from the lower left to the upper right corners of the array. Angstrom-scale gaps are therefore achieved in the center part of the array. The overlay alignment procedure employs the positions of alignment marks A and B to minimize translational and rotational errors. For state-of-the-art EBL technology, typical translational alignment errors are below 10 nm [13]; and rotational errors are below 1 mrad. Due to these errors, it is inevitable that the dimers at the very center of the array will not have the angstrom-scale gaps that they would exhibit in the ideal case. We can nonetheless expect that such gaps will occur at other locations within the array.

6.2 TEM characterizations of fabricated dimers

To facilitate the characterization of angstrom-scale gaps inside TEM, the fabrication is performed on a silicon nitride membrane with the thickness of 30 nm. Figure 6.2(a)-(d) show top-view TEM images of four fabricated dimers, which are termed Dimers I, II, III, and IV, respectively. The gap-widths of the dimers are measured from magnified views

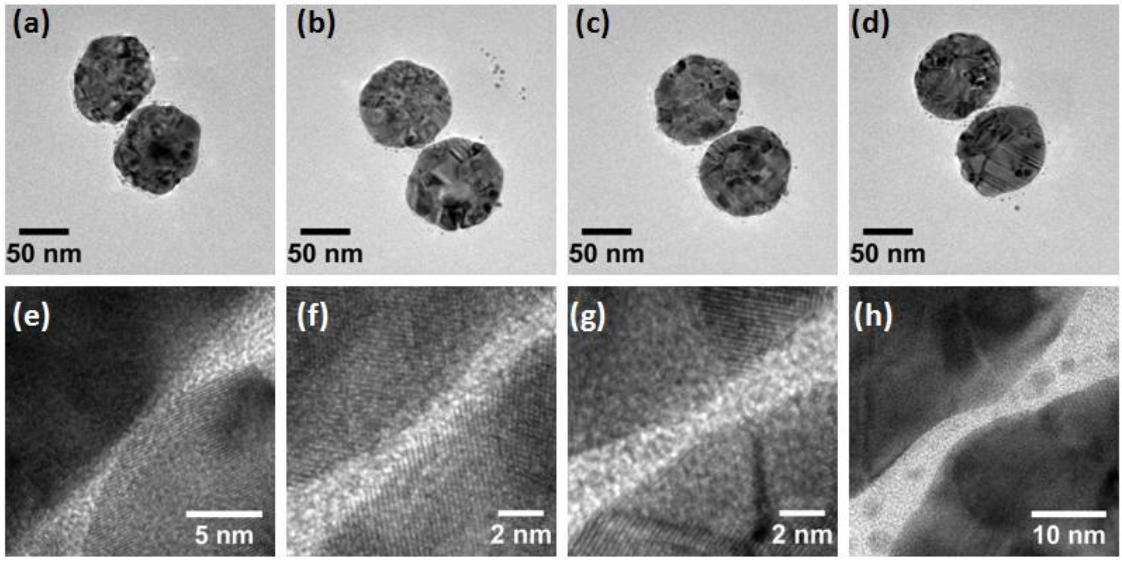

Figure 6.2 TEM images of dimers with atomic length-scale gap-width. (a-d) Top-view TEM images of four representative dimers I, II, III and IV with gradually increasing gap-width. (e-h) High-resolution magnified-view TEM images of gap regions of dimers of panels a-d. In panel e, nanoparticles touch, while panels f-h have gap-widths of 2.0 Å, 6.7 Å, and 5.8 nm, respectively.

of the gap regions shown in Figure 6.2(e)-(h). The atomic lattice of gold can be observed from these TEM images, indicating that the resolution is sufficiently high for the characterization of the angstrom-scale gaps. Small particles observed around the dimers are produced during the metal evaporation steps, and are consistently observed by TEM for similar structures [14]. We select dimers that have no such particles in the smallest region of the gap.

To prevent possible parallax errors [15] arising from sample tilting that could occur due to the high aspect ratio (gold thickness/gap-width) of the dimers, TEM images are taken at 10 additional angles in which the TEM sample holder is rotated within ±30 ° about an axis in the plane of the substrate and perpendicular to the long axis of the dimers (Figure 6.3).

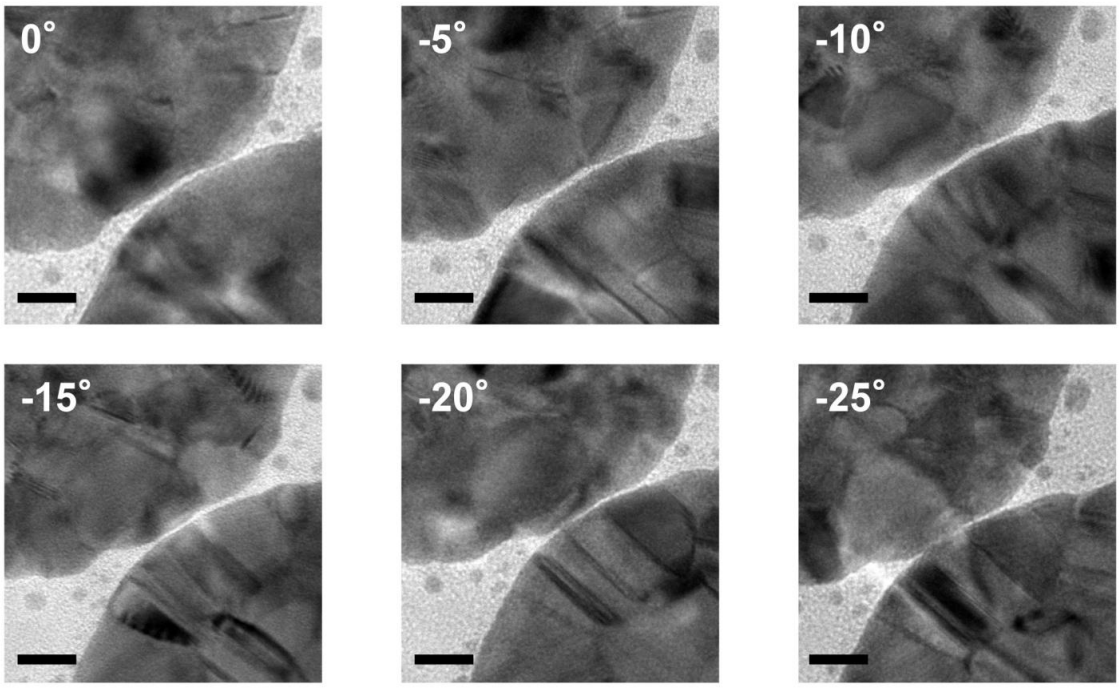

Figure 6.3 TEM images of a dimer gap observed at different angles. All scale bars are 10 nm.

We analyze each such TEM image, and define the gap-width as the distance between the two closest points on the two disks. The gap-width of the dimer is then taken as the largest gap measured from this set of TEM images. To obtain the gap size for each TEM image in a consistent manner, we perform the following procedure (Figure 6.4). First, a rectangular region of interest (ROI) is selected around the narrow portion of the gap. The line profile is averaged within the ROI to achieve good signal-to-noise ratio.

The line profile obtained from the ROI of Figure 6.4(a) is shown in Figure 6.4(b). A second ROI then is selected at a position that is away from the first ROI. The mean grayscale intensity of the pixels within the second ROI is then taken as the background value. For the ROI shown in Figure 6.4(a), the background value is found to be 301.64. The gap size is determined as the distance between the two points whose grayscale values exceed the background value (Figure 6.4(b)). Using this method, the two nanodisks of

Dimer I are found to be touching; the gap-widths for Dimer II and III are estimated to be 2.0 Å and 6.7 Å, respectively, which are comparable to the atomic lattice constant of gold [15]; and the gap-width for Dimers IV is estimated to be 5.8 nm.

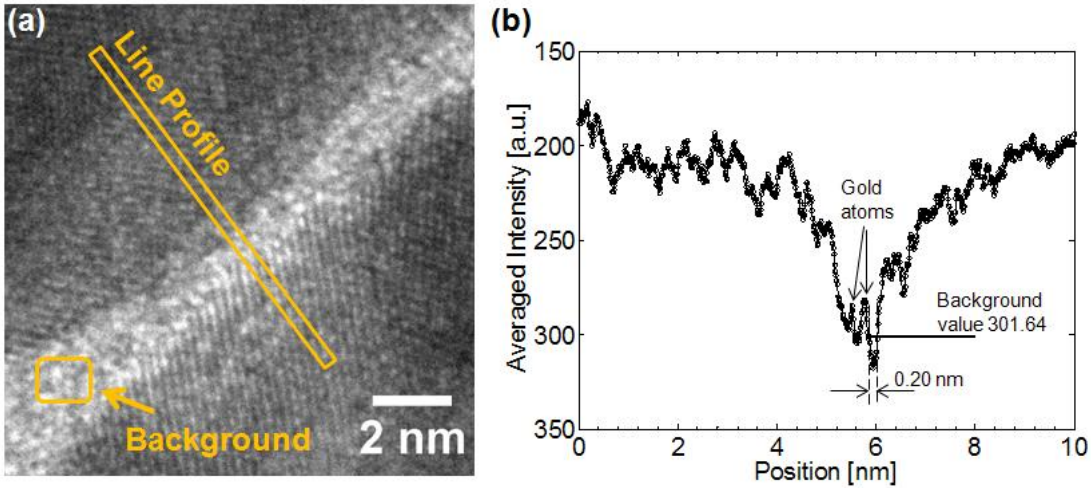

Figure 6.4 Procedure to determine gap size. (a) Selection of region for averaged line intensity profile and background characterization. (b) Averaged line intensity profile to determine gap size.

6.3 CEM and QCM simulations

In Chapter 1, we have outlined the QCM method, which presents a means for including the phenomenon of electron tunneling in classical electromagnetic simulations. Here, we compare the CEM and QCM simulations for a gold dimer that consists of two nanodisks with diameters of 90 nm and thicknesses of 20 nm. The dimer is situated on top of a thin layer of SiN whose thickness is 30 nm and whose refractive index is n = 2. CEM simulations are performed using a commercial software package (Lumerical) that

implements the 3D FDTD method. The xz-cross section of the simulation domain, for which perfectly matched layer boundary conditions are used, is shown in Figure 6.1(a). Gold is described by a Drude model, with $\varepsilon_\infty = 1$, $\omega_p = 1.94\times10^{15}$ Hz, and $\gamma = 2.14\times10^{13}$ Hz. The titanium adhesion layer is modeled by two nanodisks with diameters of 92 nm (see the discussion in Section 6.3) and thicknesses of 1 nm. These are situated beneath the gold nanodisks. The dielectric function of titanium is from a multi-coefficient fitting model provided by Lumerical FDTD. The symmetry in the plane of the substrate is exploited to minimize the simulation workload. A total-field scattered-field (TFSF) source simulates a linearly polarized plane wave normally incident on the dimer. Two power monitors that are placed outside the TFSF region measure the scattering spectrum of the dimer. A box that encloses the dimer structure has a uniform mesh of 0.5 nm. The mesh generated outside the box is non-uniform. For gaps narrower than 1 nm, a refined mesh area is generated within the gap region such that the gap width equals 4 unit cells. A 3D monitor having the same dimensions as the uniform mesh box records all field data within the box. This data is used for calculating the SERS EFs for simulations. The surface-averaged SERS EF is given by $\iint_A |E|^4\, ds \Big/ \iint_A ds$, where the surface A includes all the surfaces that are 1 nm away from both the top surfaces and side walls of the dimer.

The QCM method is implemented by quantizing the gap region of the nanodisk dimer into 8 effective layers of blocks with 8 different values of *d*, as shown in Figure 6.5(b). The same mesh configuration as that of the CEM simulations is used, but with the modification that the region containing the Drude-like material that models the tunneling is modeled with a uniform mesh with a grid cell size of 0.1 nm. The configuration of field

monitors is the same as that used in the CEM simulations. The characteristic length q=2.24 Å^{-1} in Equation (1.31) is selected for gold.

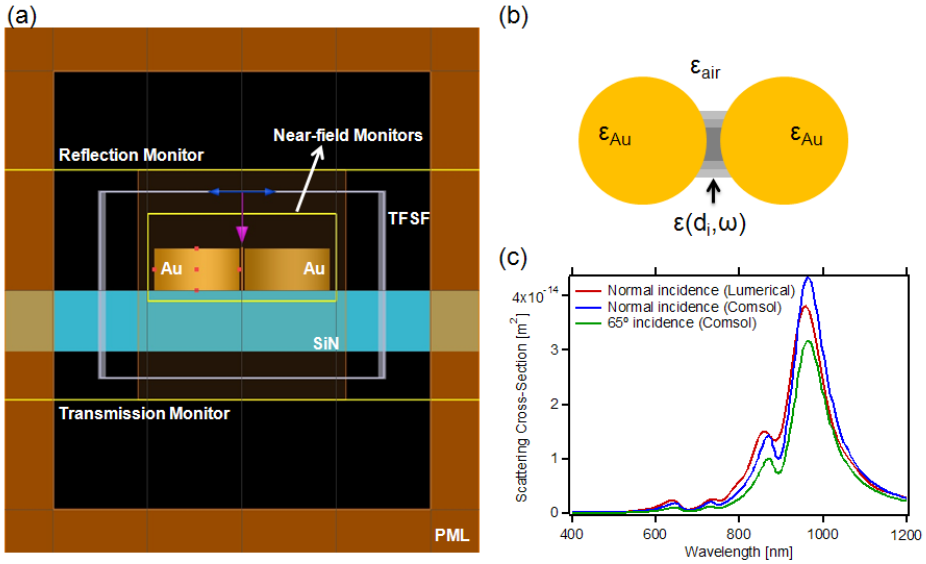

Figure 6.5 Simulation configurations of plasmonic dimer. (A) Side view of simulation domain in Lumerical. (B) Scheme of Drude-like tunneling region in QCM. (C) Comparison between normal incidence and oblique incidence.

It is also important to consider a difference that exists between the illumination conditions used in simulations and experiments. In simulations, the scattering spectra are calculated under normal incidence; while in dark-field scattering measurements, the white light source is incident at an angle of 65°. This is because implementation of oblique incidence in FDTD method would require much longer simulation times. To understand the effect that this has, we here simulate the dark-field scattering spectra in the case of oblique incidence using the finite-element method (FEM) implemented by the RF Module of the COMSOL Multiphysics package. Figure 6.1(c) shows the simulated scattering spectra obtained with normal incidence using FDTD, normal incidence using FEM, and 65° incidence using FEM. In all cases, the CEM (rather than QCM) approach

is used. It can be seen that, for normal incidence, the FEM and FDTD simulation results are in general agreement. The slight difference could be due to the differences between the dielectric functions used in these methods: FEM uses the dielectric function of gold from Ref. [16]; while Lumerical fits the data from Ref. [16] with a multiple-coefficient model. The difference in intensity between Lumerical and Comsol simulations for normal incidence could be due to the difference in collection angles. It can be seen that the spectrum under oblique incidence has similar lineshape as that with normal incidence, only differing in intensity. Therefore, we conclude that although the FDTD simulation configuration (normal incidence) is not the same as that used in dark-field scattering measurements (65 °incidence), the difference that results is relatively minor.

6.4 Impacts of electron tunneling on far-field properties of dimer

To demonstrate that the fabricated dimers exhibit quantum mechanical effects, we measure their dark-field scattering spectra. The dark-field optical setup is shown in Fig. 6.6. White light from a halogen lamp is loosely focused on the dimer array. The illumination is linearly polarized along the dimer long axis and incident at an angle of 65 ° from the normal to the substrate. An objective lens (50×, NA = 0.55) and a tube lens (f =200 mm) is placed above the TEM window and produce a dark-field image of the plasmonic dimer array at the entrance slit of the spectrometer (Acton SP2300). The entrance slit assembly is then replaced with a precision pinhole with a diameter of 200

μm to select the light scattered by the individual plasmonic dimer under study. The dark-field spectrum *S* generated by the spectrometer is then recorded from 550 nm to 1050 nm with a liquid-nitrogen cooled CCD camera (Princeton Instruments Spec-10). The integration time is 30 s. A long-pass filter (passes $\lambda > 532$ nm) placed in front of the pinhole is used to remove effect of second order diffraction by the grating in the

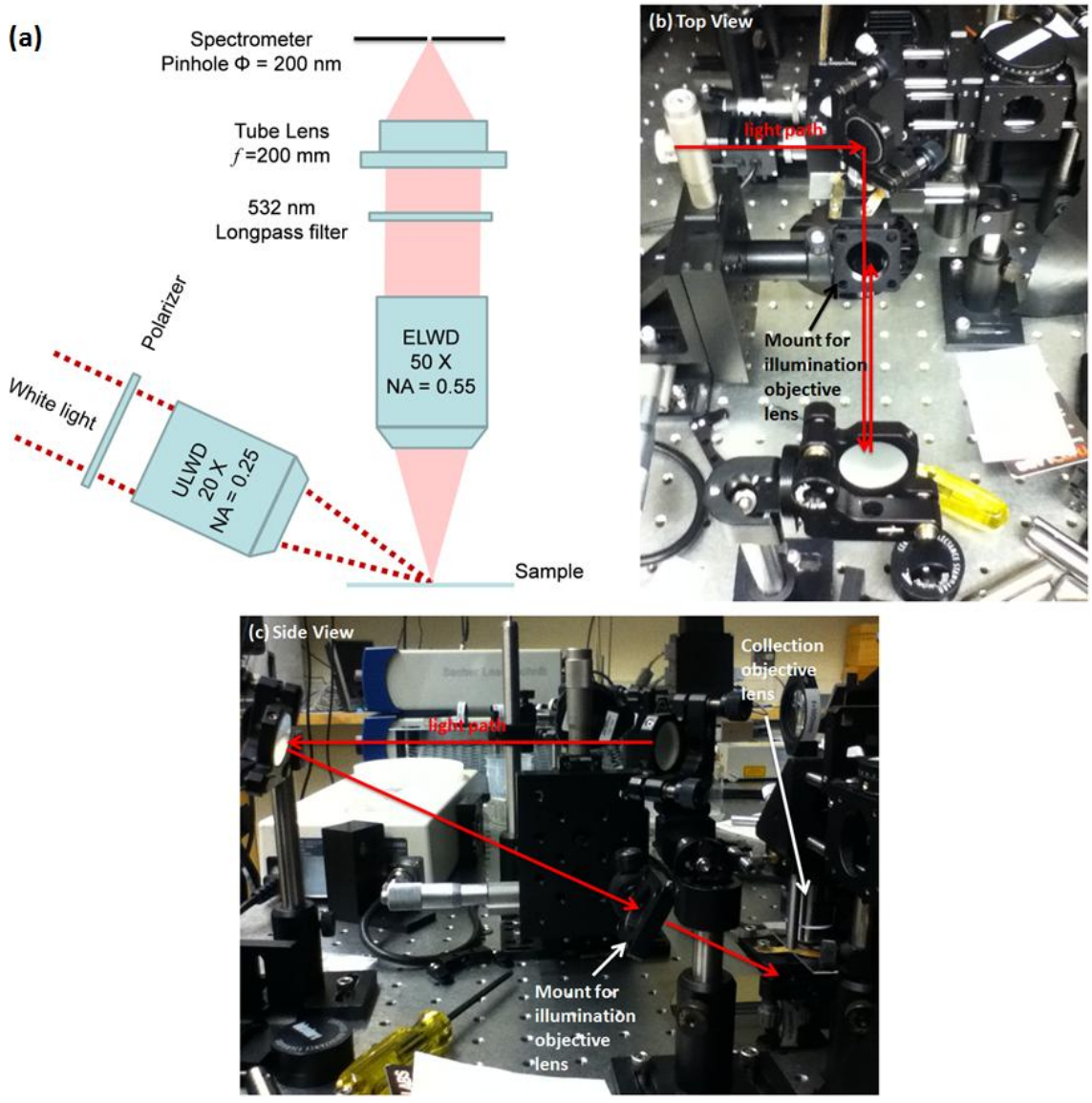

Figure 6.6 Experimental setup for dark-field scattering spectroscopy. (a) Schematic diagram. (b) Top view of optical setup. (c) Side view of optical setup.

light reflectance standard (WS-1-SL, Ocean Optics). The background spectrum *B* is measured from a region on the SiN window that does not contain any dimers. The spectrum from the dimer under study is then calculated as (*S*-*B*)/*R*.

Figure 6.7 shows scattering spectra measured from dimers with gap-widths ranging from 9.1 nm to 2.0 Å. All optical measurements reported in this paper are performed before TEM characterization to avoid the possibility of carbon contamination. They are then compared with the CEM and QCM simulation results shown in Figure 6.8(a) and (b), respectively. Classical plasmon hybridization theory [17] predicts two resonance modes for dimers, namely the bonding dipole plasmon (BDP) mode and bonding quadrupole plasmon (BQP) mode, whose charge density distributions are shown in Figure 6.9(a) and (b). For gap-widths decreasing from 9.1 nm to 6.7 Å, the measured

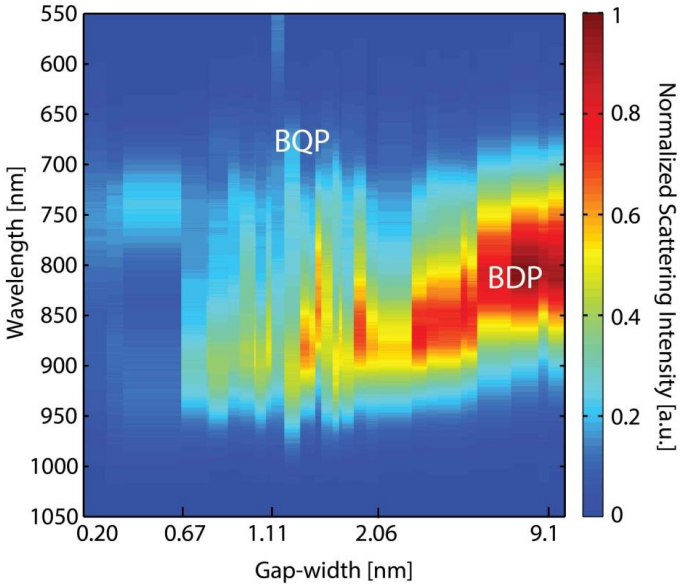

Figure 6.7 Measured dark-field scattering spectra from dimers with various gap-widths. Horizontal axis represents measured gap-widths from 2 Å to 9.1 nm in log scale. The scattering intensities are normalized by their largest value.

BDP peak resonance red-shifts from 807 nm to 892 nm, while the scattering intensity drops to 46% of its peak value. The scattering intensities of the BQP are much weaker than those of the BDP. Meanwhile, CEM simulations predict that, as the gap-width decreases from 10 nm to 7 Å, the BDP peak resonance shifts from 800 nm to 929 nm, and the scattering intensity drops to 83% of its peak value (Figure 6.8(a)). Meanwhile, scattering spectra simulated from QCM simulations reproduce those from CEM simulations, since the effective Drude model of the gap medium almost resembles vacuum for large gap-widths. The drop in the measured scattering intensity is more significant than that predicted by the CEM simulations, and is attributed to the onset of quantum mechanical effects, as we discuss below. Nonetheless, the measured peak wavelength of the BDP mode red-shifts monotonically with decreasing gap-width, as predicted by the CEM simulation, suggesting that classical plasmon hybridization is

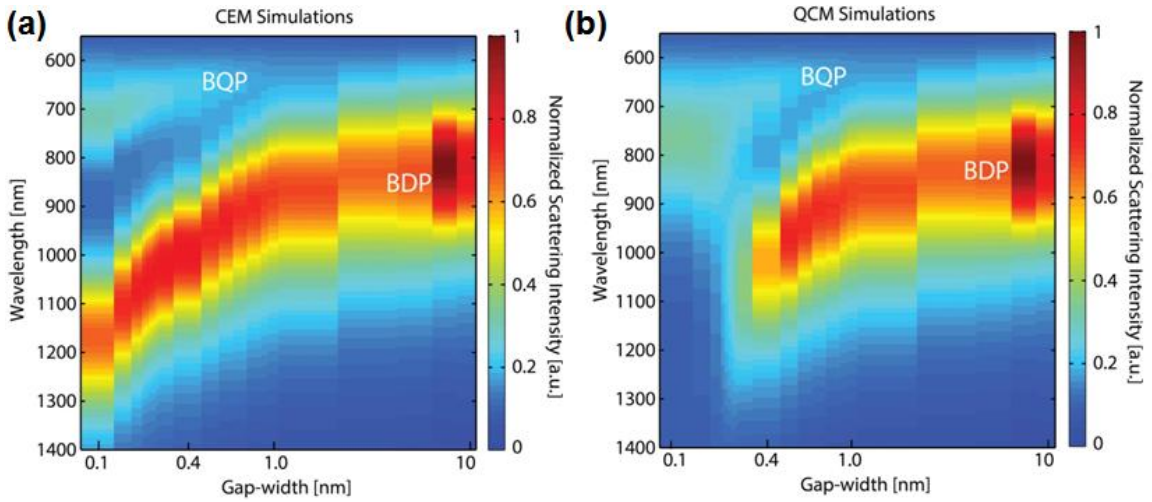

Figure 6.8 Simulated impacts of electron tunneling on dark-field scattering from dimers with angstrom-scale gaps. (a) Scattering intensities simulated by CEM for gap-widths from 1 Å to 10 nm. The scattering intensities are normalized by their largest value. (b) Scattering intensities simulated by QCM for same range of gap-widths as panel (a). Again, the scattering intensities are normalized by their largest value.

dominant for gap-widths within this range.

As the gap narrows from 6.7 Å (Dimer III) down to 2.0 Å (Dimer II), very interesting spectroscopic behaviors are observed for the BDP mode in the measured scattering spectra: the scattering resonance peak no longer redshifts, and the scattering becomes comparable to or even smaller than that of the BQP around 750 nm. These two features in Figure 6.7 differ substantially from the prediction of CEM simulations in Figure 6.8(a). On the other hand, for gap-widths smaller than 4 Å, QCM simulations in Figure 6.8(b) show that the BDP resonance peak no longer red-shifts, and its intensity drops significantly. The BQP then becomes the dominant resonance in the spectra. Examination of Fig. 2A confirms that these features are indeed observed in the experiments for dimers with gap-widths less than 6.7 Å. For gap-widths in this regime, the electron tunneling effect is significant in that it effectively create a "charge transfer" channel across the gap. The charges with opposite signs on the two sides of the gap thus neutralize each other through this channel, generating new mode as shown in Figure 6.3(c).

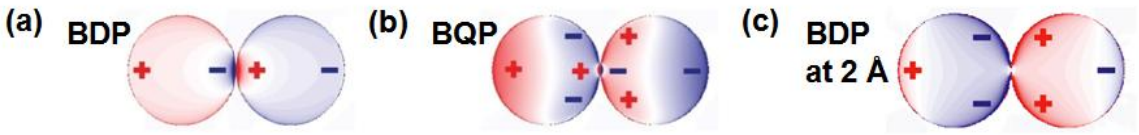

Figure 6.9 Simulated charge density distributions for three plasmonic modes. (a) Bonding dipole plasmon (BDP) simulated with CEM. (b) Bonding quadrupole plasmon (BQP) simulated with CEM. These are calculated from dimer with gap-width of 9 Å. (c) BDP simulated with QCM for dimer with gap-width of 2 Å.

We also exclude the possibility that the titanium adhesion layer might be the origin of the "charge transfer" channel. Due to the gold having a small thickness (20 nm) and poor adhesion between it and the SiN membrane, the use of a titanium adhesion layer is crucial. Figure 6.10(a) and (b) show two dimers fabricated without and with an adhesion layer. Both dimers are designed to consist of two nanodisks with diameters of 90 nm and thicknesses of 20 nm. It is clear that the shape of the dimer without adhesion layer is very irregular by comparison to the dimer with the 1 nm titanium adhesion layer. Figure 6.10(c) shows a magnified view of the gap region. It can be seen that the adhesion layer appears to be 2 nm wider than the gold structure. Thus for dimer with gap size less than ~4 nm, our observation implies that the two adhesion layers for the nanodisk dimer are connected. To study the effect of adhesion layer, we perform a test simulation on a dimer with gap size of 1 nm and with titanium adhesion layer. Figure 6.10(d) shows the calculated charge density distribution of the fundamental mode. It represents a well-defined BDP mode (compared to Figure 6.9(a)) rather than a charge transfer plasmon (CTP) mode (Figure 6.9(c)). The latter occurs for dimers that are electrically connected, i.e. they do not have a gap [6]. Therefore, we believe that although the dielectric function of titanium suggests metallic properties, the conductivity is still not large enough to introduce a charge transfer channel.

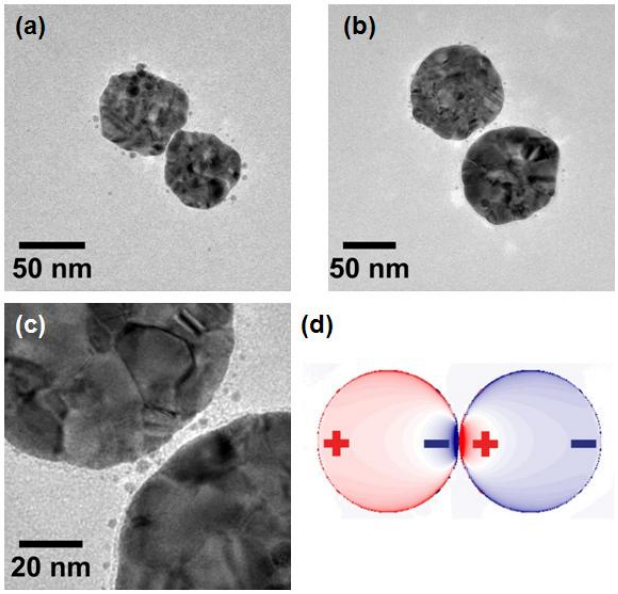

Figure 6.10 Effect of adhesion layer. (A) Fabrication without adhesion layer. (B) Fabrication with 1 nm titanium as adhesion layer. (C) Adhesion layer in gap region. (D) Charge density distribution of BDP mode of a dimer with gap of 1 nm between gold disks, but with adhesion layer that connects disks.

6.5 Impacts of electron tunneling on near-field properties of dimer

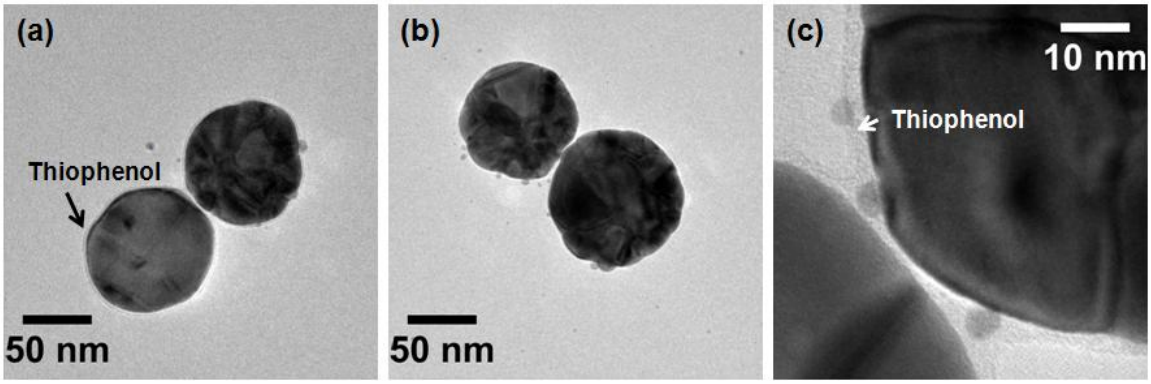

Figure 6.11 TEM characterization of SAM of thiophenol. (a) Gold dimer with thiophenol SAM. (b) Gold dimer without thiophenol SAM. (c) Thiophenol SAM within gap region.

To investigate the impact of electron tunneling on the near-field enhancement of dimers with atomic length-scale gaps, we perform SERS measurements. These are expected to be revealing due to the fact that SERS enhancement factor (EF) scales roughly as the fourth power of the near-field enhancement. Before SERS measurements, self-assembled monolayers (SAM) of thiophenol are formed on the plasmonic dimers. We compare the TEM images of gold dimers with and without the thiophenol SAM, shown in Figure 6.11(a) and (b), respectively. These dimers have thicknesses of 40 nm, and have no adhesion layer. Thus the light gray region that appears 1 nm wider than the gold dimer (Figure 6.11(a)) represents the thiophenol SAM. The gap size of the dimer shown in Figure 6.11(c) is determined to be ~5.7 Å. It can be seen from Figure 6.11(c) that, despite this gap being very small, the thiophenol molecules fill the entire gap region. Therefore, in our estimation of SERS EF, we assume monolayer coverage of thiophenol on all the exposed surfaces of the gold dimers.

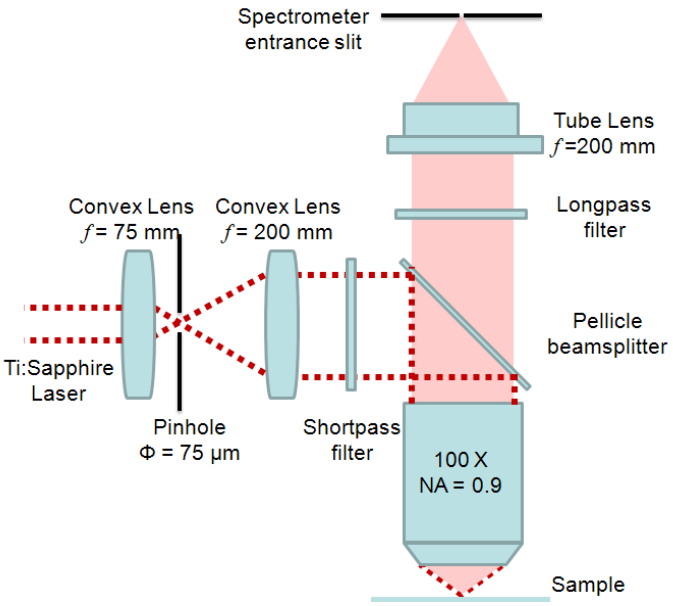

Figure 6.12 Experimental setup for wavelength-scanning Raman spectroscopy.

To ensure that the maximum SERS enhancement is measured for each dimer (i.e. for each gap size), we measure SERS spectra at 19 different laser wavelengths (every 10 nm from 705 nm to 885 nm) for each dimer. This is performed using a homebuilt wavelength-scanning confocal Raman microscope (epi-configuration), as shown in Figure 6.12. A Ti:Sapphire laser (Mira 900, Coherent) that is tunable from 700 nm to 900 nm and working in continuous-wave (CW) mode is used as the Raman excitation source. The laser power is kept below 20 μW to avoid damage to the sample, thereby permitting multiple SERS measurements. It also avoids the nonlinear field enhancement that has been predicted to occur at higher intensities [18,19]. The laser polarization is along the dimer axis, *i.e.* the same as that employed in the dark-field scattering measurements. For each wavelength, the beam from the Ti:Sapphire laser is spatially filtered with a precision pinhole with diameter of 75 μm. The light transmitted by the pinhole is collimated by a lens to a diameter of ~ 3 mm, meaning that, after being transmitted by a short-pass filter and being reflected by a beam-splitter, it overfills the back-aperture of the objective lens (100×, NA = 0.9). The purpose of the short-pass filter is to remove light that might be otherwise collected into the spectrometer by Rayleigh scattering. A pellicle beamsplitter (8:92 splitting ratio, CM1-BP108, Thorlabs) then directs ~8% of the laser beam onto the objective, which creates a near diffraction-limited laser spot on the SiN window. The long axis of the dimer under study is placed along the polarization of the laser. A piezo-stage then moves the dimer into the center of the beam to maximize the intensity of Stokes scattering. This Stokes scattering is then collected by the same objective lens; and transmitted by the pellicle beamsplitter with an efficiency of ~92%. It then passes through a long-pass filter to remove the laser line, and is focused on the spectrometer

entrance slit. The Raman spectra are then measured by the spectrometer, which is equipped with the liquid-nitrogen cooled CCD. Integration times of 60 s are used.

The measurement results for two dimers (Dimer II and III in Figure 6.2) are shown in Figure 6.13. From the far-field optical measurements and high-resolution TEM images, we conclude that electron tunneling is expected for Dimer II, but not for Dimer III. We record the dark-field scattering spectra of the dimers with and without thiophenol SAMs. It can be seen that, for both dimers, SAM formation results in increased scattering intensities (Figure 6.13(a) and (b)). The resonance lineshapes are maintained, however. Of particular note is that the suppression of the BDP of Dimer II, compared to that of Dimer III, is maintained with the formation of the thiophenol SAM. This suggests that electron tunneling through the SAM is still significant for such narrow gaps.

The wavelength-scanning Raman measurement results are shown in Figure 6.13(c) and (d). Each column of measurements shows the Raman intensity normalized by the laser power. To quantify the SERS performance, we measure the SERS EFs of the 1074 cm^{-1} line for each laser wavelength for the two dimers. The results are plotted along with the dark-field scattering spectra in Figure 6.13(a) and (b). Contrary to previous reports [20], the results show that the wavelength-dependent SERS EF follows the lineshape of the dark-field scattering spectra in the single dimer limit. We note that one difference between the results shown here and those of Ref. [20] is that in our case, SERS and dark-field scattering measurements are both made with light polarized along the axis of each dimer. The maximum SERS EF for Dimer II with 2.0 Å gap is 2.4×10^{8}, achieved at a laser wavelength of 815 nm. The maximum SERS EF for Dimer III with 6.7 Å gap is 1.2×10^{9}, achieved at a laser wavelength of 820 nm. These results suggest that as

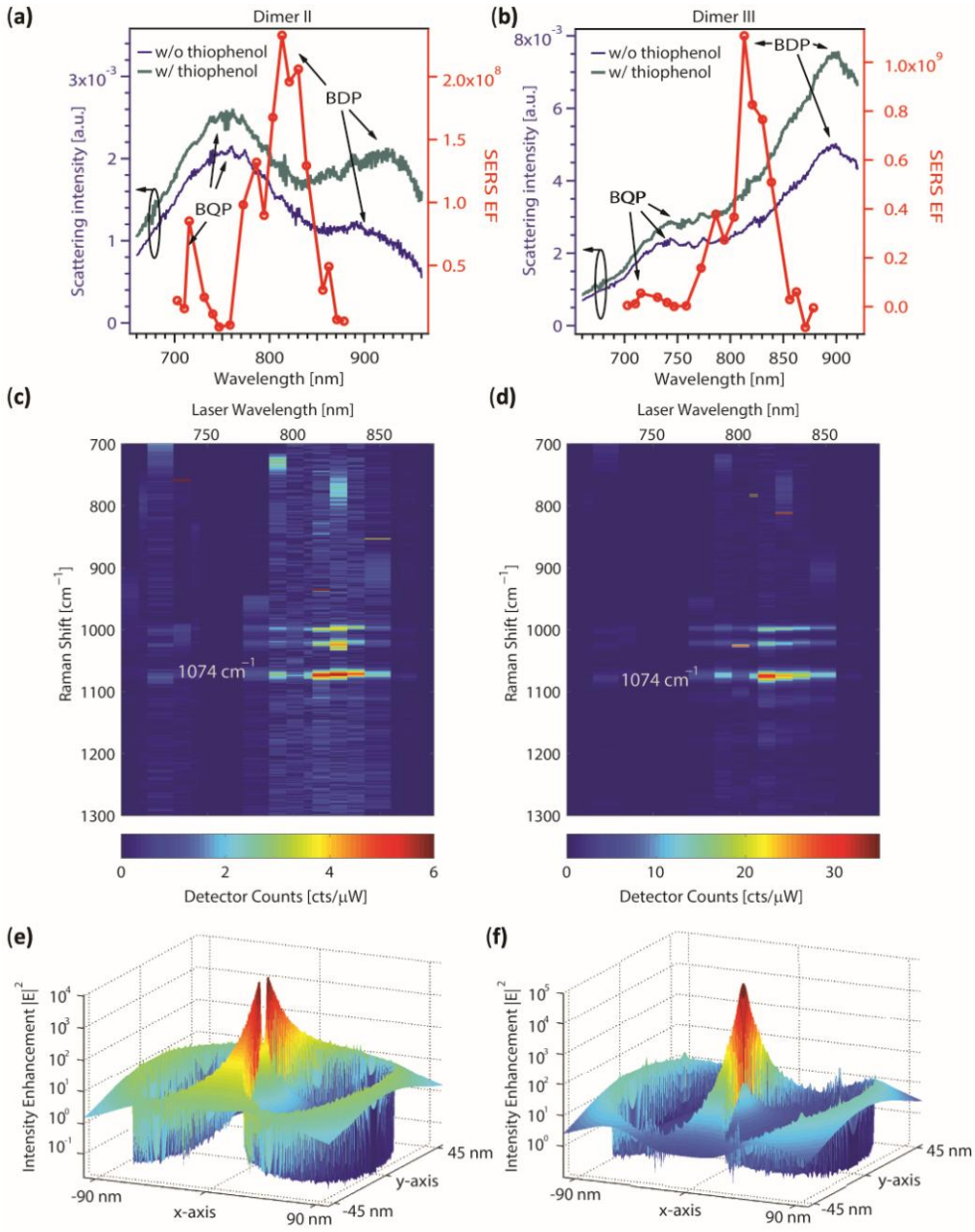

Figure 6.13 Dark-field scattering and wavelength-scanning SERS measurements on Dimers II and III, whose gap-widths are 2.0Å and 6.7 Å, respectively. (a-b) Dark-field scattering spectra measured before and after formation of thiophenol SAM, along with measured wavelength-dependent SERS EF, for Dimers II and III, respectively. (c-d) Intensity maps of Raman scattering from Dimers II and III, respectively. 1074 cm^{-1} thiophenol Raman line is used to calculate SERS EFs. (e) Near-field intensity distribution simulated by QCM for ideal nanodisk dimer structure with gap-width of 2.0 Å, at its peak resonance wavelength. (f) Near-field intensity distribution simulated by QCM for ideal nanodisk dimer structure with gap-width of 7 Å.

gap-widths reduce to the single-digit angstrom range, the SERS EF, hence the field enhancement, does not increase as predicted by CEM, but instead decreases.

To further explain this observation, we simulate the electric field intensity distributions for dimers with gap-widths of 2 Å and 7 Å using the QCM (Figure 6.13(e) and (f), respectively). Each intensity distribution is plotted at the wavelength for which the BDP has largest surface-averaged enhancement. For a dimer with a larger gap-width of 7 Å, Figure 6.13(f) shows that only one hotspot occurs in the narrowest region of the gap, consistent with the near-field distribution of plasmonic dimers in classical model [21], with a maximum intensity enhancement of 7.0×10^4. On the other hand, Figure 6.13(e) shows that QCM simulations predict a significant reduction in the near-field when the gap-width is 2 Å, with smaller maximum intensity enhancement of 1.1×10^4. The intensity distribution shows two hotspots, and the field at the center of the gap is significantly suppressed. For dimers with such small gap-width, the electron tunneling becomes appreciable to provide an effective "charge-transfer" channel, thus reduces the build-up of charges of opposite sign on the two sides of the gap. The emergence of electron tunneling therefore sets the ultimate upper limit on achievable field enhancement, hence the SERS EF.

Further evidences are shown in Figure 6.14(a) as we analyze the results of the wavelength-scanning SERS measurements performed on 45 different dimers whose gap-widths range from 9.1 nm to 2.0 Å. We plot in log-log scale the largest EF measured for each dimer with its gap-width measured by high-resolution TEM. For comparison, we use both CEM and QCM simulations to estimate the electromagnetic SERS EFs as shown in Figure 6.14(b). Amongst all 45 dimers, the maximum SERS EF measured is 1.2×10^9.

This is achieved by Dimer III, whose gap is 6.7 Å. There are clearly two regions in Figure 6.14(a) that show opposite trends for SERS EF as a function of gap-width. For gap-width ranging from 10 nm to 6.7 Å, it is observed that the SERS EF generally increases as the gap-width decreases, as expected by both CEM and QCM simulations shown in Figure 6.14(b). As gap-width decreases from 6.7 Å to 2.0 Å, the measured SERS EF no longer increases, but instead decreases significantly. For gap-widths in the

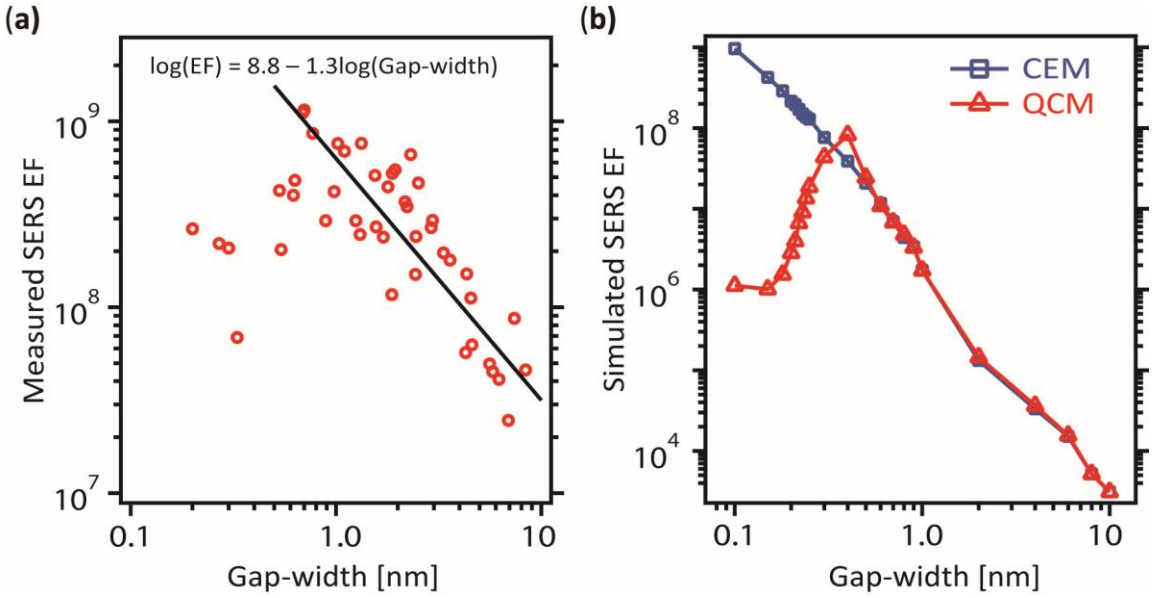

Figure 6.14 Impact of quantum mechanical electron tunneling on SERS EF. (a) Maximum SERS EFs for 45 dimers measured by wavelength-scanning SERS, shown as red circles. Two regions that show opposite trends for SERS EF as function of gap-width are observed. For gap-width ranging from 6.7 Å to 9.1 nm, the measured SERS EF generally follows the phenomenological linear fit (in a log-log scale) as: log(EF) = 8.8 – 1.3log(Gap-width). The SERS EF generally increases as the gap-width decreases in this region. As gap-width further decreases from 6.7 Å to 2.0 Å, the SERS EF does not increase, but instead decreases significantly. (b) Simulated SERS EFs using both QCM and CEM for gap-widths ranging from 1 Å to 10 nm.. The CEM simulations predict monotonic increase of the SERS EF as the gap-width decreases. The QCM simulations show a turning point around 4 Å due to the emergence of electron tunneling for smaller gap-width.

same range, the CEM simulations predict a monotonic increase of SERS EF as the gap narrows, which contradicts our observations. QCM simulations, on the other hand, take into account electron tunneling and predict a turning point around 4 Å in the SERS EF *vs.* gap characteristics, in a similar manner to what is observed experimentally. Moreover, this gap-width region matches the exact region in which we observe the impact of electron tunneling on the dark-field scattering spectra of the same group of dimers. The emergence of electron tunneling not only reduces the scattering intensity of the BDP mode, but also reduces the SERS EF. Through the correlation between the structures and the optical properties of dimers with angstrom-scale gaps, we thus demonstrate that the maximum achievable SERS EF, hence plasmonic field enhancement, is limited by the quantum mechanical electron tunneling.

6.6 Simulated impacts of nonlocal effect on scattering spectra and field enhancements

In Chapter 1, we outlined a "locality analogue method (LAM)" that allows nonlocal effects to be modeled using classical electromagnetics simulations. Figure 6.15(a) and (b) compare the simulated scattering spectra predicted by the LAM (i.e., considering nonlocality) and the CEM (i.e., without considering nonlocality). Both simulation results are in good agreement for gap size of 4 nm, indicating nonlocality is not significant for large gap sizes. As the gap narrows, the deviation in the peak wavelength of the

resonance becomes larger. For simulated dimer with 2 Å gap, LAM predicts a resonance that is blue-shifted by 250 nm compared with CEM predictions.

It is also noted that the LAM does not take into account electron tunneling. Thus the simulated scattering spectrum for a dimer with a gap of 2 Å is quite different from our measured spectra. On one hand, this observation indicates that electron tunneling is the dominant quantum mechanical effect for gap size in this regime. On the other hand, the large difference in the resonance position between measured data and QCM simulations (mentioned in the main text) could be due to nonlocal effect. For example, the longest resonance wavelength predicted by the QCM simulations is ~1050 nm, while the experimentally measured value is ~920 nm. A model that combines both QCM and LAM would thus be preferable to fully explain the details in our measured data; but is out of the scope of our present work.

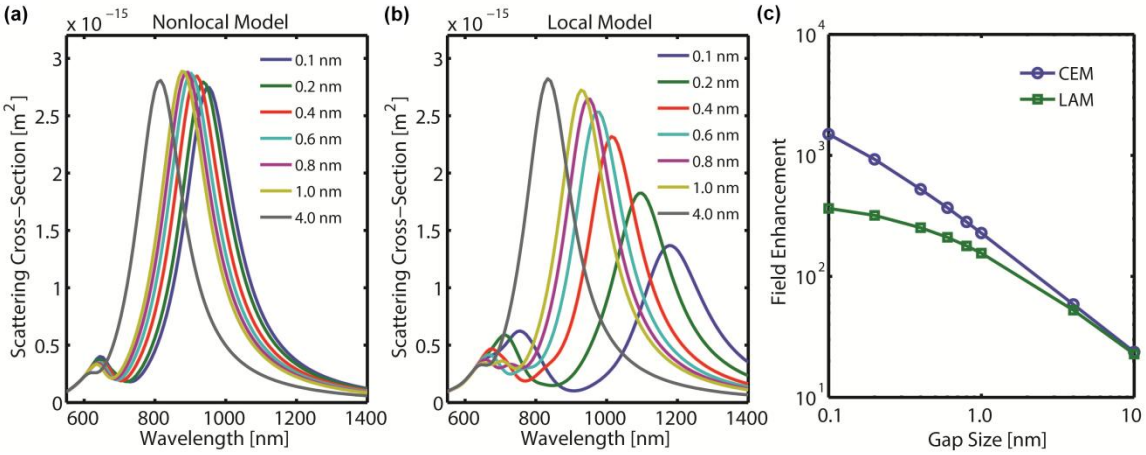

Figure 6.15 Impact of nonlocality. (a) Simulated scattering cross-section of gold dimer with various gap widths using LAM. (b) Simulated scattering cross-section of gold dimer with various gap widths using CEM. (c) Field enhancement at the midpoints of the gaps simulated with LAM and CEM.

We also examine the impact of nonlocality on field enhancements. Figure 6.15(c) summarizes the simulated field enhancements for various gap widths using the LAM and the CEM. These field enhancements are recorded at the midpoints of the gaps at their peak resonance wavelengths. It can be seen that the LAM predicts field enhancements that are smaller than those of the CEM. It can also be seen however that the LAM predicts that enhancement increases as gap width narrows, in contradiction to our experimental measurements shown in Figure 6.14(a). We therefore conclude that it is predominantly electron tunneling across the gap, rather than nonlocality, that sets the limit to field enhancement.

6.7 Conclusions

In conclusion, we develop a top-down nanofabrication method that achieves lithographically fabricated plasmonic dimers with gap-widths as narrow as 2.0 Å. Through correlation between the structural characterization of each individual dimer using high-resolution TEM, and its optical properties using dark-field scattering spectroscopy and wavelength-scanned SERS, we demonstrate that the maximum achievable plasmonic enhancement is limited by quantum mechanical electron tunneling. This phenomenon is also likely to be of crucial importance for other plasmonic applications, such as optical manipulation [22], four-wave mixing [23], high-harmonic generation [21], and optical rectification [24]. We believe the experimental platform demonstrated here offers unique advantages for these studies. This platform could also pave the way for understanding quantum plasmonics in metallic nanostructures that are

more elaborate than dimers, such as heptamers and higher-order oligomers. We also note that, although electron tunneling should be avoided to achieve large plasmonic enhancement, by actively controlling the effect, *e.g.* by the Fowler-Nordheim effect [18], future applications of quantum plasmonics could be enabled.

References

[1] J. M. McMahon, S. K. Gray, and G. C. Schatz, "Optical properties of nanowire dimers with a spatially nonlocal dielectric function," Nano Lett. **10**, 3473–3481 (2010).

[2] C. Cirac ì, R. T. Hill, J. J. Mock, Y. Urzhumov, A. I. Fern ández-Dom ínguez, S. A. Maier, J. B. Pendry, A. Chilkoti, and D. R. Smith, "Probing the ultimate limits of plasmonic enhancement," Science **337**, 1072–1074 (2012).

[3] G. Toscano, S. Raza, A.-P. Jauho, N. A. Mortensen, and M. Wubs, "Modified field enhancement and extinction by plasmonic nanowire dimers due to nonlocal response," Opt. Express **20**, 4176–4188 (2012).

[4] Y. Luo, A. I. Fernandez-Dominguez, A. Wiener, S. A. Maier, and J. B. Pendry, "Surface Plasmons and Nonlocality: A Simple Model," Phys. Rev. Lett. **111**, 093901 (2013).

[5] J. Zuloaga, E. Prodan, and P. Nordlander, "Quantum description of the plasmon resonances of a nanoparticle dimer," Nano Lett. **9**, 887–891 (2009).

[6] R. Esteban, A. G. Borisov, P. Nordlander, and J. Aizpurua, "Bridging quantum and classical plasmonics with a quantum-corrected model," Nat. Commun. **3**, 825 (2012).

[7] K. J. Savage, M. M. Hawkeye, R. Esteban, A. G. Borisov, J. Aizpurua, and J. J. Baumberg, "Revealing the quantum regime in tunnelling plasmonics," Nature **491**, 574–577 (2012).

[8] J. A. Scholl, A. Garc á-Etxarri, A. L. Koh, and J. A. Dionne, "Observation of quantum tunneling between two plasmonic nanoparticles," Nano Lett. **13**, 564–569 (2013).

[9] S. Kadkhodazadeh, J. B. Wagner, H. Kneipp, and K. Kneipp, "Coexistence of classical and quantum plasmonics in large plasmonic structures with subnanometer gaps," Appl. Phys. Lett. **103**, 083103 (2013).

[10] M. S. Tame, K. R. McEnery, Ş. K. Özdemir, J. Lee, S. A. Maier, and M. S. Kim, "Quantum plasmonics," Nat. Phys. **9**, 329–340 (2013).

[11] N. Félidj, J. Aubard, G. Lévi, J. R. Krenn, a. Hohenau, G. Schider, a. Leitner, and F. R. Aussenegg, "Optimized surface-enhanced Raman scattering on gold nanoparticle arrays," Appl. Phys. Lett. **82**, 3095 (2003).

[12] V. R. Manfrinato, L. Zhang, D. Su, H. Duan, R. G. Hobbs, E. a Stach, and K. K. Berggren, "Resolution limits of electron-beam lithography toward the atomic scale," Nano Lett. **13**, 1555–1558 (2013).

[13] N. Liu, H. Guo, L. Fu, S. Kaiser, H. Schweizer, and H. Giessen, "Three-dimensional photonic metamaterials at optical frequencies.," Nat. Mater. **7**, 31–37 (2008).

[14] M. D. Fischbein and M. Drndić, "Nanogaps by direct lithography for high-resolution imaging and electronic characterization of nanostructures," Appl. Phys. Lett. **88**, 063116 (2006).

[15] J. Kern, S. Gro ßmann, N. V Tarakina, T. Ha, M. Emmerling, M. Kamp, J. Huang, P. Biagioni, J. C. Prangsma, B. Hecht, B. Group, E. Physik, and T. Physik, "Atomic-Scale Confinement of Resonant Optical Fields," Nano Lett. **12**, 5504–5509 (2012).

[16] P. B. Johnson and R. W. Christy, "Optical constants of the noble metals.," Phys. Rev. B **6**, 4370–4379 (1972).

[17] P. Nordlander, C. Oubre, E. Prodan, K. Li, and M. I. Stockman, "Plasmon hybridization in nanoparticle dimers," Nano Lett. **4**, 899–903 (2004).

[18] L. Wu, H. Duan, P. Bai, M. Bosman, J. K. W. Yang, and E. Li, "Fowler-Nordheim tunneling induced charge transfer plasmons between nearly touching nanoparticles," ACS Nano **7**, 707–716 (2013).

[19] D. C. Marinica, A. K. Kazansky, P. Nordlander, J. Aizpurua, and A. G. Borisov, "Quantum plasmonics: nonlinear effects in the field enhancement of a plasmonic nanoparticle dimer," Nano Lett. **12**, 1333–1339 (2012).

[20] S. L. Kleinman, B. Sharma, M. G. Blaber, A.-I. Henry, N. Valley, R. G. Freeman, M. J. Natan, G. C. Schatz, and R. P. Van Duyne, "Structure enhancement factor relationships in single gold nanoantennas by surface-enhanced Raman excitation spectroscopy," J. Am. Chem. Soc. **135**, 301–308 (2013).

[21] P. Mühlschlegel, H.-J. Eisler, O. J. F. Martin, B. Hecht, and D. W. Pohl, "Resonant optical antennas," Science **308**, 1607–1609 (2005).

[22] M. Righini, P. Ghenuche, S. Cherukulappurath, V. Myroshnychenko, F. J. García de Abajo, and R. Quidant, "Nano-optical trapping of Rayleigh particles and Escherichia coli bacteria with resonant optical antennas," Nano Lett. **9**, 3387–3391 (2009).

[23] S. Palomba, S. Zhang, Y. Park, G. Bartal, X. Yin, and X. Zhang, "Optical negative refraction by four-wave mixing in thin metallic nanostructures," Nat. Mater. **11**, 34–38 (2012).

[24] D. R. Ward, F. Hüser, F. Pauly, J. C. Cuevas, and D. Natelson, "Optical rectification and field enhancement in a plasmonic nanogap," Nat. Nanotechnol. **5**, 732–736 (2010).